Enhanced Thermoelectric Performance at the Superionic Phase Transitions of Mixed Ion-Electron Conducting Materials
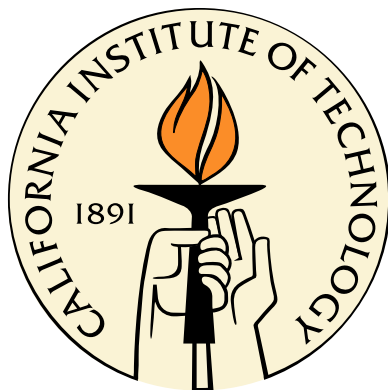
Thesis by

David R. Brown

In Partial Fulfillment of the Requirements

for the Degree of

Doctor of Philosophy

California Institute of Technology

Pasadena, California

2015

(Defended July 17th, 2014)

Acknowledgements

To all who have taken the time to read some or all of this document, please accept my gratitude.

I would first like to thank my adviser, Jeff Snyder. His door was always open, and he was always happy to discuss science with me. I've learned immensely both about the details of thermoelectrics science and about how to conduct myself as a professional scientist from my conversations with him. I will always be grateful to him for opening the door to his lab to me in 2011.

I've worked with many great scientists at Caltech, and I learned a lot from my peers. Tristan Day synthesized most of the samples studied in this thesis. I have benefitted from Nick Heinz's expertise on microstructure; Zachary Gibb's on band structure calculations and python coding; Wolfgang Zeier's on solid state chemistry; and Heng Wang and Yanzhong Pei's expertise on band structure engineering and modeling. Shiho Iwanaga and Aaron Lalonde taught me the basics of thermoelectric instrumentation in the short time I overlapped with them at Caltech. My officemate Fivos Drymiotis is an experienced scientist whose advice I am always keen to hear.

I've had the opportunity to mentor and advise to a greater and lesser degree a number of graduate and undergraduate students. First and foremost I'd like to thank David Neff, who was my undergraduate assistant for one year and an expert at putting any random thing I could imagine together with his hands. Stephen Kang found my work interesting enough that he is pursuing it further for his own Ph.D.

I'd like to thank my colleagues at the JPL thermoelectrics group. In particular I'd like to thank Alex Zevalkink, Pawan Gogna, and Samad Firdosy for assisting with measurements. I'd like to thanks Sabah Bux for helping to organize my collaborations

iv

Abstract

The quality of a thermoelectric material is judged by the size of its temperature dependent thermoeletric-figure-of-merit (zT). Superionic materials, particularly Zn_4Sb_3 and Cu_2Se, are of current interest for the high zT and low thermal conductivity of their disordered, superionic phase. In this work it is reported that the super-ionic materials Ag_2Se, Cu_2Se and $Cu_{1.97}Ag_{0.03}Se$ show enhanced zT in their ordered, normal ion-conducting phases. The zT of Ag_2Se is increased by 30% in its ordered phase as compared to its disordered phase, as measured just below and above its first order phase transition. The zT's of Cu_2Se and $Cu_{1.97}Ag_{0.03}Se$ both increase by more than 100% over a 30 K temperatures range just below their super-ionic phase transitions. The peak zT of Cu_2Se is 0.7 at 406 K and of $Cu_{1.97}Ag_{0.03}Se$ is 1.0 at 400 K. In all three materials these enhancements are due to anomalous increases in their Seebeck coefficients, beyond that predicted by carrier concentration measurements and band structure modeling. As the Seebeck coefficient is the entropy transported per carrier, this suggests that there is an additional quantity of entropy co-transported with charge carriers. Such co-transport has been previously observed via co-transport of vibrational entropy in bipolaron conductors and spin-state entropy in $Na_xCo_2O_4$. The correlation of the temperature profile of the increases in each material with the nature of their phase transitions indicates that the entropy is associated with the thermodynamcis of ion-ordering. This suggests a new mechanism by which high thermoelectric performance may be understood and engineered.

Contents

List of Figures

List of Tables

Chapter 1

Introduction

1.1 Summary of Introduction

In this chapter I will introduce the motivation and basic concepts that underpin this thesis. In section 1.2 I will discuss the motivations for thermoelectric materials development. In section 1.3 I will describe what the figure-of-merit zT is and explain why it is a good number for describing the performance of thermoelectric devices. In section 1.4 I will discuss the concept of Seebeck and zT enhancement via co-transport of non-electronic entropy. In section 1.5 I will discuss superionic materials and why there is so much recent interest in them as good thermoelectric materials; this section will include a brief discussion of prior work on Ag_2Se [26], Cu_2Se [23] and $Cu_{1.97}Ag_{0.03}Se$ [23]. In section 1.6 I will briefly summarize the key challenges and results of this work.

1.2 Motivation of Thermoelectric Research

A critical problem of the twenty-first century is of energy and sustainability. The limited supply of fossil fuels and the growing global population and economy have caused a steadily increasing price of electricity [37]. The massive quantities of CO_2 emitted in fossil fuel based energy production is causing worldwide climate change [152]. In order to address these challenges renewable energy sources should be developed and energy demand reduced. Though there is a pilot program to demonstrate cost ef-
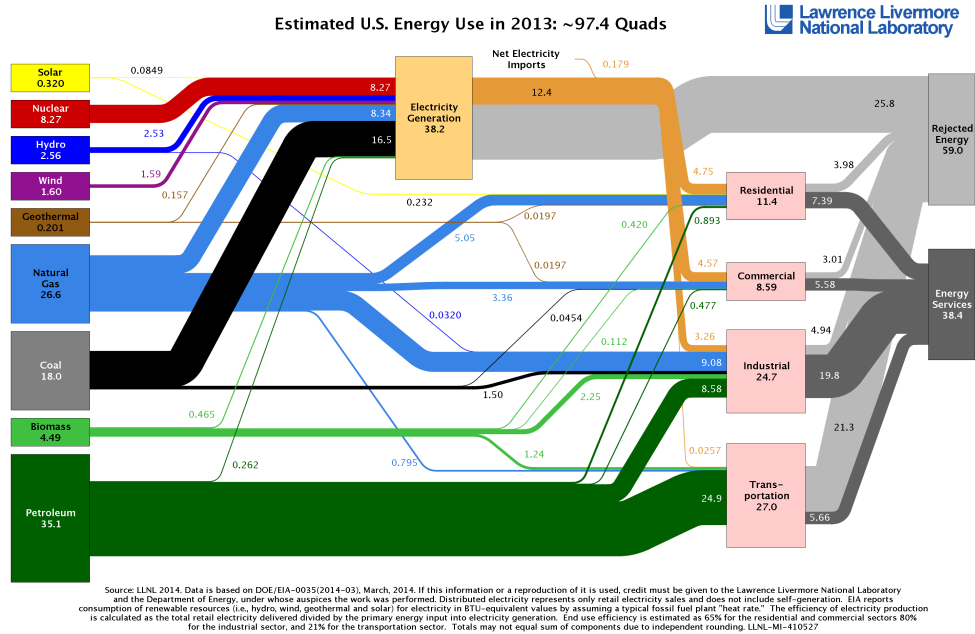
Figure 1.1: Sankey diagram of 2013 US energy inputs and outputs. 26 Quadrillion BTU's are lost as waste head in the industrial and transportation. Over 1 Quadrillion BTU's would be recoverable with $ZT = 2$ thermolectric materials. Image credit: Lawrence Livernmore National Laboratories.

fective thermoelectric power generation [146], thermoelectric devices are principally focused on reducing demand without decreasing economic activity [13]. This is accomplished by two different strategies. The first is to develop a thermoelectric cooler that operates more efficiently than commercial refrigerants. The second is to convert waste heat directly into electricity [13].

Thermoelectric waste heat conversion is principally focused on the high temperature exhaust of industrial synthesis [76] (e.g., aluminum refining) and the medium temperature exhaust of automobiles [63]. In both these scenarios heat is rejected incidentally to the system's needs to reject the mass of the exhaust gas. Systems in which fast heat rejection or heat conservation is required are better served by heat exchange or insulation. These systems also generate heat in a manner that is geometrically inaccessible for higher efficiency heat engines based on the Rankine or Otto cycle. Thermoelectric conversion of high exergy industrial waste heat could provide approximately 10 TeraBTU/year of recovered energy in the United States alone [76].
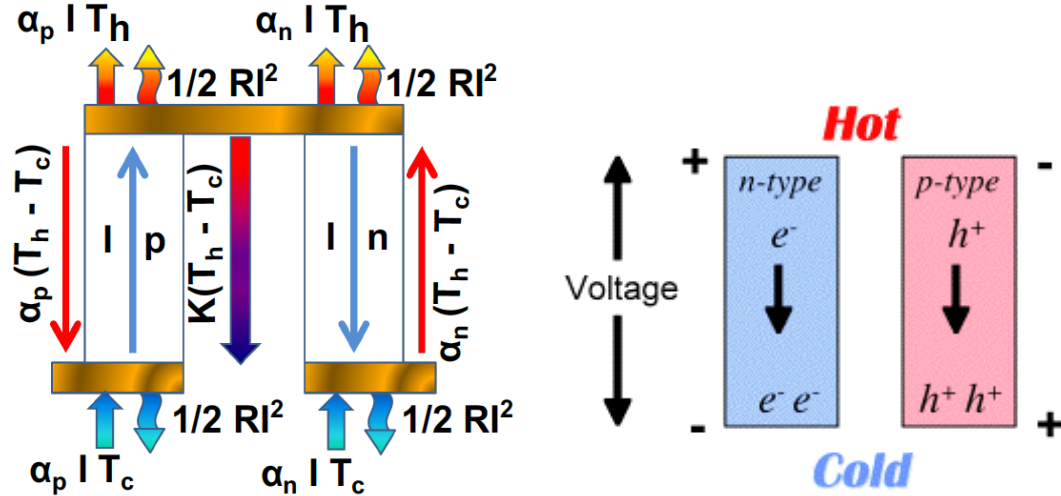
Figure 1.2: (a) Model of a thermoelectric unicouple including all electronic and thermal flows. (b) The thermoelectric effect is the result of thermodiffusion of charged carriers from the hot to cold end.

Conversion of automotive waste heat could improve fuel economy by 5% and thereby save a much larger 1 Quadrillion BTU/year [63], however device integration is more complicated due to the varied operational conditions of automobiles [104]. Therefore the typical strategy for development of thermoelectric waste heat generators is to demonstrate success in industrial applications and then integrate them into automobiles afterwards.

Thermoelectrics generators (TEGs) are compact, silent, and reliable. They are easily controlled with even simple linear PID systems [13]. For this reason they have seen use in a number of niche applications. The most important and famous of these are the Radioisotope Thermal Generators (RTGs) used to power NASA's deep space missions and its Mars Rovers [168]. In this application the compact size leads to an excellent performance on the Watts per Kilogram ratio essential for mass-limited satellite launches and the reliability ensures operation for multiple decades [202]. However, this application is not cost sensitive. Grid-scale energy conversion requires a good performance on a dollar per watt basis [203].

1.3 Thermoelectric Energy Conversion

The basic unit of a TEG is a unicouple, as depicted in Figure 1.2(a). It consists of two thermoelectric legs that are thermally in parallel and electrically in series. One of these two legs should conduct electrons (n-type) while the other conducts holes (p-type) [180]. An n-type leg will have a higher voltage at its hot side than its cold side, while the converse will be true for a p-type leg. The resulting voltage induces a current, and thereby provides power to an external load.

The voltage is induced by thermoelectric effect, as depicted in Figure 1.2(b). Charge carriers at the hot end of a material will tend to move faster and therefore diffuse quicker than species at the cold end of a material. Under a temperature gradient this results in transport to and build-up of charge carriers at the cold end of the material [67]. This process is referred to as thermodiffusion when the carriers are uncharged. In essence thermoelectric effects are thermodiffusive effects of charged particles [159]. The effects of thermodiffusion are known in a tangible sense from the transport of gas from hot regions to cold regions. The temperature gradient results in a pressure gradient and that induces a flow of particles colloquially referred to as wind.

Analogously, in a conducting material a temperature gradient induces an electrochemical potential gradient ($\tilde{\mu}_e$). That gradient in turn induces transport of particles [49]. The quantity $\frac{1}{q}\tilde{\mu}_e$ is known as the Galvani potential or voltage (V). (And not the Volta potential typically denoted by ϕ) [166]. Under open circuit operation the voltage and temperature are related by:

$$\alpha = \frac{\nabla V}{\nabla T} \tag{1.1}$$

Under closed circuit operation the voltage is diminished by the resistive flow of current. The quantity α (in many other documents denoted as S) is the *Seebeck* coefficient. Further detailed derivations of the Seebeck coefficient can be found in numerous sources [147, 32, 132, 69] Domenicali's work in particular is a detailed approach of

fundamental use to anybody working on thermoelectric metrology [49]. Below I also draw strongly on Goupil *et al.*'s excellent review [69, 83].

Clearly, a large induced voltage and therefore a large α is required for a good thermoelectric material. Intuitively, the power generated will be proportional to the voltage driving it squared, and so a figure-of-merit should include a α^2 dependence. As joule heating and conduction of heat are both dissipative it can be intuited that a large electrical conductivity (σ) and a small thermal conductivity (κ) are important for good thermoelectric performance. In fact, thermoelectric materials are judged on a combination of these properties and the material temperature (T) known as the thermoelectric Figure-of-Merit (zT) [69]:

$$zT = \frac{\alpha^2 \sigma}{\kappa} T \tag{1.2}$$

But what is the meaning of zT? How does it relate to the performance of a thermoelectric as a heat engine? The answer is simple to state but will require some explanation: zT is a measure of the *thermodynamic reversibility* of a thermoelectric material acting as a heat engine [19, 187]. A similar quantity can be derived for any coupled linear energy conversion process [150]. I will first develop the zT in sketch from equilibrium thermodynamics and then develop it explicitly from non-equillibrium thermodynamics.

In 1824 Sadi Carnot proposed that there was a fundamental limit to the efficiency of a heat engine [33]. This limit depended only on the temperature at its hot and cold end. Clausius determined this efficiency, thenceforth known as the *Carnot efficiency*, to be [38]:

$$\eta_c = 1 - \frac{T_c}{T_h} \tag{1.3}$$

This limit follows directly from the second law of thermodynamics. To paraphrase Max Planck's formulation [158], "the rate of entropy production of a heat engine is always equal to or greater than zero." At the Carnot efficiency the entropy production is equal to zero. The efficiency of any heat engine is the work (dW) done divided by the heat taken from the hot end (dQ_H). The work done is the difference in the heat

rejected from the hot end and the heat provided at the cold end:

$$dW \leq dQ_H - dQ_c \qquad (1.4)$$

With this and the relationship between entropy and heat, $dQ = TdS$, the efficiency of any heat engine may be stated as:

$$\eta \leq 1 - \frac{T_c dS_c}{T_h dS_h} \qquad (1.5)$$

The second law requirement of entropy production indicates that $dS_c \geq dS_h$ for a closed system. Therefore the limiting efficiency is η_c, as expressed in Equation 1.3. The reversibility may be defined as the ratio of entropy production required for the work done to the entropy produced dissipatively. For the perfectly reversible Carnot engine its value is infinity.

While Carnot was formulating his theory of heat engines, Thomas Johannes Seebeck was observing that by applying a temperature gradient he could deflect the needle of a compass [175, 176, 174]. A decade later Peltier determined that a current applied across the interface of a material carried a heat current [155]. William Thomson, later Lord Kelvin, integrated these effects with the nascent field of thermodynamics and postulated that the Peltier and Seebeck effect arose from the same physical effect [135]. The Seebeck coefficient was defined in Equation 1.1. The Peltier coefficient relates the reversible heat flux transported to the current applied as:

$$\pi = \alpha T = \frac{Q_R}{I}, \qquad (1.6)$$

where π is the Peltier coefficient and $\pi = \alpha T$ us the first Thomson relation [135].

From these relations the reversibility of a thermoelectric material can be found. Figure 1.3 shows a simplified thermoelectric consisting of only a single leg. If the second leg is of equal and opposite Seebeck coefficient and equal σ and κ, the analysis below is excact. Suppose the leg has a resistance $R = \frac{1}{\sigma}\frac{L}{A}$ and a thermal conductance $K = \kappa\frac{A}{L}$. If it is placed under a temperature gradient and connected electrically to a
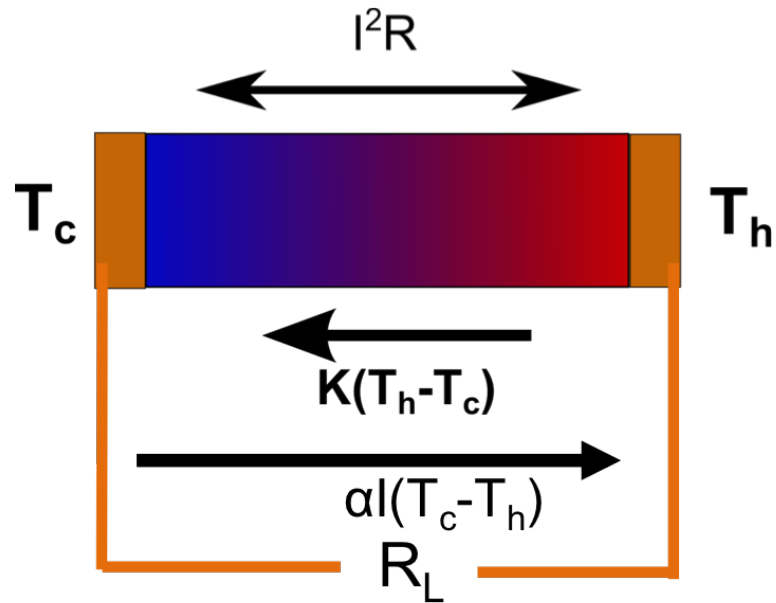
Figure 1.3: A single thermoelectric leg with all heat and thermal flows. The balance between dissipative thermal conductance and dissipative joule heating leads to constraints on the ideal geometry
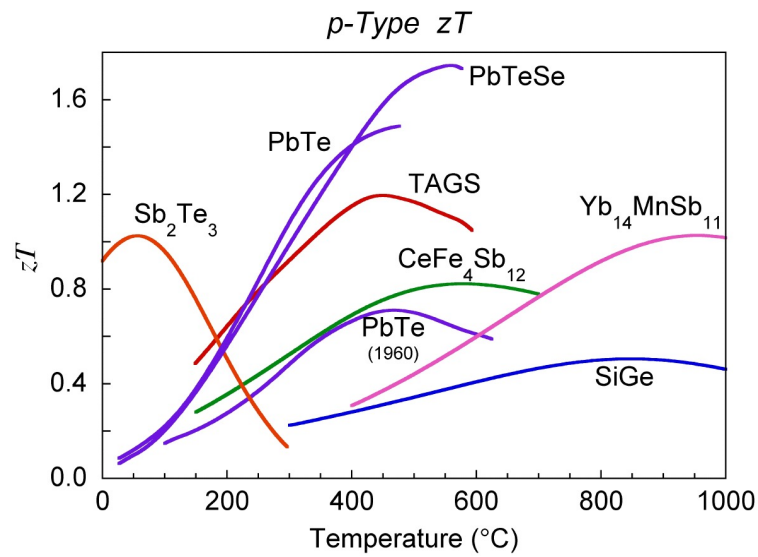
Figure 1.4: zT's for representative state of the art thermoelectric materials.

load of the same resistance, it will produce an electrical power of $V^2/R_L = \alpha^2 \Delta T^2/R$ while dissipating heat by joule heating ($I^2 R$) and Fourier law conduction $K\Delta T$. It will transport by the Peltier effect a quantity of heat equal to the power produced.

Define the thermal conductivity under no particle flow as κ_j and that under no voltage gradient as κ_e. Then the two thermal conductivities are related by $\kappa_e = \kappa_j + T\sigma\alpha^2$. When the ratio κ_e/κ_j is maximized the work produced per heat flow is maximized. This gives:

$$\frac{\kappa_e}{\kappa_j} = \frac{\alpha^2 \sigma}{\kappa_j} T + 1 \equiv 1 + zT, \tag{1.7}$$

in which maximizing zT therefore provides maximum power. Re-expressing the above as:

$$\frac{\kappa_e - \kappa_j}{\kappa_j} = zT \tag{1.8}$$

By this equation zT is the ratio of heat transformed in work by the Peltier effect to the heat that fluxes through the material. Therefore zT is a microscopic version of $\frac{dS_c dS_h}{dS_c}$ and a good representation of thermodynamic reversibility. The differential efficiency under these conditions is then:

$$d\eta = \frac{dT}{T} \frac{\sqrt{1 + zT} - 1}{\sqrt{1 + zT} + 1} \tag{1.9}$$

Therefore optimization of improved material zT is essential to increased device efficiency. Recent work on cost models of thermoelectric devices that includes devices costs such as a heat exchangers and metallization has shown that not only is high zT important for good device efficiency, it also is the most important factor for device cost — excepting perhaps thermoelectrics based on precious metals such as silver, gold, and rhodium. The mantra of thermoelectric material development may very well be stated as zT at any cost. [203, 117]

What are typical best values for material zT now and what values are necessary for widespread thermoelectric integration? A summary across a wide temperature range is shown in Figure 1.4; these are materials that have undergone rigorous device testing at JPL and should thus be considered as readily available for commercial
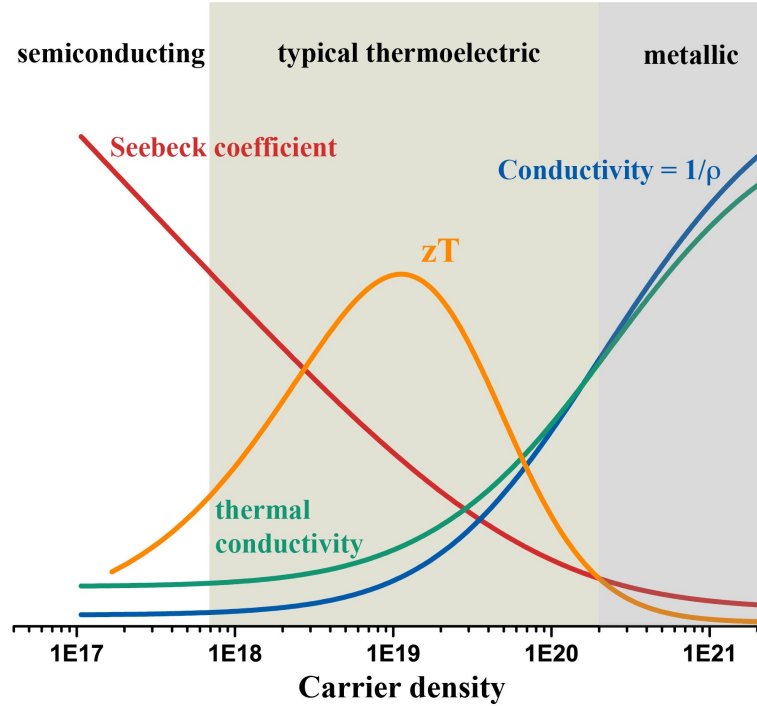
Figure 1.5: Variation of thermoelectric properties with carrier concentration as calculated with a single parabolic band model.

development. At multiple temperatures and for both charge carrier types a zT greater than unity is now available. Recent research has lead to development of materials with zT's that are potentially greater than 2, which is considered to be the threshold for device integration. While typically a publication is judged by the peak value of zT, a broad high zT across a wide temperature range is needed for commercial waste heat generation.

1.4 Entropy Co-Transport

In the previous section I defined Seebeck coefficient initially as the voltage gradient induced by a temperature gradient. However, I also noted the equivalence of the Seebeck effect and the Peltier effect that Thomson postulated and Onsager later proved explicitly from a microscopic approach based on fluctuation and dissipation. Equation 1.6 says that the Seebeck coefficient is the ratio of the reversible heat flux (Q_R) to the applied current (I) times the temperature. That is to say $\alpha = -\frac{S_R}{I}$ in

which S_R is the reversible entropy flux (the minus sign is by convention). If both numerator and denominator are divided by the number of carriers transported per unit time than [49]:

$$\alpha = -\frac{S^*}{q} \tag{1.10}$$

This equation is motivated explicitly from the Onsager formalism in the appendix. In it, S^* is the entropy transported per particle — an important quantity when considering thermodiffusive transport [132] — and q is the carrier charge. The negative sign in eq 1.10 is by convention. It ensures that p-type materials have a positive Seebeck and n-type materials a negative Seebeck. Naively, one might say that what is needed is simply to increase the entropy transported per electron; just as naively one might say that one ought increase the electronic conductivity while reducing the thermal conductivity. There is no a priori relation between the transport coefficient and thus a limit on zT. However, good thermoelectric materials are heavily doped semiconductors, and the three transport coefficients are related to one another by their particular material physics [128, 154].

The transport coefficients in typical thermoelectric materials are principally related by their electronic band structure. In this work I study materials that transport thermodynamic quantities other than charge carriers and entropy, and this co-transport appears to lead to both Seebeck and zT enhancement beyond that of the band structure, and so my treatment of band structure thermoelectrics will be brief. For a more thorough discussion of band structure engineering approach to enhancing zT, the review article of Pei *et al.* [154] and the CRC chapter by Andrew May and Jeff Synder [170] are excellent resources.

It is often convenient to rewrite zT in terms of the separate contributions of electrons and lattice vibrations (phonons) to zT:

$$zT = \frac{\alpha^2 \sigma}{\kappa_L + \kappa_e}, \tag{1.11}$$

in which κ_L and κ_e are the thermal conductivity contributions of the lattice and the electrons directly. The lattice thermal conductivity is purely dissipative and so ought

to be minimized [180]. The lower limit of it is that due to glass-like scattering [28, 29]. An intense subject of research over the last two decades has been to devise methods of scattering phonons to reduce κ_L without scattering electrons and thereby reducing σ. Reduction of κ_e is more difficult as it is fundamentally related to the electrical conductivity by the Wiedemann-Franz Law [100]:

$$\kappa_e = L\sigma T \tag{1.12}$$

In which L is the *Lorenz number* of the material. Though the Drude model value of $L_0 = 2.44 \times 10^{-8} W \cdot \Omega \cdot K^{-2}$ is seldom exactly right, it is not violated significantly above the Debye temperature [68]. Even in very low carrier concentration samples a Lorenz number is only 60% of L_0 [154]. Both κ_e and σ should increase as carrier concentration is increased. κ_e has a weaker relationship with the Seebeck coefficient. While κ_e represents the energy conducted by the kinetic energy of electrons, the Seebeck coefficient also includes the potential energy that is transported [67]. A simple way to conceptualize the Seebeck coefficients is to divide it into two terms as per Emin [49, 61]:

$$\alpha = \alpha_{presence} + \alpha_{transport} \tag{1.13}$$

The presence Seebeck is the entropy added by adding carrier without regards to how it came to be added. The contributions from its transport through the temperature gradient (*e.g.* scattering effects are contained in $\alpha_{transport}$). While the transport term is necessary for the full derivation, the presence term is far more didactic, as it can be derived using only equilibrium thermodynamics as [169]:

$$\alpha_{presence} = -\frac{dS}{qdN}, \tag{1.14}$$

where N is the number of particles. It can be re-expressed in terms of the entropy density (s) and the carrier concentration (n) as $\alpha_{presence} = -\frac{ds}{qdn}$. The very simplest limit of this is the case in which all electron states have the same energy, *i.e.*, that the band width is small compared to k_bT. This is called the Hubbard model [14, 138]. In

that case the presence Seebeck is due only to a change in entropy of mixing:

$$S_{mixing} = -Nk_b \left(c \ln(c) - (1-c) \ln(1-c) \right), \tag{1.15}$$

in which c is the concentration of carriers relative to sites. From this the Heikes formula for thermopower may be derived [135]:

$$\alpha_p = -\frac{dS}{qdN} = \frac{k_B}{q} \ln \left(\frac{c}{1-c} \right) \tag{1.16}$$

The Heikes formula gives a large magnitude of Seebeck if c is small or c is near unity. For c small the dominant carrier is electrons (n-type) and for c large it is holes (p-type). Therefore the Seebeck decreases with increasing carrier concentration. This trend is depicted in Figure 1.5, along with the corresponding trends in κ and σ. As a result of the differing carrier concentration dependence of α, κ, and σ, there is a zT peak at heavily doped carrier concentrations. A typical approach is to find a material with an electronic band structure in which the zT peak is high and attempt to dope it to the appropriate carrier concentration.

The band structure limited peak in zT only applies if electrons and heat are the only thermodynamic fluxes that show transport. Co-transport of another flux may lead to an enhancement in the entropy transported and therefore an increase in zT. Without loss of generality, let us call the additional thermodynamic flux that transports, J_m, and its corresponding equilibrium thermodynamic property, m. It will also transport entropy with quantity S_m^* per unit of m. Its thermodiffusion will have a presence contribution given by:

$$S_{m_p resence}^* = \frac{dS}{dm} \tag{1.17}$$

In the presence limit the amount of m transported per a quantity of charge carrier transported is $\frac{dm}{qdN}$. Therefore the entropy co-transport provides an additional contribution to Seebeck of:

$$\Delta\alpha = -\frac{1}{q} \frac{dS}{dm} \frac{dm}{dn} \tag{1.18}$$

The additional negative sign is again due to the sign convention relating α and S^*. Though this expression in Equation 1.18 was not rigorously derived, a similar expression can determined from the Onsager phenomenological equations. From that expression Equation 1.18 can again be motivated with better grounding in non-equillibrium thermodynamics. That derivation can be found in Chapter 8.

Such entropy co-transport has been previously observed in three different types of material systems. Vibrational entropy co-transport has been observed in Boron Carbide [61, 7], lattice spin entropy co-transport has been in observed in Na_xCoO_2 [110, 109], and lattice entropy co-transport has been observed in phonon-drag systems [148]. In the case of Na_xCoO_2, for example, the differing spin degeneracy of electron-occupied and electron-unoccupied cobalt sites provides the mechanism for this coupling of carrier transport to entropy transport [196]. However, this strategy has thus far been limited to small changes in spin degrees of freedom of single ions; it remains an open question whether structures with more spin degrees of freedom can be coupled to charge transport.

Here we consider coupling the carrier transport to degrees of freedom associated with the entropy associated with an order-disorder phase transition. A phase transition is always associated with an entropy change because there is always a concurrent transformation in system symmetries [162]. If the entropy change of a continuous phase transition can be associated with carrier transport, a substantial enhancement in Seebeck may be obtainable. The number of degrees of freedom associated with a structural transformation scales as the number of atoms in the system rather than the number of carriers. For a typical thermoelectric material with a carrier concentration of $10^{20}\,cm^{-3}$, there are 100 times as many atoms as there are charge carriers. Thus the potential Seebeck enhancement by this mechanism may be extremely large. Because phase transitions occur at a discrete temperature, it is relatively simple to distinguish the anomalous enhancement due to ordering entropy co-transport from the band structure contribution. In a material without a phase transition such enhancements may be misattributed to the band structure through incorrect determination of one of the band parameters.
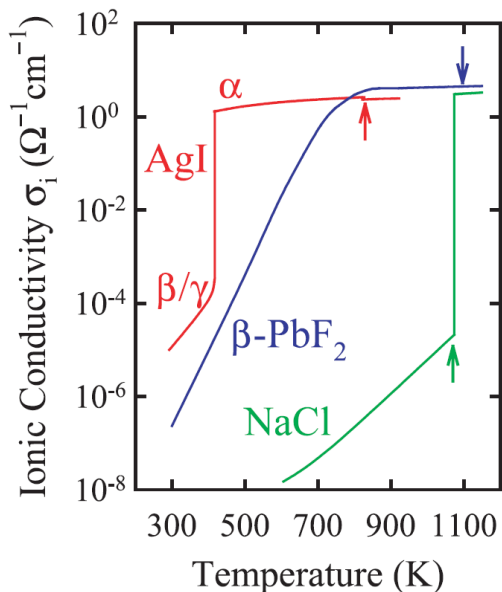
Figure 1.6: Ion conductivity of type I super-ionic AgI, type II super-ionic PbF$_2$, and the non-superionic NaCl. Arrow indicates the melting temperature. Superionics have a liquid-like ion conductivity while in the solid phase. Image credit to [87].

1.5 Super-ionic Thermoelectrics

Mixed ion-electron conductors are of recent and increased interest as thermoelectric materials. Though there is long-standing work on the Zn ion conductor Zn$_4$Sb$_3$ [204], recent results have sparked interest in mono-valent coinage metal chalcogenides such as Ag$_2$Se [136, 64, 199, 133], Ag$_2$Te [50, 178], and Cu$_2$Se [84, 122]. These materials all have ion conductivity greater than 1 S/cm at elevated temperatures [21, 87], which qualifies them phenomenologically as super-ionic conductors as defined by Rice and Roth [163]. This is a classification rather than a definition and so it is not held uniformly. Sometimes a material with ion conductivity one to three orders of magnitude smaller is called super-ionic due to its resemblance in structure and behavior to canonical super-ionics. The ion conductivity of 1S/cm is similar to that of a molten salt [87, 70, 34]. For this reason the super-ionic materials are often spoken of as having a molten sublattice. For example, in the Ag$^+$ conductor AgI the I$^-$ are taken to be in a rigid cage, while the Ag$^-$ is free to travel [97].

Why are these materials of such interest as thermoelectrics? Because their lattice

thermal conductivity is extremely low. For example, in $Ag_2Se_{0.05}Te_{0.05}$ it is only $0.5\,W/mK$ at 400 K [50] and Ag_8GeTe_6 has been reported as having a lattice thermal conductivity of $0.25W/mK$ at $300K$ with only negligible contribution from electrons. This thermal conductivity is almost certainly at or below the glassy limit proposed by David Cahill.

Super-ionics were divided into three categories by Pardee and Mahan [151] based on the manner by which the super-ionic state is achieved. Their classification system superceded an earlier system based on chemical composition and structure instead of phenomenological behavior. The dependence of ionic conductivity on temperature is plotted for prototypical members of each superionic classification in Figure 1.6. In type I superionics such as AgI [97], the ionic conductivity increases suddenly at a phase transition temperature. In type II superionic such as PbF_2 [86], the ionic conductivity increases continuously but super-exponentially to a phase transition temperature. Type III super-ionics such as $Na - \beta - Al_2O_3$, the ionic conductivity increases according to an Arrhenius behavior with no phase transition.

The super-ionic phase transition is of particular interest to this study. Type I and type II super-ionic conductors are characterized by a structural phase transition with an entropy change close to that of melting (*i.e.*, order $10\,J \cdot K^{-1} \cdot mol^{-1}$) and a concurrent increase in ion conductivity [151]. For type I super-ionic conductors there is a sudden enthalpy release at the phase transition temperature (*i.e.*, a first order phase transition) and a concurrent discontinuous increase in ionic conductivity. For type II super-ionic conductors the ionic conductivity increases super-exponentially up to the phase transition temperature, the structure changes continuously, and there is a lambda-shaped peak in heat capacity like that characteristic of a second order phase transition [87]. In the final chapter of this work I will show that Ag_2Se is a type I super-ionic, while Cu_2Se is a type II super-ionic. This difference is essential to understanding their behavior in their ordered phases just below their respective super-ionic phase transitions.

1.6   Key Challenges and Results

Having outlined the motivations for this study, I should also present a brief outline of
the thesis. In the course of thesis I had to overcome a number of challenges in order
to come to my conclusions, and I had to develop a broad theoretical understanding
to interpret my data. I needed to measure the chemical and transport properties of
these materials, see Chapter 2. Metrology of the Seebeck coefficient near phase tran-
sitions was a particularly challenging part of the work for which new methodology
was developed, see Chapter 3. The most common question I faced with respect to
the applicability of my work to real thermoelectric device was whether ion conducting
materials would be stable under applied current. In Chapter 4 I examine this ques-
tion both by a review of a past attempt by JPL and the DOE to use $Cu_{1.97}Ag_{0.03}Se$
as a super-ionic material and through experimental tests designed to simulate de-
vice conditions. Determination of the nature of the phase transition is particularly
important to this work. In the course of this work we proved that contrary to all
previously published literature, Cu_2Ses phase transition is second order not first or-
der, see Chapter 5. This understanding was crucial to calculating correctly its zT. In
Chapter 6 I report my data and analysis of the transport behavior of Ag_2Se. I also
give an overview of why super-ionics are of interest as thermoelectrics and of band
structure modeling of thermoelectrics. In Chapter 7 I introduce the concept of en-
tropy co-transport as means of enhancing thermoelectric performance, and I present
the transport data and analysis of both Cu_2Se and $Cu_{1.97}Ag_{0.03}Se$. In the final chapter
I integrate my results and a full phenomenological explanation of the thermoelectric
enhancement of Ag_2Se and Cu_2Se. From the basis of this hypothesis a series of future
experimental goals are proposed.

Chapter 2

Experimental Methods

This chapter discusses the basic methods used to characterize the materials in this study with the exception of Seebeck coefficient metrology, which is described in detail in Chapter 3.

2.1 Transport Measurements

Thermoelectric materials are characterized by the figure-of-merit zT. In the introduction I discussed the thermodynamic meaning of zT. However, that is only one half of its utility. The other half is that it is composed of material properties which are readily measured. We have:

$$zT = \frac{\sigma \alpha^2}{\kappa} T \tag{2.1}$$

In this work κ was not measured directly. Instead the thermal conductivity is expressed as:

$$\kappa = \rho D_t c_p \tag{2.2}$$

And each component of Equation 2.2 is measured separately. To obtain zT six quantities must be measured: ρ, D_T, α, σ, c_p, and T. Additionally, for characterization of the band structure properties the Hall coefficient (R_H) is measured. From R_H and σ it is possible to determine the Hall carrier concentration (n_H) and the Hall mobility (μ_H). These quantities are macroscopic measurements of the band structure and can be used to determine its form.
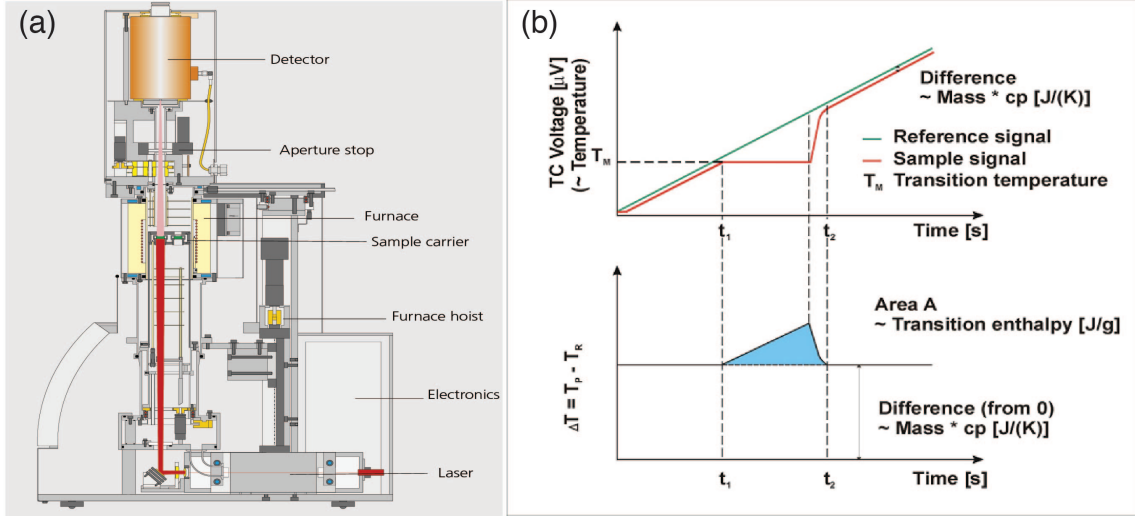
Figure 2.1: Schematic (a) of laser flash apparatus (LFA) and graphical representation of differential scanning calorimetry. (DSC) Image credit to Netzch Corporation.

Thermal diffusivity (D_T) was measured via the laser flash method. In this method a laser is pulsed upon the sample quickly, and the temperature on the other side is measured as a function of time. By fitting the temperature rise data a thermal diffusivity can be obtained. The timescale of the laser pulse must be much smaller than the rise time. The measurements presented in this thesis were measured using a Netzsch LFA (Laser Flash Analysis) 457 MicroFlash apparatus, see Figure 2.1.

The density (ρ) was measured by direct geometry. Measured samples typically have a regular geometry — either a rectangular prism or a cylinder. By measuring these regular dimensions with a pair of calipers or a micrometer the volume can be calculated. The sample mass is then measured on a calibrated scale. From measured mass and volume the geometric density is calculated.

Differential scanning calorimetry was used to obtain the specific heat capacity using a Netzsch DSC 404. In the case of Cu_2Se the measurements were confirmed using a Quantum Design PPMS. The measurements are courtesy of Huili Liu and Xun Shi of the Shanghai Institute of Ceramics at the Chinese Academy of Sciences (SIC-CAS) and also of Pawan Gogna of the JPL Thermoelectrics Group. The working principle of DSC is to increase the temperature of a heat bath in contact with both a sample and a reference at a constant rate. Due to the fixed rate of heat transfer there

Figure 2.2: Resistivity and Hall coefficient were measured by the four point Van der Pauw method. Image courtesy of Heng Wang.

will be a lag in the measured temperature of a sample that is proportional to its heat capacity, see Figure 2.1. The PPMS c_p measurement is similar except quasi-static. The sample is brought to a stable temperature and then a reservoir temperature pulse is applied while the sample temperature deviation is measured.

Two Van der Pauw geometry resistivity systems were used in this study to obtain σ, n_H and μ_H. Both systems are of identical design. A system with a 1 T magnet at the JPL thermoelectrics group was used to obtain the Hall data for Cu_2Se; all other data was obtained with a 2 T system at Caltech. The design and function of these particular systems is described in a recent publication by Borup *et al.* [20].

The Hall coefficient is measured by applying a magnetic field, measuring the voltage, and applying a current in three orthogonal directions. In Figure 2.2 the mangetic field would be applied through the sample, while the current is applied from lead 1 to lead 3 and voltage measured from lead 2 to 4. The current direction and leads used were alternated in accordance with the Van der Pauw resistivity method. The measurement were made at both positive and negative applied field to eliminate magnetoresistive offsets. In the case of a single carrier the Hall resistance is related to the carrier concentration by [160]:

$$R_H = \frac{1}{nq} \qquad (2.3)$$

If there are carriers of multiple type their contribution to the Hall resistance will depend on the applied field (B) as detailed in Jaworski *et al.* [92] and a recent publication I authored [25]. Though the full expansion is extremely complicated, for

either the limit of $B \gg \mu^{-1}$ or $B \ll \mu^{-1}$ the form is much simpler. This condition corresponds to whether the carrier velocity is primarily due to electron drift (small B) or cyclotron acceleration (large B). The high field limit is:

$$R_H = \frac{1}{n_1 q_1 + n_2 q_2} \tag{2.4}$$

While the low field limit is:

$$R_H = \frac{n_1 \mu_1^2 + n_2 \mu_2^2}{(n_1 q_1 \mu_1 + n_2 q_2 \mu_2)^2} \tag{2.5}$$

In the low-B limit R_H is dependent on the square of carrier mobility, while in the high-B limit it only depends linearly on band mobility. Therefore if there is a high mobility minority carrier and a low mobility majority carrier, the minority carrier will dominate the behavior at low-B while the majority carrier dominates at high-B.

Sample	α	σ	D_T	C_p
Ag_2Se	0	15	15	0
Cu_2Se	0	10	5	0
$Cu_{1.97}Ag_{0.03}Se$	0	15	15	0

Table 2.1: Temperature Shifts for Transport Properties

The instruments described in this chapter are designed for typical thermoelectric samples in which transport properties have slowly varying temperature dependences. A temperature misreading of 10 K or 20 K will have no noticeable effect on the progression of zT in such materials. Near the phase transition it can lead to crucial misinterpretation of the results.

The abruptness of the phase transition allows a ready means of determing the actual offsets. The temperatue of the phase transition in Seebeck was taken as the phase transition temperture. In a Seebeck measurement care is taken in instrument design to ensure that the temperature measured is that of the sample. Two thermocouples are used, which allows determination of thermocouple failure through comparison. Finally the Seebeck measurement is path independent [49] — the voltage only depends on the temperatures at the meaurement points without regard for temperature

irregularities in the sample. This contrasts to the volumetric measurements of D_T, c_p, and σ.

The temperature peak of heat capacity agreed with where the transition temperature determined by Seebeck measurement. The temperature offset in thermal diffusivity was due to misplacement of the measurement thermocouple. By moving the thermocouple into position the error could be reduced substantially. An encapsulated sample of Indium was measured during thermal diffusivity and the difference between its observed temperature of melting and its literature value (156.6 °C) was used to confirm the calibration. Electrical conductivity could not be checked the same way, and its calibration could not be confirmed. The values of these calibrations are in table 2.1.

2.2 Synthesis

The samples measured for this thesis were synthesized by Tristan Day at Caltech. A more detailed report on their synthesis will be available in his Ph.D. thesis (expected publication 2015). Ingots of Cu_2Se and $Cu_{1.97}Ag_{0.03}Se$ were prepared from mixtures of copper shot (Alfa Aesar, Puratronic, 99.999% pure on a metals basis), silver shot (Alfa Aesar, Puratronic, 99.999% pure on a metals basis), and selenium shot (Alfa Aesar, Puratronic, 99.999% pure on a metals basis) in stoichiometric ratios. The mixtures were placed in carbon-coated quartz ampoules evacuated to a pressure of less than 5×10^{-5} torr. The ampoules were heated to 1273 K at 100 K/hr and held at that temperature for five days. The ampoules were cooled to 973 K and annealed for three days, after which the ampoules were quenched in water. The ingots were then ball-milled. The resulting powder was hot-pressed [116] at 40 MPa and 923 K for five hours under argon flow. The pressed pellets were then cooled to room temperature at a rate of 5 K/min to avoid cracking.

Ag_2Se polycrystalline ingots were prepared by melting Ag (shot, 99.9999% pure, Alfa Aesar, Puratronic) and Se (shot, 99.999% pure, Alfa Aesar, Puratronic) in the desired mass ratios inside fused quartz ampoules evacuated to less than $6 \times 10^{-5} torr$.

The elements were slowly brought to 1273 K, held at that temperature for 12 hours, cooled to 973 K over three hours, annealed at 973 K for three days, then quenched in water. Disk-shaped samples were cut from the ingots and used directly for the experiments.

2.3 Chemical Characterization

X-ray diffractometry was performed with the assistance of Kasper Borup, Sebastian Christensen, and Bo B. Iversen of Aarhus University. PXRD was performed using a Rigaku SmartLab diffractometer configured with a Cu Kα source and a Rigaku D/tex detector. Temperature were performed using the same system and an Anton-Paar DHS-1100 furnace. The FullProf software suite was used for the refinements. X-ray diffraction allowed confirmation of composition by crystallography. Temperature resolved crystallography was used to determine the nature of the phase transition.

The Pair Distribution Function (p.d.f.) derived from total scattering measurements was performed on Cu$_2$Se to further elucidate the nature of the phase transition. The data was collected at beamline 11-ID-B, APS and analyzed by Sebastian Christensen. The utilized wavelength was $\lambda = 0.2128\,\text{Å}$ giving a $Q_{max} = 26\,\text{Å}^{-1}$. Samples were packed in 1.1 mm glass capillary within a glove box and sealed using epoxy glue. A dataset was obtained for every ≈ 5 K. Data collection time per dataset was 1 minute. Data was collected at equivalent temperatures on an empty capillary for background subtraction. Data was integrated using Fit2D. All datasets needed to be normalized to the incoming intensity because the ring was in decay mode during the experiment. The reduced pair distribution function, $g(r)$ was calculated by PDFgetX3. For the calculation we chose: $q_{min} = 0.8\,\text{Å}^{-1}$ and $q_{max} = 26\,\text{Å}^{-1}$.

Secondary measurements were performed via scanning electron microscopy (SEM) and electron probe microanalysis (EPMA). Wavelength dispersive spectroscopy (WDS) and energy dispersive spectroscopy (EDS) were performed respectively during EPMA and SEM. SEM (ZEISS 1550 VP) and EDS of Ag$_2$Se and Cu$_2$Se indicated them to be phase pure. EPMA and WDS were performed by Tristan Day with assistance from

Figure 2.3: Electron micrographs of $Cu_{1.97}Ag_{0.03}Se$ (a) and Cu_2Se (b). Black features are cavities. While Cu_2Se is single phase, $Cu_{1.97}Ag_{0.03}Se$ has inclusions of a silver rich phase (white) identified as CuAgSe by crystallography.
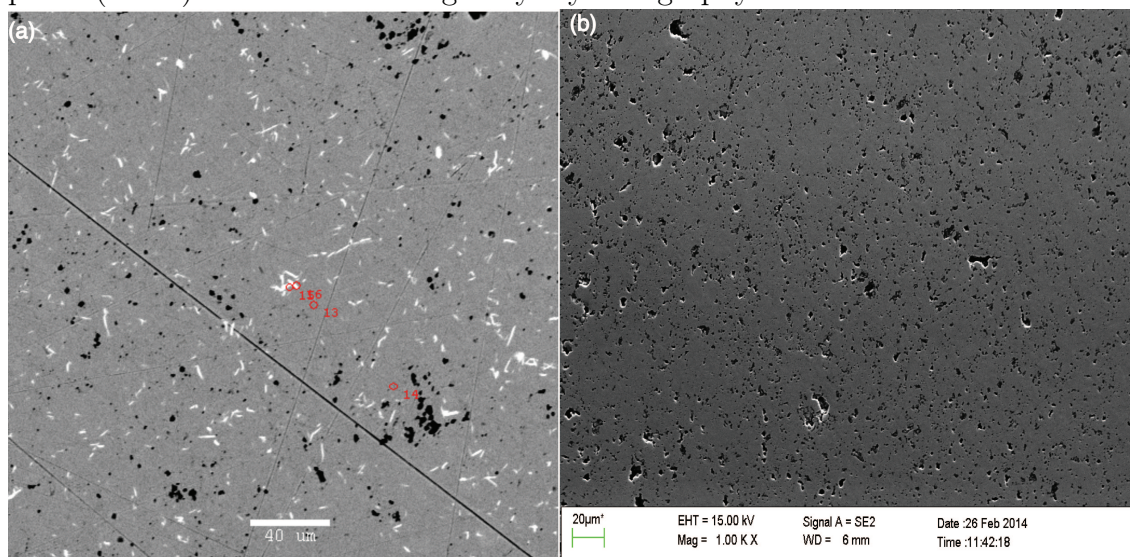
Dr. Chi Ma using a JEOL JXA-8200. WDS is considered to be more accurate than EDS and this advantage is amplified by the careful calibration to standards of the WDS detector. WDS on Cu_2Se confirmed the sample to be stoichiometric within the uncertainty of the measurement (0.5%). However, SEM of Cu_2Se indicated the presence of small cavities along the surface, see Figure 2.3(b). These cavities have been observed previously and identified as being from cavitation of Cu_2O and Se_2O_3 from trace oxygen in the material [101]. Any such oxygen secondary phase is undetectable by WDS due to the surface morphology and was also below the quantity for detection in any of the many X-ray measurements done during my studies. $Cu_{1.97}Ag_{0.03}$ shows a secondary silver rich phase that is identified as CuAgSe, see Figure 2.3(a).

Chapter 3

Seebeck Metrology

The Seebeck coefficient is unique to the metrology of thermoelectric materials. While the purely thermal transport properties (c_p, D_T, and κ) and the electrical properties measured using the Van der Pauw method (n_H, σ, and μ_H) are essential to thermoelectric characterization, they are also essential to other fields of scientific inquiry. For this reason Seebeck metrology is far less advanced and far less understood than that of the other variables, though great effort is being made by many to rectify that shortcoming. [47, 130, 94, 90]

On my first day working at the Caltech Thermoelectrics Group I was introduced to a moth-balled pair of Seebeck metrology devices and asked to restore them to full functionality. I spent many hours calibrating these systems and I eventually constructed my own Seebeck measurement system with the help of my undergraduate assistant David Neff. Over this time I learned many of the details and potential failings of Seebeck metrology.

This understanding of Seebeck metrology was essential to the work presented in this thesis. The materials that I studied were substantially more difficult to measure than typical thermoelectric materials. The Seebeck coefficient has a much stronger first and second temperature derivative near its phase transition temperature, requiring greater stability and resolution. To illustrate this I plot in Figure 3.1 both the Seebeck coefficients of Cu_2Se and $Na_{0.01}Pb_{0.99}Te$ [153] on the same axis.

The presence of the phase transition itself warrants more detailed investigation. The structural transformations of a phase transformation may be associated with
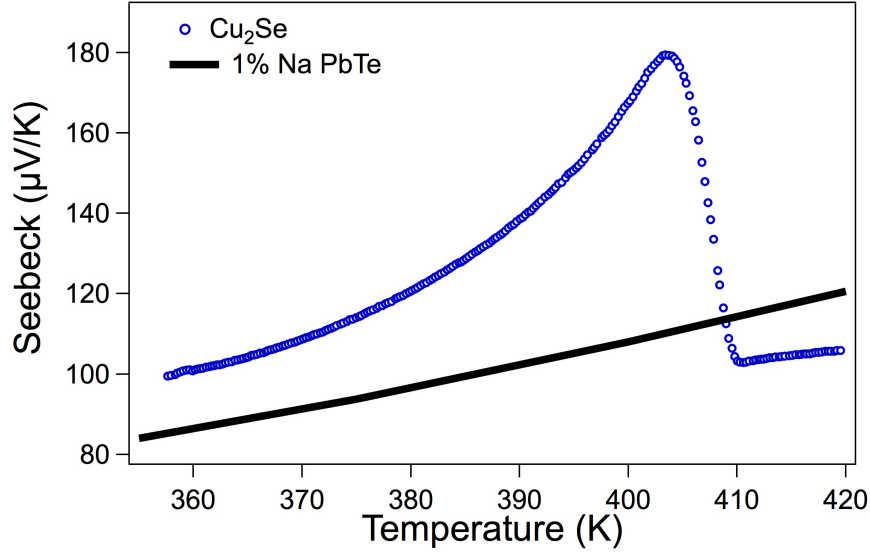
Figure 3.1: Seebeck coefficient of Cu_2Se compared with that of $Na_{0.01}Pb_{0.99}Te$. Cu_2Se's strong peak near its phase transition requires more precise measurement than is typical for thermoelectric materials. PbTe data courtesy of Yanzhong Pei [153].

time dependent kinetics. These time dependent kinetics may result in chimerical transport properties.

3.1 Measuring the Seebeck Coefficient

The essence of a Seebeck measurement is to measure the voltage difference (ΔV) across a sample under a fixed temperature gradient (ΔT) at some fixed temperature $\bar{T}$. The Seebeck coefficient (α) is then taken as $\Delta V/\Delta T$; this quantity I shall sometimes refer to as the *nominal Seebeck coefficient* or α_m. By convention ΔV is defined at the voltage on the cold side minus the voltage on the hot side, while $\Delta T = T_h - T_c$. Both the voltage and temperature are measured at the same nominal point on the sample. This is done by pressing one thermocouple onto a hotter point of the sample and one thermocouple onto a colder point on the sample, see Figure 3.2. The Seebeck coefficient is, as defined in Equation 1.1 is actually the ratio of the *gradients* of V and T. Single point Seebeck measurements are therefore an approximation to $\Delta V/\Delta T \approx \nabla V/\nabla T$. This may cause an error and these errors are discussed in the context of typical metrology techniques below in reference to Cu_2Se. It will be shown

Cold   **Hot**

Thermocouple 1   Thermocouple 2

$$\alpha = \frac{\Delta V}{\Delta T}$$
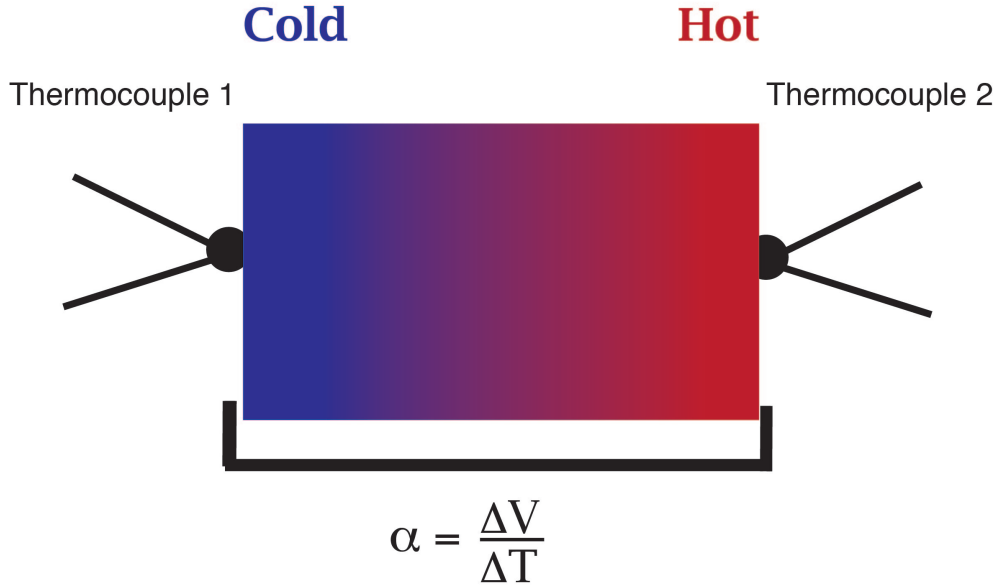
Figure 3.2: Schematic of a Seebeck measurement. Two thermocouples are placed at two different points on a sample. Both ΔT and ΔV are measured with the thermocouples. In a single point measurement $\Delta V/\Delta T$ is taken as the Seebeck coefficient.

that these errors are of greater concern near the super-ionic phase transitions studied for this thesis.

A more pernicious and frequently large error is the small voltage measured even when $\Delta T = 0$ [90, 129]. This offset is colloquially referred to as the dark voltage, V_D, though one should not be misled into thinking it is a voltage error. It may be caused by error in temperature measurement. That quantity I refer to as the dark temperature. It is defined as the ΔT for which $\Delta V = 0$ and is related to V_D by $T_D = V_D/\alpha$. The intercept error, whether formulated as T_D or V_D, is problematic for single point Seebeck measurements. The error induced is determined by:

$$\alpha_m = \alpha \left(1 + \frac{T_D}{\Delta T} \right) \tag{3.1}$$

Because of this error single point Seebeck metrology is no longer used. An example is discussed in section 3.3 in the context of Cu_2Se [144].

To compensate for these variations on the *oscillation* Seebeck measurement is
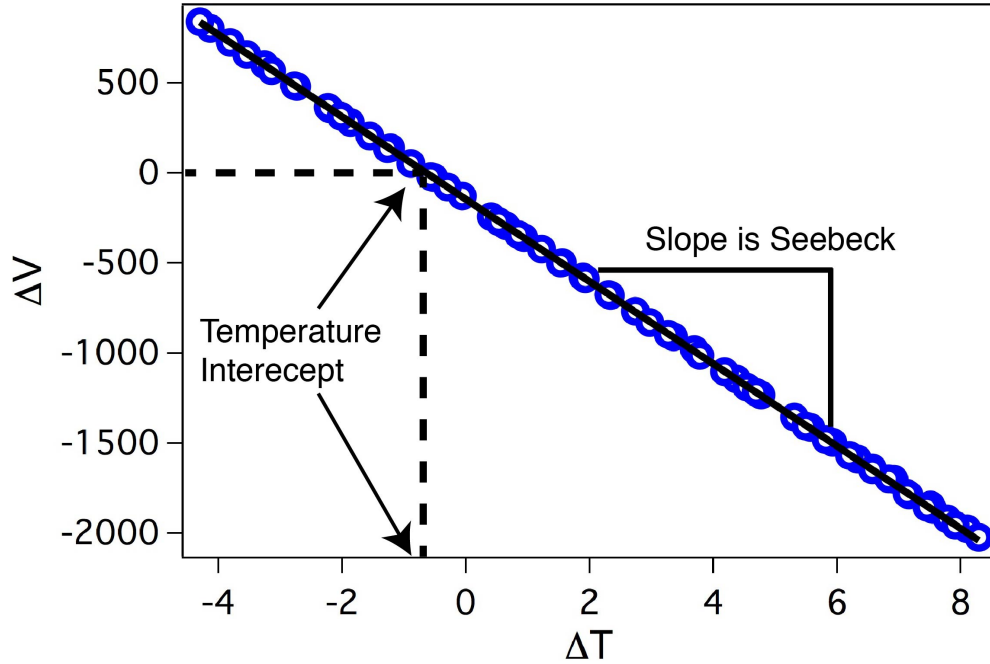
Figure 3.3: Raw Seebeck data from an oscillation sequence. The slope of the data is taken as the Seebeck coefficient.

now used almost universally [47, 94]. In this technique ΔT is varied while $\bar{T}$ is held constant and ΔV is measured. The resulting data is plotted as in Figure 3.3 and a line fit to it. This compensates for T_D, which is the intercept of such a plot. The slope of that line is taken α, though errors other than T_D may still effect its value. These issues are discussed more explicitly later in this chapter.

Measuring Seebeck coefficient correctly is technically challenging partially due to a lack of standardized samples. Though many metals used in thermocouples are well calibrated, they have relatively low Seebeck coefficient (e.g., $10\,\mu$V/K) and high thermal conductivity (e.g., $50\,$W/m $\cdot$ K). Good thermoelectrics have a much higher Seebeck (e.g $\alpha > 100\,\mu$V/K) and lower thermal conductivity ($\kappa < 3\,/m \cdot K$). Due to the great mismatch between the thermal conductivities of metals and good thermoelectrics, an apparatus designed for one will be inappropriate for the other. Round robin testing has lead to the development of a Bi_2Te_3 standard below 400 K [124, 126, 125]. No such standard is available at higher temperatures, though such standards are under current development at both NIST [125, 131] and ORNL [195].

The Seebeck of Bi_2Te_3 standard varied by 5% from lab to lab during the round-robin test [124], and I take this as the current upper limit of accuracy for Seebeck metrology.

The lack of standards for Seebeck measurement means care must be taken in instrumentation design. A Seebeck measurement may have low Gaussian noise but still exhibit large systematic errors. For example, Dr. Joshua Martin at NIST has made a strong case that instruments designed using an infrared furnace, such as that of the commercially available ULVAC ZEM-3 and Linseis LSR-3, produce repeatable errors in Seebeck measurement [94]. Dr. Johaness de Boor of DLR in Germany found that systematic error may be present in data for which the linear fit has $1 - R^2 < .01$; further order of magnitude reductions in the deviation of R^2 from unity resulted in systematically improved data [47]. Correct apparatus design is therefore crucial for accurate Seebeck metrology.

The principle challenge of Seebeck measurement is accurate thermal measurement rather than accurate voltage measurements. Determination of the electrical contact to be ohmic and small is insufficient for determination of good thermal contact [94]. In making a Seebeck measurement it is assumed that the temperature of the thermocouple is the temperature at a particular point on the sample. If there is a combination of heat flux to or through the thermocouple and a thermal resistance from the sample point to the measurement point on the thermocouple, then an error will result. Because the heat flux through the thermocouple tip is driven by the system's various parasitic couplings to low or ambient temperature, this is referred to as the *cold finger effect*. A good Seebeck metrology apparatus reduces the cold finger effect.

There are three standards designs (Figure 3.4) of a thermocouple measurement apparatus commonly used today. The first is the *two point* design, in which the sample is sandwiched between electrically conductive heater blocks and the electrical and thermal properties measured from within the blocks. The second is the *four point linear* design in which the thermocouples touch the sample from its side instead of being inside the heater block. The final design, which was created by NASA JPL in support of their radio-isotope thermal generator program [90], is the *four point co-linear* design. Like in the four point design, the thermocouples directly touch the
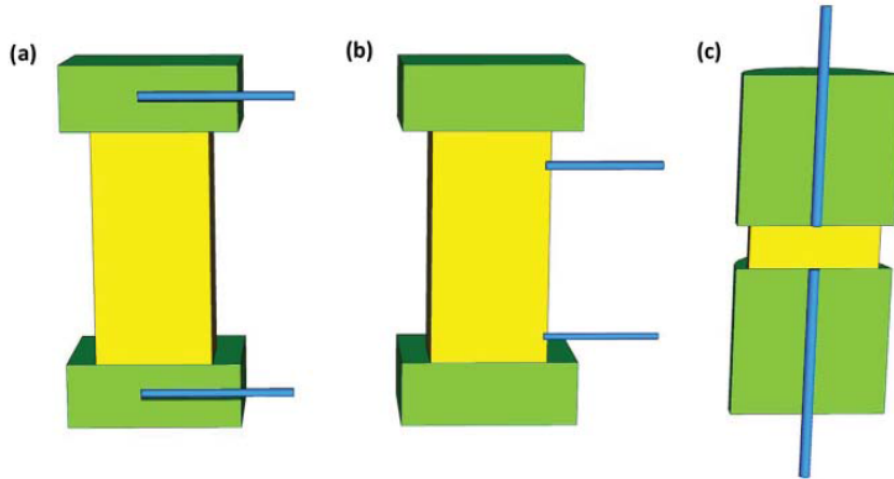
Figure 3.4: The three principle Seebeck geometries. Sample is shown in yellow, heater block in green, and thermocouple in blue. (a) the two point linear design. (b) the four point linear design. (c) the four point co-linear design. Image adapted from Iwanaga *et al.* [90].

sample, but here they pass through the heater block. The four point co-linear design was used for this experiment.

The two point design (Figure 3.4(a)) is the most traditional as it is relatively easy to construct. In this design the thermocouple can be extremely well thermalized to the block and that should mitigate its coupling to cold or ambient temperatures. However, while the thermalization with the heater block is excellent, the thermalization to the sample itself is problematic. As a result, two point designs consistently over-estimate ΔT and therefore under-estimate the Seebeck coefficient. The apparatus used in this experiment had thermocouples both in the heater block approximately 1 cm from the sample and thermcouples in direct contact with the sample. As shown in Figure 3.5, the thermocouples in the heater block had a small offset from those touching the sample. Although it only causes a small error in absolute temperature, there is a much more significant (30% here) difference between the ΔT in the blocks and at the sample.

The four point linear design (Figure 3.4(b)) is used in commercial systems such as the ULVAC ZEM-3 and Linseis LSR-3. It is popular because it can be used for
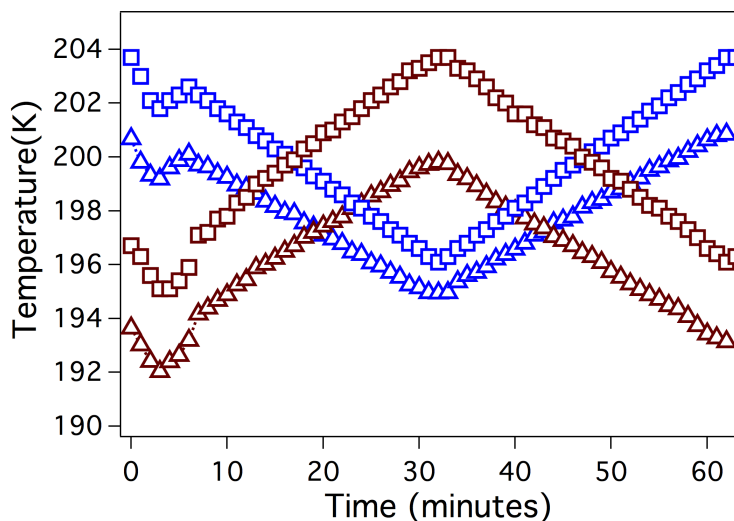
Figure 3.5: Temperature readings on the sample and in the block as ΔT is varied. Magenta represents thermocouples on the top side. Blue represents thermocouples on the bottoms side. Squares represent thermocouples in the heater block while triangles represent thermocouples in direct contact with the sample.

near simultaneous measurement of electrical conductivity and Seebeck coefficient. Its principle flaw is the cold finger effect. The thermocouples do not run through the heater block and so are thermalized via their signal path to the ambient environment. While in theory this may be mediated by heat sinking the thermocouple wires to a hot block, in practice these instruments are only thermalized using an infrared furnace. As a result they tend to underestimate ΔT and therefore overestimate Seebeck. Work at NIST constructing a system with the same configuration found that an overestimate of up to 15% in Seebeck coefficient may result at high temperatures [94] This casts into doubt some of the highest zTs reported as very many of them were measured on ZEM-3s.

The four point co-linear design (Figure 3.4(c)) is meant to include the best features of the other two designs without their defects. The thermocouples contact the sample without intermediation by the heater block as in the four point linear design. The thermcouples are well heat sunk into the heater block itself, as in the two point design. Together these should mitigate both the thermal resistance from sample to thermocouple and minimize the heat flux from the thermocouple into the bath.

However, there may still be temperature fluxes through the thermocouple if there are non-uniformities in the temperature of the block. Such differences have been observed in our apparatus, see Figure 3.5. The temperature difference is in the block in that measurement was 30% higher than that at the sample surface.

A simple method for improving thermal contact is the use of a thin graphite-base foil (brand name *grafoil*) between the sample and the pair of block and thermocouples. Due to the conformation of the flexible foil to both sample and thermocouple, the effective thermal contact area is increased and thermal contact resistance decreased. Furthermore, the improved thermal contacts between the heater block and the sample ensure that the best path for thermal conduction goes directly into the block instead of into the thermocouple. The grafoil may cause a small underestimate in ΔT. As the grafoil is only 100μ thick with a thermal conductivity of chem10 W/mK, its thermal resistance is a small fraction of sample thermal resistance (less than 2%). The effect on the measured ΔT is therefore negligible.

The consistency of thermal contacts may be tested by measuring the Seebeck both at ambient pressure and under vacuum. Ambient pressure mediates the contact between sample, heater blocks, and thermocouples, thereby reducing the sample thermal contact resistance. Dr. Martin at NIST tested this effect both with and without the use of grafoil to mediate the contact, see Figure 3.6. When no grafoil was present, reducing the pressure from atmosphere to rough vaccuum resulted in a 10% shift in the measured value of Seebeck. This 10% shift was eliminated by the inclusion of grafoil contact. The foil also acts as a diffusion barrier to protect the sample and the thermocouple from chemical reactions. Given the high diffusivity of Ag and Cu into other materials, this is an important concern for this work in particular.

3.2 Apparatus and Protocols

The Seebeck apparatus used in this experiment is diagrammed in Figures 3.7(a),3.7(a). This diagram was originally published in Iwanaga *et al.* [90]. A photograph of the actually apparatus is displayed in Figure 3.7(b). In describing it I will refer to the
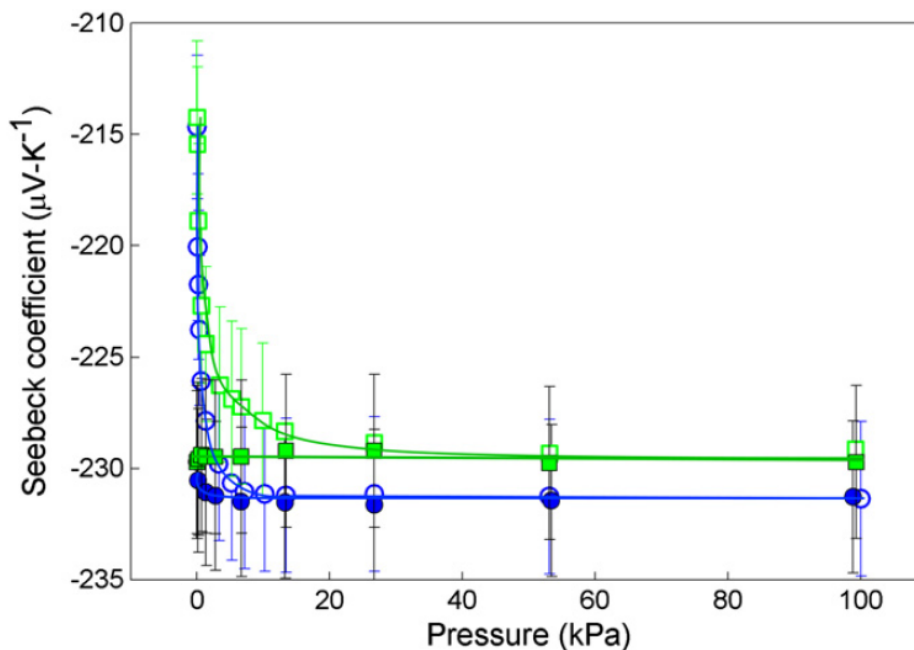
Figure 3.6: The effect of ambient pressure on measured Seebeck. Seebeck coefficient as a function of helium (circles) and nitrogen (squares) gas pressure at 295 K for Bi_2Te_3 SRM 3451 measured under a poor thermal contact (unfilled circles) and the Seebeck coefficient using a graphite-based foil interface (filled circles). Image from Martin *et al.* [131].
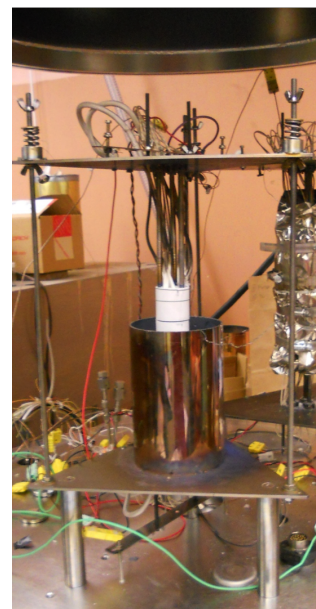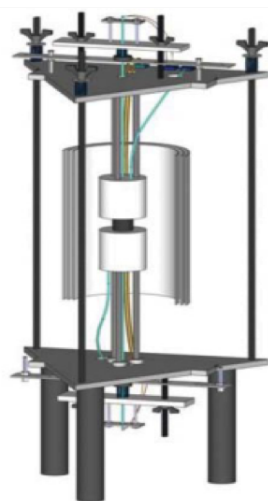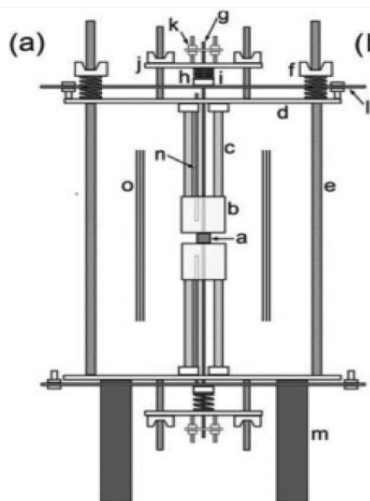
Figure 3.7: Diagram of Seebeck apparatus in profile (a) and three-quarter view (b). Photograph of apparatus used in this research (c). Figures part (a) and (b) were previously published in Iwanaga *et al.*[90]

labels within Figure 3.7(a). The sample (a) is compressed between two cylindrical Boron Nitride (Saint Gobain AX05) heater blocks (b) by three springs (f) pushing through a top plate (d) and three Inconel rod (c). The Boron Nitride blocks contain six symmetrically placed heater cartridges. The measurement thermocouples (g) run through the centers of the heater blocks in order to thermalize them and eliminate the cold finger effect. Compression of the thermocouple onto the sample for good contact is achieved by a spring (h) and plate (i) combination. The thermocouple apparatus is mechanically connected to the top plate by two threaded rods (j). The relative position of the thermocouple is adjusted by two wingnuts pushing on a small plate. The small plate is connected mechanically to the thermocouple by a spring (h). Adjustment by the wingnuts and spring are minor compared with constructing the thermocouple such that the length between the spring and the thermocouple tip is appropriate. An error of one quarter of an inch in this aspect of thermocouple construction will result in an insurmountable error. The thermocouple is put on and removed from the sample via holdoff bolts (l).

The loading procedure for the system is as follows. Wingnuts are located underneath the top plate and are used to separate the two boron nitride blocks without external mechanical support (*e.g.*, the user's arm). If the thermocouples are extended by releasing the hold-offs (l), they should extend 2-4 mm out of the block. The wingnuts for the thermocouples (j) should be set such that the thermocouple can be pushed back mechanically with a single finger with 3-5 pounds of force. If the thermocouple extends less than 2 mm out of the block than the thermal contact may be too poor, and it may even lose contact at higher temperatures due to the thermal expansion of the block. If the thermocouple extends too far it will require too great a force to contract it — Hooke's law being proportional to displacement. This will result in mechanical degradation of the thermocouple tip. The thermocouple tip should be cleaned with isopropanol using a tweezer and a folded Kimwipe in the same gentle fashion by which optical lenses are cleaned. Then the thermocouple holdoffs should be re-engaged.

The sample should then be sandwiched between two pieces of graphoil cut to

Vacuum Chamber

Solid State Relays

Temperature Controller

Heat Shield

$\overrightarrow{\sigma T_h^4 A}$ $\overrightarrow{\sigma T^4 A}$

$\overleftarrow{\sigma T^4 A}$ $\overleftarrow{\sigma T_c^4 A}$

Heaters

Visual Basic

K-Type Thermocouple

Nb-Chromel Thermocouple

Multimeter

Scanner
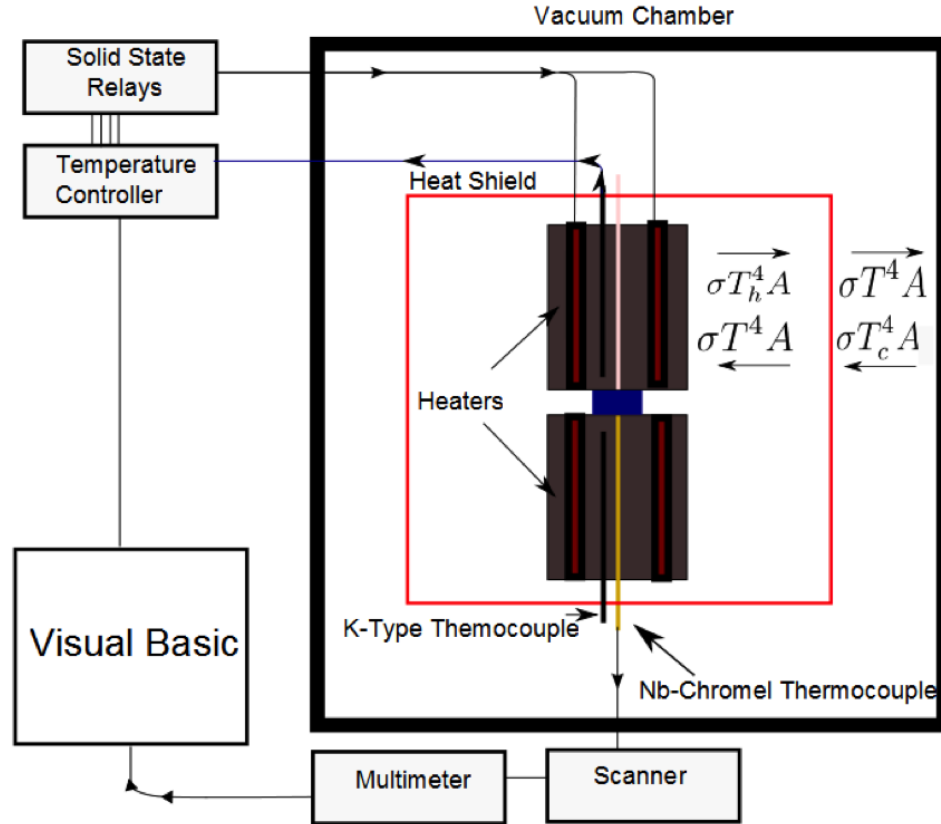
Figure 3.8: Schematic of the measurement and control software used.

the appropriate size and placed on the center of the bottom heater. The top heater should then be carefully lowered onto the top side of the sample. One hand should gently stabilize the top heater block while the other hand lowers the top plate (d) and adjusts the top wingnuts (f). Once the top heater block is on top of the sample the top plate wingnuts (f) should be tightened until resistance is felt. Then each should be tightened by one half a turn; this tightening should be done three times. This will ensure firm contact between the sample and the heater block. Then the thermocouple hold-offs should be disengaged. The heat shield (n) should then by tied onto the threaded rods (e) above the top plate. On occassion — for example, immediately after new thermocouples are installed — the Seebeck should be tested just above room temperature (40 to 50 °C) both in air and in vaccuum to ensure that the pressure is sufficient to overcome the thermal contact errors described above.

A schematic of the measurement and control instrumentation for the apparatus

is shown in Figure 3.8(a). The measurement and control electronics and sensors are kept completely separate. Custom thermocouples with a combination of Niobium and Chromel are used to measure the sample. The thermocouple wires exit to a thermocouple scanner card that includes an aluminum block with built-in resistive thermal device (RTD). To measure the temperature on each side of the sample, the voltage from that channel is read on a multimeter. That voltage and the temperature of the cold junction block are input into a look-up table by which the temperature at the thermocouple tip is obtained. The voltage is obtained via the Niobium wires. Niobium was chosen for its relatively low Seebeck coefficient as the Seebeck voltage must be compensated for during measurement.

A k-type thermocouple inserted separately in the block is used to measure and control its temperature. The k-type thermocouples output is connected directly to an Omega CN7000 temperature controller. This value and the temperature set-point allow for PID control of the heater catridges in the heater block. The heaters are resistive elements that are powered directly from the wall through solid state relays. The PID controllers alter the duty cycle time of the solid state relays and therefore the thermal power. All control is computer controlled through a Visual Basic program written by Dr. G. Jeffrey Snyder with some modifications by this author to deal with particular challenges. At present the author has begun the process of transitioning to python-based control software.

Above 300 °C the dissipation of heat in the system is driven by black body radiation. This was emprically determined via liner fitting of input power and the fourth power of temperature (Figure 3.9) with fitting coefficient R = 0.99459. The scatter in the data is due to the functioning of the PID control system. Blackbody radiation may cause thermal fluxes out of the side of the heater block and induce a temperature offset between the two thermocouples and lead to cold finger errors. For this reason heat shielding is installed in the apparatus. In later revisions radiation heat shielding was replaced with direct thermal insulation of the apparatus.
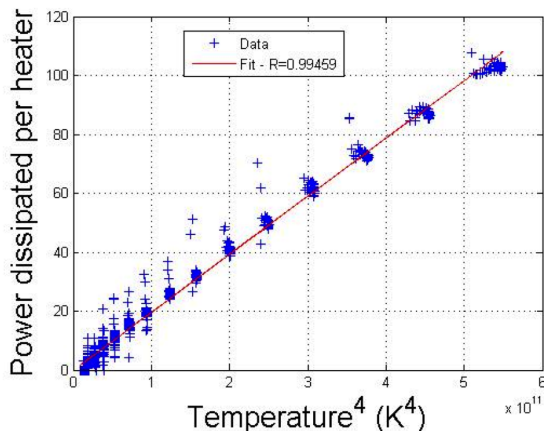
Figure 3.9: Black body radiation is the dominant thermal loss mechanism at high temperatures. When the apparatus is run at 1000 °C the radiant heat is sufficient to warm the metal bell jar to 50 °C.

3.3 Challenges of Phase Transition Seebeck

Though materials based on Ag_2Se and Cu_2Se are of great current interest in thermoelectrics, they are not new materials. Both are binary chalcogenides and are even present as uncommon earth minerals as Berzelianite (Cu_2Se) and Naumanite (Ag_2Se). Despite this rich history, my work is the first to successfully measure their phase transition thermoelectric properties correctly. I provide an example of literature attempts to measure their Seebeck coefficient in Figure 3.10. The plot is from Okamoto (1971) [144] and includes data from Bush and Junod (1959) [27]. These two data sets used different approaches and these different approaches led to different errors. My understanding of these two approaches and their errors indicated that a different technique was necessary. This method is described in detail in section 3.4 below.

Okamato's data superficially resembles my own, but his approach suffered from systemic problems. First, he used a two point Seebeck geometry with the heater blocks made of copper. This raises the possibility of transfer of copper in and out of Cu_2Se from the heater blocks; thereby making the exact stoichiometry uncertain. He also used a variation of the single point Seebeck method that I will call the *single ramp technique*. Each data point he measured was derived from a single ΔV,
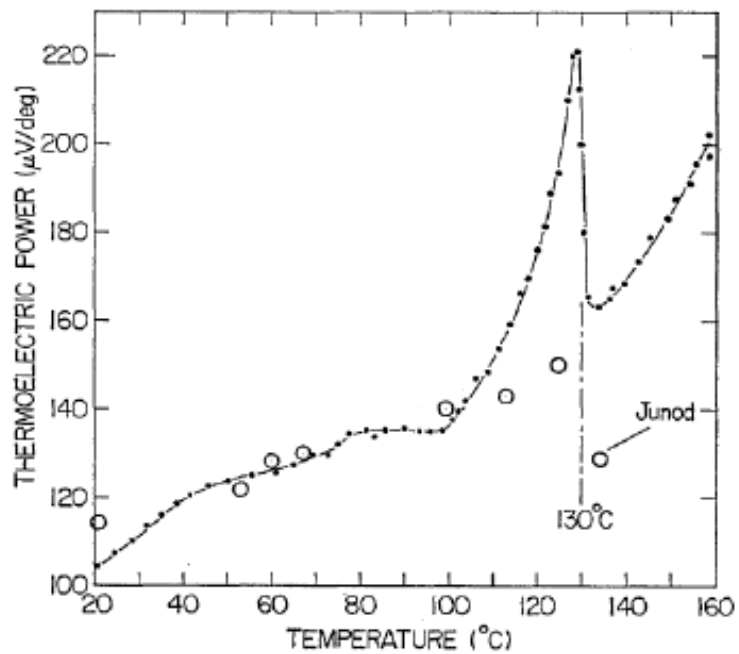
Figure 3.10: Literature Seebeck (Thermoelectric Power) data on Cu$_2$Se. Image extracted from Okamoto (1971) [144]. Data points labeled Junod originally from Bush & Junod [27]. Okamotos data was obtained using a single point technique. Bush & Junods data was obtained using an oscillation technique. Both were insufficient for correct determination of the Seebeck Coefficient.

ΔT pair. Therefore any offset temperature or voltage would skew the value as per Equation 3.1. The ΔT used was up to 5 K and that therefore limits the resolution at or near the phase transition. That limitation is sufficient for determining the *existence* of a phase-transition anomaly; it may be insufficient for the proper calculation of zT. Methodologically, he ramped the average temperature at a constant (but unreported) rate while performing single point Seebeck data. He observed the peak in Seebeck, but there is no way to determine whether the data is accurate or chimerical.

Bush and Junod used the oscillation method. Variants of this technique are in standard use at Caltech, JPL, and in commercially available instruments. Ideally in this technique, the sample is kept at an average temperature ($\bar{T}$), while the voltage (V) is measured at various temperature differences (ΔT). The Seebeck coefficient (α) is taken as the slope of the best fit line to V and ΔT data. This standard method is not ideal for the assessment of phase transition properties for three reasons: drift in temperature during a Seebeck oscillation, the instability due to kinetics associated with the phase transition, and limits on its temperature resolution. Bush and Junod caught hints of the phase transition anomaly using this technique, but without the resolution necessary to make a definitive statement.

The finite temperature shifts of an oscillation sequence causes errors when measuring near a phase transition. To make a Seebeck fit, the temperature of the two sides of the sample must deviate through a range of ΔT's. This range is typically 5 K or 6 K to ensure a good Seebeck fit. For a typical sample with a slowly varying Seebeck coefficient this range is insufficient to cause a significant error. However, near the peaked Seebeck second order transition of Cu_2Se or the step change in Seebeck at a first order transition, the finite temperature range used can be problematic.

The essence of a Seebeck fit is to make the approximation to a set of N $(V, \Delta T)$ points taken at the same $\bar{T}$.

$$\alpha \equiv \frac{\partial V}{\partial T} = \frac{1}{N} \sum_i \frac{\Delta V_i - V_{Dark}}{\Delta T_i}, \tag{3.2}$$

if N points are measured. The process is therefore to approximate to a Taylor expan-
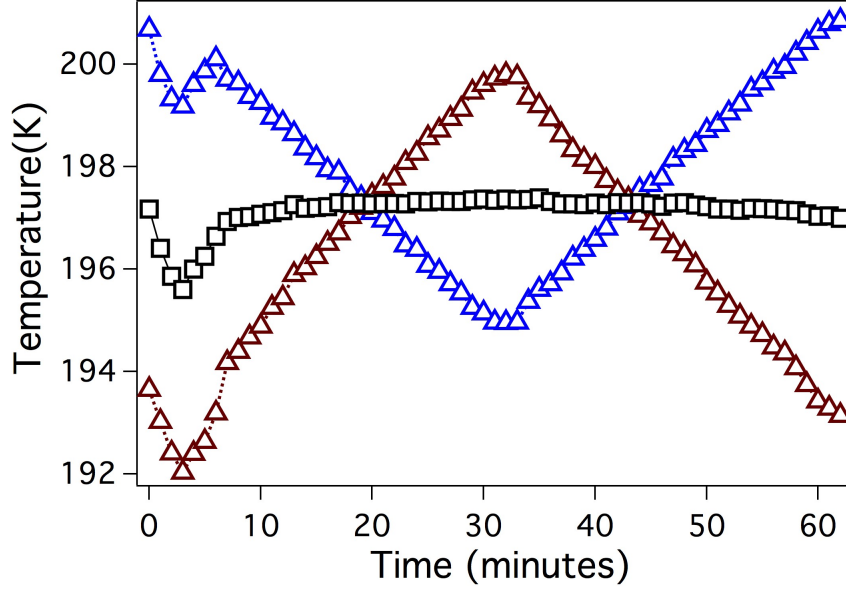
Figure 3.11: Sample oscillation sequence. Magenta and blue triangles are the temperature at the top and bottom side of the sample. Black squares are the average temperature. There is a small variation of average temperature that is correlated with the direction of ΔT.

sion to first order, and so intuitively as ΔT becomes larger this approximation error gets more and more significant. The full Taylor expansion for the Seebeck coefficient about $\bar{T}$ is:

$$\alpha(T) = \alpha(\bar{T}) + (T - \bar{T})\frac{\partial \alpha}{\partial T} + \frac{1}{2}(T - \bar{T})^2\frac{\partial^2 \alpha}{\partial T^2} + ... \tag{3.3}$$

Defining $\delta T = T - \bar{T}$, the corresponding voltage error at a given ΔT is:

$$V_{error}(\Delta T) = \alpha(T) - \alpha(\bar{T}) = \int_{-\Delta T/2}^{\Delta T/2} d\delta \left(\delta T \frac{\partial \alpha}{\partial T} + \frac{1}{2}\delta T^2 \frac{\partial^2 \alpha}{\partial T^2} \right) \tag{3.4}$$

Inspection of Equation 3.4 reveals that the odd terms of Equation. 3.3 do not contribute to V_{error}. However, if there is a correlation between the deviations in δT and ΔT, there will be an error term on order of $\frac{\partial \alpha}{\partial T} \langle \delta T^2 \rangle^{1/2}$ .Inspection of oscillation data from our apparatus reveals that $\langle \delta T^2 \rangle^{1/2}$ is of order 0.25 K. This problem is therefore significant near 406 K in Cu_2Se — the temperature of the zT peak — at which $\alpha = 140\,\mu V/K$ and $\frac{\partial \alpha}{\partial T} = 20\,\mu V/K^2$. It may result in a several percentage error.
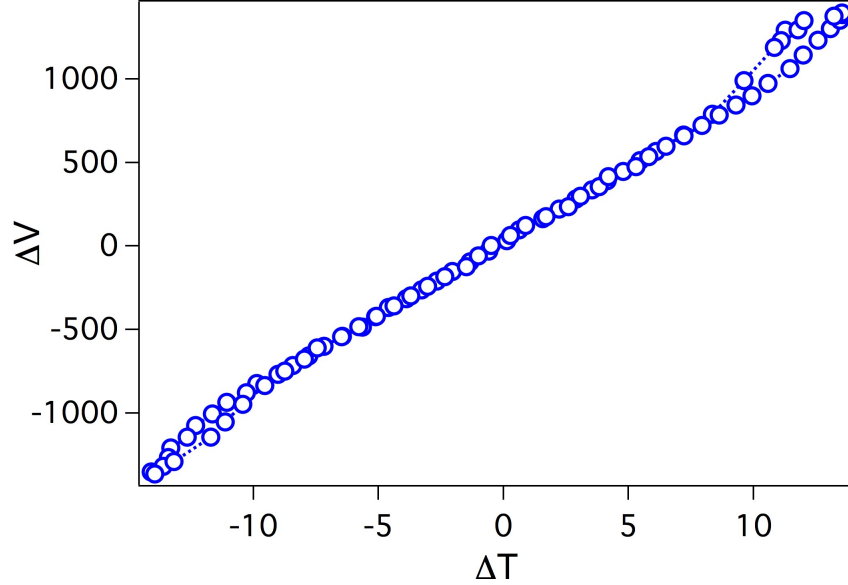
Figure 3.12: Raw Seebeck data for Cu_2Se measured at $\bar{T} = 410K$. There is a distinct cubic contribution and deviations from a consistent curve.

Ignoring correlations between ΔT and $\bar{T}$, we can simplify Equation 3.4 as:

$$V_{error} = \frac{\Delta T^3}{24} \frac{\partial^2 \alpha}{\partial T^2} \tag{3.5}$$

As Seebeck is typically cited with a 10% error, the condition for this effect being significant is:

$$\frac{\partial^2 \alpha}{\partial T^2} = 0.72 \alpha \Delta T^{-2} \tag{3.6}$$

While for a typical thermoelectric material this error is small, for phase transition materials it can be significant. For a typical thermoelectric material α varies gradually while temperature $\frac{\partial^2 \alpha}{\partial T^2}$ is very small $(< .01 \, \mu V/K^3)$. Even in the most extreme case with $\alpha = 100 \, \mu V/K$ and $\frac{\partial^2 \alpha}{\partial T^2} = 0.1 \, \mu V/K^3$, the condition of Equation refeq:Verror3 is met only for $\Delta T > 25K$. However, near the Seebeck peak of Cu_2Se $\frac{\partial^2 \alpha}{\partial T^2} \approx 3 \, \mu V/K^2$ and the relevant ΔT from Equation 3.6 is the only 5 K. This error can be seen in Figure 3.12.

In the case of a step change in Seebeck at a first order transition, the Taylor expansion formalism of Equation 3.3 must be modified to contain two piecewise functions

above and below the phase transition. These piecewise functions will be slowly vary-ing, thereby making further Taylor expansion unnecessary for the argument above. Raw Seebeck plots in which a portion of the ΔT are above and below the phase transition are difficult to analyze. For a typical oscillation through a phase transition the resulting data will be disjointed and non-linear.

During a typical Seebeck oscillation $\bar{T}$ deviates slightly from its average value, as can be seen in Figure 3.11. These deviations occur in the system described above due to imperfect PID control and the use of separate thermocouples for tempera-ture control and temperature measurement. The Seebeck error for a single point will be only of order $\frac{\partial \alpha}{\partial T}\Delta T$; in typical thermoelectric materials (*e.g.*, $\frac{\partial \alpha}{\partial T} = 1\,\mu\text{V/K}^2$, $\alpha = 100\,\mu\text{V/K}$, this error is only a few percent. The point by point error itself will only effect the overall Seebeck if there is a correlation between ΔT and $\bar{T}$. Otherwise these terms in Equation 3.2 will average to zero, and the leading term will be that of $\frac{\partial^2 \alpha}{\partial T^2}$. As argued above, this term is small for typical thermoelectrics.

For phase transition thermoelectrics the drift in $\bar{T}$ during an oscillation measure-ment can have large effects. Near the Seebeck peak of Cu$_2$Se $\frac{\partial \alpha}{\partial T}\Delta T$ is as much as 8% of α. The result of this error would be inaccuracies (reduction) in the peak value of Seebeck measured. For a first order transition such as Ag$_2$Se, crossing the phase transition temperature will result in errors greater than 10% in measured voltage.

3.4   The Multi-Ramp Seebeck Technique

To minimize error and increase the resolution of the Seebeck data near the phase transition, a modification to the standard Seebeck metrology was made. I named this technique the "Ramp Seebeck" technique. While in the Oscillation Seebeck technique $\bar{T}$ is held nominally constant while ΔT is varied and the resultant voltage measured, in the Ramp Seebeck technique ΔT is held nominally fixed while the $\bar{T}$ is steadily increased or decreased.

During each ramp the $(\Delta T, V)$ pairs are measured continuously. In our apparatus the effective $\bar{T}$ steps between data points was on average 0.25 K when ramping at 15
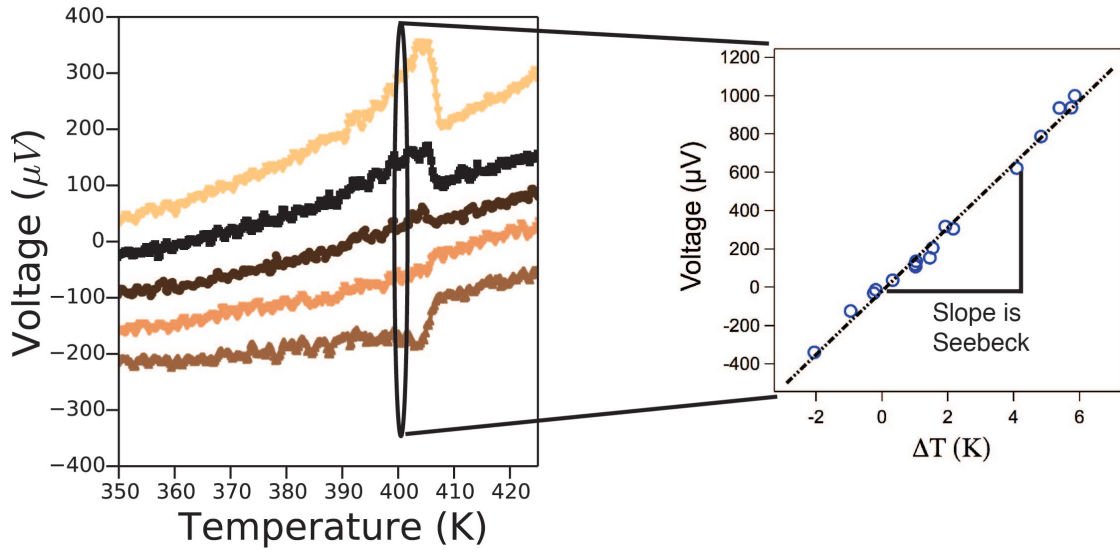
Figure 3.13: Data from multiple ramp sequences are combined point by point to create ΔV versus ΔT from which point by point Seebeck values may be extracted

K/min. Each separate ramp has a slightly different set of $\bar{T}$ values. The $(\bar{T}, \Delta T, V)$ data sets from each ramp were interpolated onto the same $\bar{T}$ values for comparison. The spacing of the new $\bar{T}$ was the average temperature step between data points, as that sets a resolution limit on the measurement procedure.

This process is illustrated in Figure 3.13, in which the coefficient is plotted point by point without compensation for the voltage offset. If data from a single $\bar{T}$ is explicitly plotted, than a raw Seebeck plot (V vs ΔT) is created from which a single $(\bar{T}, \alpha)$ point may be determined. This process is done at all temperatures using the combined heating and cooling data and is illustrated in Figure 3.13.

The proof of the superiority of the multi-ramp method for this problem is its superior results. In Figure 3.14 I plot the Seebeck coefficient and dark temperature measured on Cu_2Se by both the oscillation and ramp method. While the oscillation method shows the general trend of the anomalous Seebeck peak, it lacks sufficient resolution and clarity to fully describe the phase transition region. The temperature intercept is also of much smaller magnitude during the ramp measurement. The reason for this happy situation is unclear, but it is possible that the multiple ramps through the phase transition temperature allow the thermal contacts to stabilize into
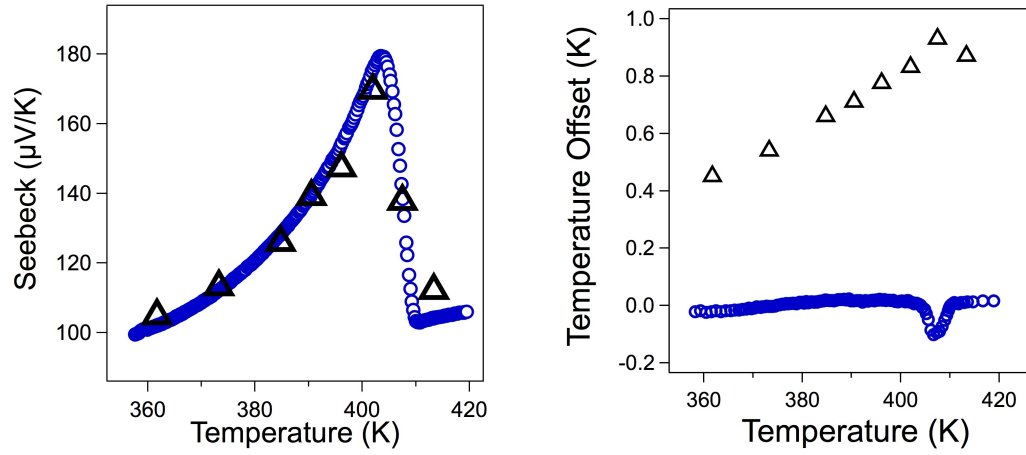
Figure 3.14: Comparison of oscillation (black triangles) and multi-ramp method data (blue circles) for Cu$_2$Se in proximity to its phase transition. The ramp data is superior.

a better position. Therefore the thermal contacts are superior and thus the Seebeck value more trustworthy for data using the multi-ramp technique rather than the oscillation technique.

Chapter 4

Operational Stability

A major question for the future development of ionic conducting thermoelectrics, particularly Cu_2Se and $Cu_{1.97}Ag_{0.03}Se$, is whether these materials will be stable under device conditions of sustained temperature gradients and currents. Both copper and silver show fast interdiffusion in many materials [52, 89]. Therefore there is strong concern about the decomposition of these materials when operated under the device condition of steady state current operation. Indeed, $Cu_{1.97}Ag_{0.03}Se$, Cu_2Se, and Cu_2Se are empirically known to be unstable under current density of $10\,A/cm^2$ at elevated temperatures in their super-ionic phase [24, 48]. However, while these issues may occur at elevated temperatures, my empirical testing shows no evidence of electrochemical degradation at the phase transition temperature.

In section 4.1 I will discuss the publication [24] I wrote summarizing the DOE/NASA studies of $Cu_{1.97}Ag_{0.03}Se$ in the 1970s. In this publication I also repeated and redemonstrated the electrochemical effects in Cu_2Se. In section 4.2 I show the work I did repeating this experiment in the low temperature phase. I will also discuss the possible reasons for the difference in degradation behavior between the high temperature and low temperature phase, with particular reference to the extensive studies on Cu_2Se performed by Mikhail Korzhuev of the Baikov Metallurgical Institute.

4.1 $Cu_{1.97}Ag_{0.03}Se$ at NASA

In the late 1960s the 3M corporation designed and patented a set of highly efficient selenide thermoelectric materials to be used for the next generation of radio-isotope thermal generators (RTGs) and for other DOE applications [72, 73, 74, 40].The n-type material developed was based on Gd_2Se_{3-x}. The p-type material was $Cu_{1.97}Ag_{.03}Se_{1+y}$, $y < 0.01$ [75]. This proprietary material was referred to as TPM-217. 3Ms reports indicated good thermoelectric properties that were stable over 4000 hours, though typically the material would take several hundred hours to become stable [72]. Further material studies were done by the General Atomics Corporation [58, 59, 57, 55, 56, 60] and NASA Jet Propulsion Laboratory [183, 182, 181]. Device and generator development was done by 3M and Teledyne Energy Systems [149].

The technical reports cited in this thesis are merely a representative sample of the dozens of quarterly and annual reports available from the DOE OSTI database and easily searched for with the key word "TPM-217." There is signifcant overlap between many of these reports; the set referenced above is representative of the program as a whole. General Atomics images of the material as synthesized by 3M showed clear Cu and Ag rich regions, which could be eliminated by further hot-pressing and annealing of the material [71]. The 3M reports also indicate that there was a small problem of Cu extrusion at the interface between the $Cu_{1.97}Ag_{0.03}Se_{1+y}$ and the cold side end-cap [72]. Though this issue was identified at the beginning of the program, it was not addressed until it began to cause systematic issues, such as increasing device contact resistances under extended operation [80]. The failure of the TPM-217 program was as much or more a failure of program management as it was of the materials' properties themselves.

Data from 3M indicates that $Cu_{1.97}Ag_{0.03}Se_{1+y}$ has a peak zT of 1.2 at 1000 K,[9] see Figure 4.1. 3M typically synthesized 0.1% excess selenium samples. Data from JPL indicated a peak zT of 0.8 at 800 K. JPL bonded their samples to copper at the cold end. Therefore the equilibrium Se excess in their samples varied from 0.02% to 0.08% depending on the temperature as the copper in the cold junction
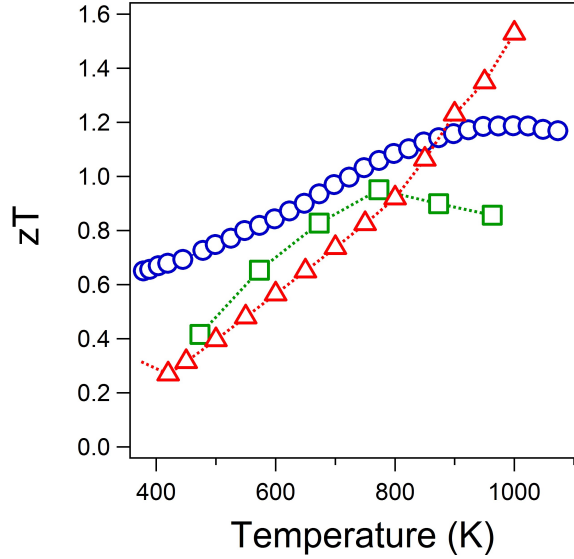
Figure 4.1: zT data for $Cu_{1.97}Ag_{0.03}Se$ (TPM-217) as extracted from JPL status reports. Blue circles are data from 3M Corporation tests. Green squares are data from JPL tests [71]. Red triangles represent data from Liu *et al.* [122].

block diffused in and out of the bulk sample.(See Figures 1 and 2 of reference [181]) Electrical conductivity and thermopower were measured via a four-point technique. Thermal conductivity was directly measured by steady-state direct calorimetry, as was typical then, [81] rather than by separate measurement of thermal diffusivity and heat capacity, as is done in modern thermoelectric laboratories. The material was also evaluated over a ten year period by the General Atomics corporation. Most of the information in the General Atomics reports evaluates $Cu_{1.97}Ag_{0.03}Se_{1+y}$ in a device setting, with particular focus on high-temperature (1000 K to 1200 K) stability and operation under typical device thermal gradients with a cold-side at 400 K to 600 K and a hot side at 1000 K to 1200 K, as well as under conditions of applied current and in segmented legs and devices. These tests revealed problems that were not reported in $Cu_{1.97}Ag_{0.03}Se_{1+y}$ original material testing at 3M.

The biggest problem observed was material loss rate, see Figure 4.1. At 1200 K the loss rate under zero current was found to be $10^{-4}\,g\cdot cm^{-2}\cdot hr^{-1}$, and under conditions of applied current the loss rate was measured as high as $10^{-2}\,g\cdot cm^{-2}hr^{-1}$ at iL/A = 8.6 A/cm [40]. For a reasonable sample geometry, these loss rates would
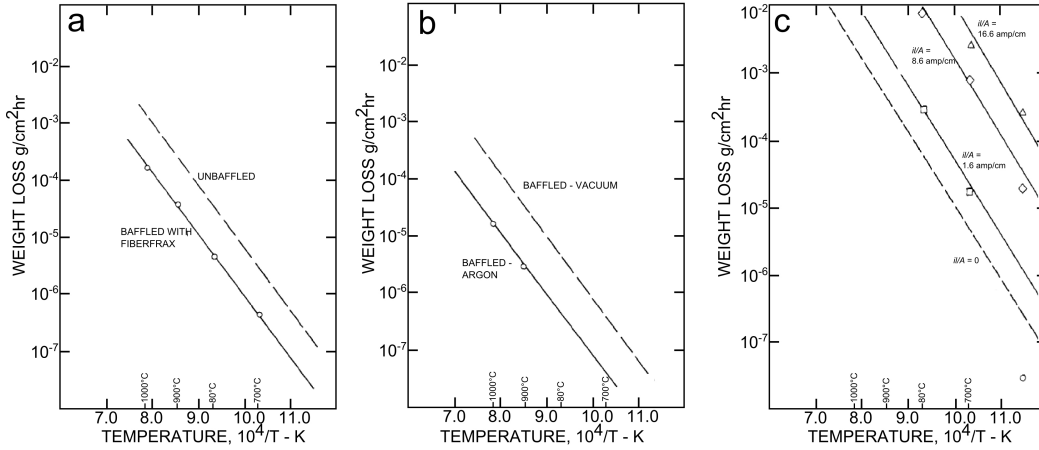
Figure 4.2: Weight loss rates for TPM-217 as a function of temperature. Figures 6, 7, and 8 from reference [183]. (a) Comparison between unprotected and baffled TPM-217. (b) Comparison between TPM-217 in vacuum and in 750 mbar argon atmosphere. (c) Loss rates at different applied currents. Il/A ranges from 0 A/cm to 16.6 A/cm.

cause rapid deterioration of the material. Quantitatively the fraction loss rate per hour is a function of the loss rate (LR), the geometric density (ρ) and the leg radius (r) as:

$$fLR = \frac{2LR}{\rho r} \tag{4.1}$$

This gives for a 1 cm radius leg a loss of mass equal to 0.3% of total mass per hour under applied current. The mechanism for this loss was believed to be evaporation of Se at the hot end.[9] As thermal and electrical potential gradients created a Cu concentration gradient with a low concentration of copper at the hot end, the Se activity increased and thereby increased its vapor pressure. The evaporation of the selenium causes the solid state precipitation of the copper there. Under conditions of applied thermal and electrical gradient, it was found that the percent excess selenium in the material varied with temperature. 3M and JPL found that excess selenium percent increased by the factor of 0.0095 iL/A over the zero-current concentration with iL/A in Acm. To mitigate this problem the p-leg was partitioned with a diffusion barrier. This diminished the problem of Se evaporation but also decreased zT by 25% [181].
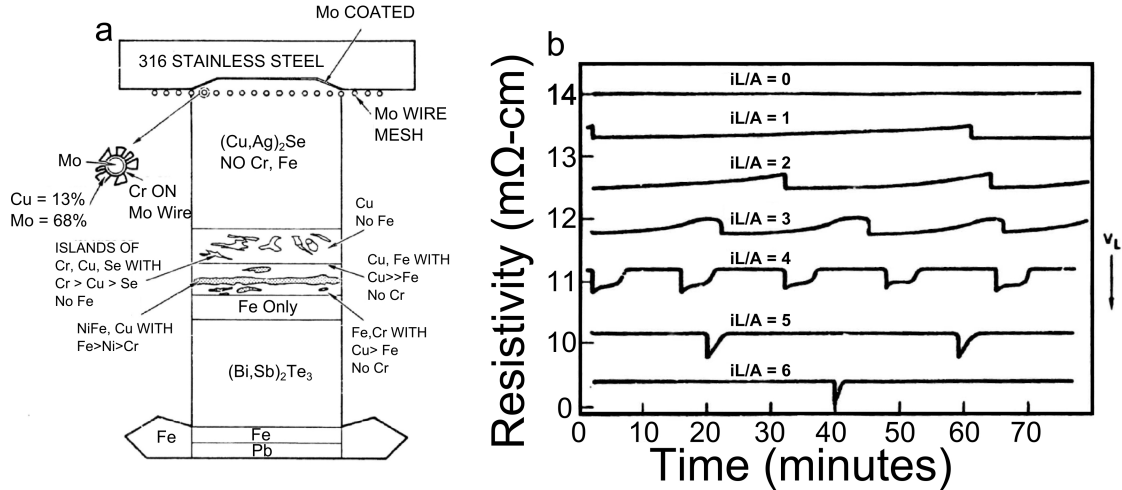
Figure 4.3: Degradation of segmented modules. Data from General Atomics final report [57], representing Figure 2-21 and Figure 2-31. (a) Depiction of chemical degradation after isothermal test of p-type leg after 2490 hr at a 1027 K/380 K thermal gradient. (b) Depiction of resistivity ratcheting under conditions of applied current. iL=A is in units of A/cm. $T_h = 1023\,\mathrm{K}$, $T_c = 473\,\mathrm{K}$.

To address this issue, General Atomics developed systems to suppress the evaporation of Se. They would baffle the $Cu_{1.97}Ag_{0.03}Se_{1+y}$ with boron nitride and boron oxide glassy coatings [79]. With greater baffling thickness they would find a reduction in material loss rate of up to two orders of magnitude, but this baffling decreases device efficiency by acting as a thermal short. This provides a limiting condition on the thickness of the baffling that can be effectively added to the module. They further found that they could suppress the weight loss rate by one order of magnitude if they operated in a low (2.5 torr) atmosphere of Argon instead of in vacuum [79]. The combination of these effects reduced the loss rate to a level that allows potential operation of the leg for multiple years without significant degradation. Another option for reducing the effect might be to decrease the hot end temperature, as evaporative material loss was is an exponential function of that temperature.(Figure 4.1)

The second major problem was the chemical degradation of the material and device, particularly under conditions of applied current. In the original 3M studies, these effects were obscured by the use of Cu as both hot and cold-side contacts. General Atomics found that at elevated temperature the Cu in $Cu_{1.97}Ag_{.03}Se_{1+y}$

would react with the Fe in 316 stainless steel contacts [79]. Tungsten, molybdenum, and tungsten-rhenium were found to be chemically unreactive to $Cu_{1.97}Ag_{0.03}Se_{1+y}$. However, these materials showed a coefficient of thermal expansion one-fifth that of $Cu_{1.97}Ag_{0.03}Se_{1+y}$, resulting in micro-cracks through which Cu could diffuse at elevated temperatures [79]. It is also possible that these cracks were related to the approximately 1.4% volume expansion at the 410K phase transition of the material [191]. In the final General Atomic tests during the late 1970s, $Cu_{1.97}Ag_{0.03}Se_{1+y}$ was used as the low temperature segment. Fe was used as the diffusion barrier for the segmented tests, because it was known to be compatible with $(Bi, Sb)_2Te_3$ [80] During isothermal tests it was found that the Fe reacted with the Cu in $Cu_{1.97}Ag_{0.03}Se_{1+y}$, see Figure 4.1a. A region of mixed Cu and Fe was found in between the $Cu_{1.97}Ag_{0.03}Se_{1+y}$ and the Fe, as well as a region of $Cu_{1.97}Ag_{0.03}Se_{1+y}$ with inclusions of Cu, Fe, and Cr from the coating of the 316 Stainless Steel end caps. Under conditions of applied current these segments failed dramatically. At different factors or IL/A ranging from 0 to 6 A/cm the segments were measured to have a resistivity ranging from 15 to 9 $m\Omega \cdot cm$ when $T_h = 1023\,K$ and $T_c = 473\,K$. The measured Seebeck coefficient and electrical resistivity would also show ratcheting behavior: at regular intervals the transport quantity would suddenly increase for a short period of time and then decrease down to the baselin, see Figure 4.1b. The ratcheting frequency depended on applied current, but was typically on order one ratchet per 15 minutes. These results were interpreted as being due to an irregular electrochemical process — plate out of copper followed by reabsorption of copper. Work done at 3M indicated that under accelerated conditions (Il/A = 15 A/cm), contact resistance increased to up to 700% of leg resistance after 100 hours. Upon thermal cycling, the device was restored to its original contact resistance. After these tests, the TPM-217 project was terminated [80].
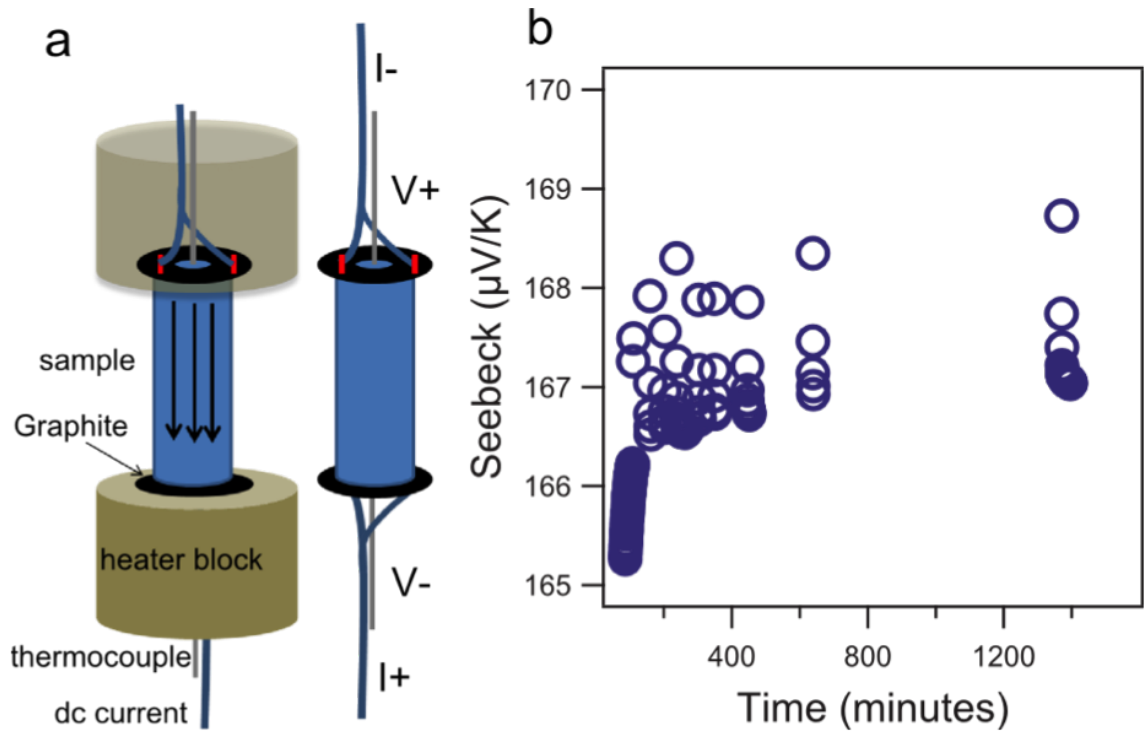
Figure 4.4: (a) Thermopower measurement apparatus with modification to allow operation with applied current. Conductive graphite contacts are used for the current source and sink. (b) Seebeck coefficient stability during measurement of sample under conditions of applied current and temperature gradient. It is unclear whether the transients represent instrument error or relaxation of the concentration gradient produced by turning off the current source immediately before the measurement.
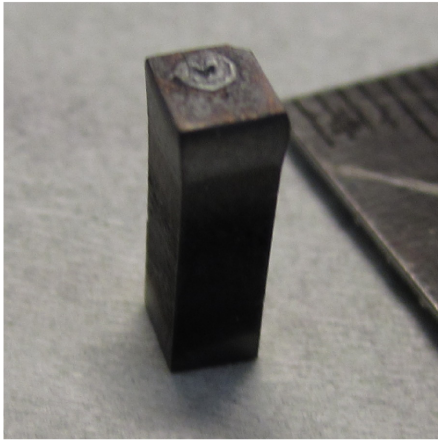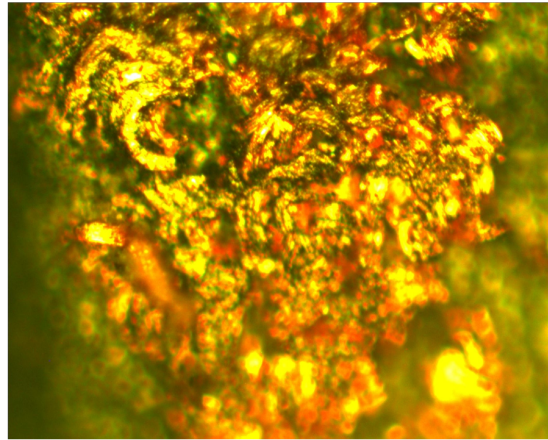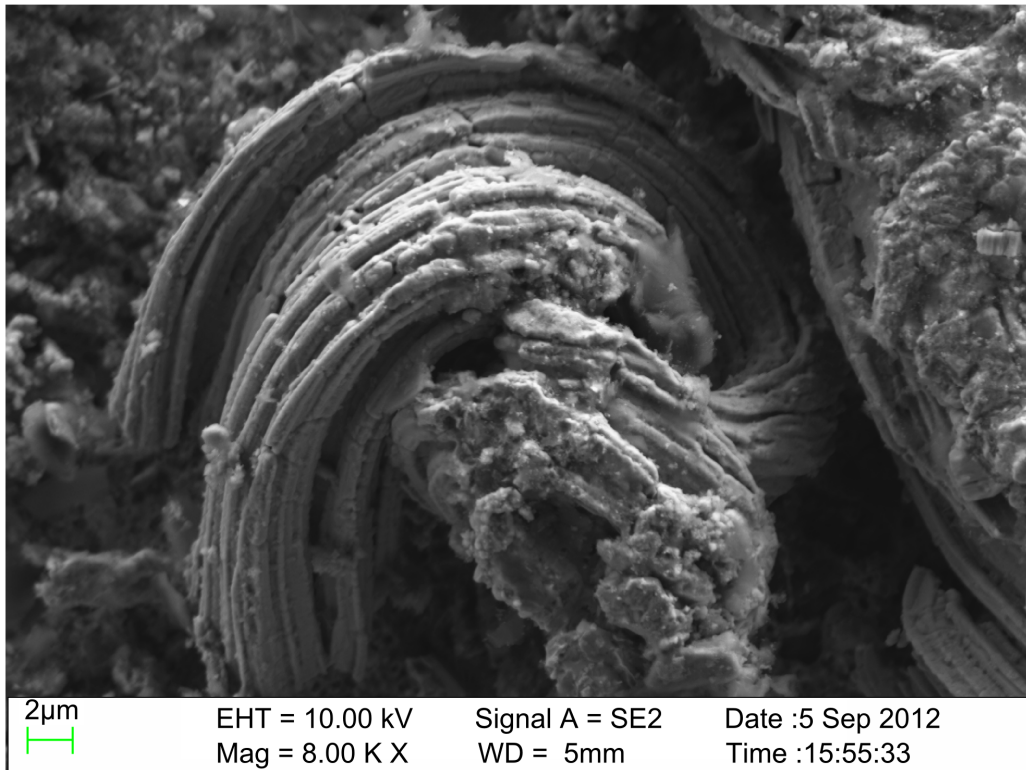
Figure 4.5: (a) Sample after applying current for 24 h. (b) Optical microscopy image of the current-sink face of the sample after applying a current for 24 h. Copper can be clearly seen precipitated on the surface. (c) SEM micrograph of top surface of sample after applying current for 24 h. The electromigrated copper grows into nanowire bundles (whiskers).

4.2 Degradation Testing of Cu_2Se

In order to understand these results and test their applicability to stoichiometric Cu2Se, we performed a short electro-migration experiment. A piece of copper selenide with cross-sectional area of 11.47 mm^2 and length of 10.7 mm was placed in a modified Seebeck apparatus, see Figure 4.2a. This Seebeck apparatus allows for simultaneous measurement of voltage and temperature and application of a current of up to 10 A. The sample was placed under a thermal gradient of 275 K for 16 hours with $T_h = 795\,K$ and $T_c = 520\,K$. The sample was not visibly affected. Current was varied from 0 to 10 A under the same thermal gradient as before. The resistivity did not depend upon applied current, in contradiction to the General Atomics reports [57]. The sample was then run under the same temperature gradient and in current continuously for 24 hours. The magnitude of this current was such that the voltage it induced was half the thermoelectric voltage. The direction was such that it transported Cu^+ in the opposite direction of thermal diffusion; Cu^+ should electromigrate to the hot-side and thermally diffuse to the cold side. The applied current was 1A. The applied current density was $j = 9\,A/cm^2$. There was no noticeable degradation of the average Seebeck coefficient over this period (Figure 4.2,b), which is consistent with the reports by JPL, 3M and General Atomics. When the sample was removed, visual inspection showed that it had undergone deformation at the hot end. Copper residue was visible on the face that had been against the hot-side heater and the current sink. The copper residue was inspected via optical microscope (Figure 4.2ab) and SEM (Figure 4.2c). The non-uniformity of the surface copper may have been due to spatial inhomogeneity in the contact resistivity between the current electrodes and the sample face. The SEM image reveals that the copper grows as bundles of nanowires. The result is a clear indication that electromigration drives physical degradation of Cu_2Se.

It has yet to be shown that liquid-like thermoelectrics based on fast-ion conductors can be used effectively in thermoelectric devices. The historical work by General Atomics, the 3M Corporation, Teledyne Energy Systems, and the NASA Jet Propul-

$\bar{T}$	ΔT	$J(A/cm^2)$	Duration (hr)	Plate out?
$658K$	$275K$	9	16	Yes
$404K$	$23K$	21.7	260	No
$387K$	$19K$	29.3	70	No
$423K$	$6K$	29.3	110	See Text

Table 4.1: Electromigration Experiments on Cu_2Se. No electomigration was observed below the phase transition temperature. When tested slightly above the phase transition temperature there was no plate out observed but there was copper observed on the side of the sample near the hot end.

sion Laboratory gives reason to be cautious in assuming that the excellent material properties observed in Cu_2Se will necessarily lead to a high quality thermoelectric module. There were three major problems observed. The first was electrochemical process resulting in weight loss via selenium evaporation. The 3M and General Atomics reports indicate that this problem was solved via baffling of the thermoelectric leg and operation in an Argon atmosphere. JPL and Teledyne expressed skepticism that the problem had been sufficiently reduced to prevent mechanical and chemical degradation of the thermoelectric generator. The second major problem was that of chemical reactivity at high temperature. In the view of all four major organizations involved in this work, this problem was never solved. Changes in contact resistance over time due to chemical process at interfaces between $(Ag, Cu)_2Se$ and diffusion barriers and bond pads led to unacceptable degradation of overall module performance. This last problem appears to be the principle reason the program was cancelled in 1979. If Cu_2Se is to be used for thermoelectric generators, these problems must be solved or evaded. Possible solutions would be the development and use of different diffusion barriers and contact materials, and the operation of the material only at lower temperature. The authors own work shows that physical degradation of Cu_2Se can be induced with currents similar to those needed to build a practical thermoelectric generator.

Fortunately these problems are eliminated below the phase transition temperature. The author performed high current density plate-out tests at three additional temperaturesm, the results of which are summarized in table 4.1. Currents and dura-

tions far in excess of that applied above the phase transition resulted in no observed copper plate out or altering of the transport properties. A further test was performed just above the phase transition temperature. It also showed no whisker-growth or plate out at the end of the sample, however there was a small quantity of Cu on the side of the sample near the hot end. This may result from loss of selenium due to evaporation or the piezodiffusion of Cu_2Se that has been noted by prior authors [107].

Why should copper excrescence growth occur and why should it only in the high temperature phase? Korzhuev provides a compelling answer [106, 103] that relies on the comparative thermodynamics of the solid, super-ionic, and melt phases. The sub-lattice melting and super-ionic transition causes a decrease in the melt entropy of transition of the super-ionic phase. He prepared two samples of nominal composition $Cu_{1.77}Se$ and Cu_2Se [106]. Denote the entropy of transition of the super-ionic transition as (ΔS_C) and that of the melt transition as (ΔS_m) and their sum $(\Delta S_T = \Delta S_C + \Delta S_M)$. ΔS_T differed by less than 2% between the two samples. In the Cu_2Se 62% of the total was released at the superionic transition, while in $Cu_{1.77}Se$ only 29% was released. This resulted in a significant change in melt morphology between the two samples. Korzhuev also suggested [103] that the entropy of the Cu in the superionic phase might be larger than that in the liquid phase. Therefore the material under external force (e.g. piezodiffusion, electrodiffusion) may be extremely unstable and tend to copper excrescence growth.

In general the super-ionic phase, in addition of course to its elevated ionic conductivity, is thermophysically quite distinct from the low temperature phase. It shows ultrafast chemical diffusion [107, 102, 108] and superplasticity [177]. In this context it is unsurprising that the ion-ordered phases do not show the same thermophysical instability as the super-ionic phase.

Chapter 5

Structural and Phase Transition Classification

Knowing the order of the structural phase transitions of Ag_2Se, Cu_2Se, and $Cu_{1.97}Ag_{0.03}Se$ is essential to understanding their thermoelectric properties in the vicinity of those phase transitions. Structure effects the transport properties through the mechanism of the electronic band structure and the phononic band structure. A change in band structure should always be accompanied by some, though perhaps subtle, change in structure. In later chapters I will present the transport properties of Ag_2Se, Cu_2Se, and $Cu_{1.97}Ag_{0.03}Se$, and there will be direct correlations between the structural changes of their phase transitions in their transport property. Understanding the nature of that transformation will allow me to develop the phenomenology necessary to explain them.

In the case of Cu_2Se there is an important scientific question that was answered by the work presented here. All previous authors considered Cu_2Se to be a first order phase transition [21, 41, 188, 191, 123, 121]. The work presented here shows it to be definitively second order [23]. This question of is central importance; the zT of Cu_2Se can not be properly calculated without understanding the nature of its phase transition. The determination of the Differential Scanning Calorimetry (DSC) data depends on the order of the phase transition. A substantial broad peak is seen in the DSC for Cu_2Se, see Figure 5.1. If the transition is second order the DSC measurement must be treated as c_p. If it were first order, it would be more proper to
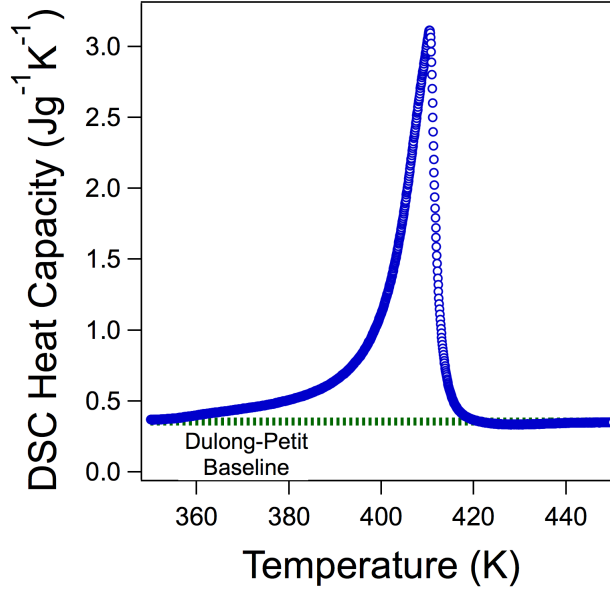
Figure 5.1: Differential Scanning Calorimetry c_p for Cu_2Se (blue circles) with the Dulong-Petit contribution as a green dotted line. Determining the order of the phase transition of Cu_2Se determines which of these two curves should be used to calculate c_p.

use the Dulong-Petit heat capacity instead.

As κ is calculated from c_p by the formula $\kappa = \rho c_p D_t$, and zT from κ by $zT = \alpha^2 \sigma T / \kappa$, this argument has an order of magnitude impact on the zT calculated. Treating Cu_2Se as a first order transition results in a five-fold overestimate in zT above its true value. Answering this question is particularly pressing due to recent published articles, [121, 123], claiming zTs two to five times that published here based on a first order treatment of c_p data.

Ag_2Se has a much simpler story. Prior literature shows understanding of its transformation as first order [15, 137, 21]. The work presented below agrees with that assessment. Still, it serves an excellent contrast to Cu_2Se and therefore illuminates the contrast between first and second order behavior in structural measurements.

$Cu_{1.97}Ag_{0.03}Se$ has the most complex story and one that this thesis does not fully resolve. As temperature is increased from room temperature it follows a trend similar to than of its Cu_2Se main phase. However, this trend is interrupted by the dissolution of a secondary phase of CuAgSe, eventually leading to a first order phase transition

at a temperature lower than Cu_2Se's second order phase transition.

In the next section I will discuss the definitions, different categorizations of, and phenomenology of structural phase transitions. There will be particular emphasis on order-disorder phase transitions. In section 5.2 I will discuss the measurements made on Ag_2Se, in section 5.3 I will discuss the characterization made of Cu_2Se, and in section 5.4 I will discuss measurements made on $Cu_{1.97}Ag_{0.03}Se$.

From understanding of the structure of a material, great insight can be obtained into its chemical performance can be obtained. For example, if the structure is well-understood, calculations of the electron and phonon band structure can be accomplished by Density Functional Theory (DFT). Super-ionic materials are a particularly challenging and interesting topic for structural studies. The high mobility and interstitial occupation probabilites of their ions means that determining the average location of the ions is insufficient for understanding their transport. For this work I am of course interested primarily in the nature of the superionic phase transition of Cu_2Se, Ag_2Se, and related materials.

5.1   Phase Transitions

A phase transition is a transformation in the symmetry of a system. The symmetries are understood in terms of the mean location or state of the degree of the system (*e.g.*, atoms, molecules, spin states). For example, the Arrhenius activation of Frenkel ion defects does not affect the mean symmetries and so is not a phase transition. Phase transitions are a very broad category. In a glass transition the symmetry reduction is purely local [162]. In crystal twinning or martensite transitions the reduction in order is between large ordered grains rather than due to a local effect [162]. In order-disorder transitions a local change in coordination results in a long-range transformation in symmetry [95]. An excellent summary of phase transitions in the solid state is available in Rao and Rao [162]. Super-ionic phase transitions are *order-disorder* phase transitions [21, 151].

The disordering is frequently modeled as due to the creation of Frenkel defects [163,
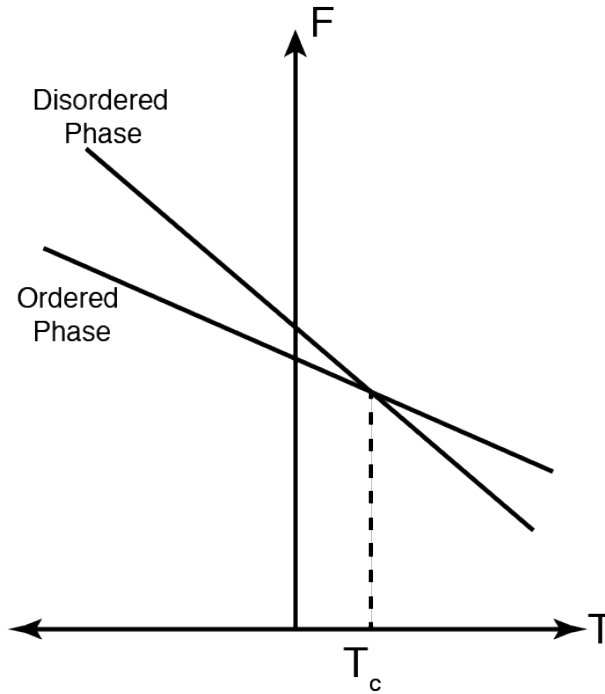
Figure 5.2: Free energy versus temperature for a first order phase transition. At T_c the free energy of both phases is equal.

22, 70, 34] in the high temperature phase; while this may be true for other super-ionics, the pair distribution function (PDF) data measured for my publication on Cu_2Se [23] contradicts this explanation. Super-ionics typically have an ionicity close to the critical value of 0.785 [22] described by Phillips [156]. Therefore there is almost equal preference for coordination into sites preferred by ionic coordination as those preferred by electronic coordination. Aniya [4, 5] suggested that it is the fluctuations between these two co-ordinations that are characteristic of superionic materials; this explanation is more compatible with our PDF data.

In an order-disorder phase transition all high-temperature symmetries are preserved in the low temperature phase. Solidification of a liquid, in which the rotational freedom of the liquid is lost but the chemical coordination maintained, is a very common instance of an order-disorder transition [31]. In an order-disorder transition the ordering is typically long range, mathematically defined as a very slow decay of correlations between states of the ordering element with increasing distance. The kinetics of an order-disorder transition are relatively fast, as they are not limited by atomic
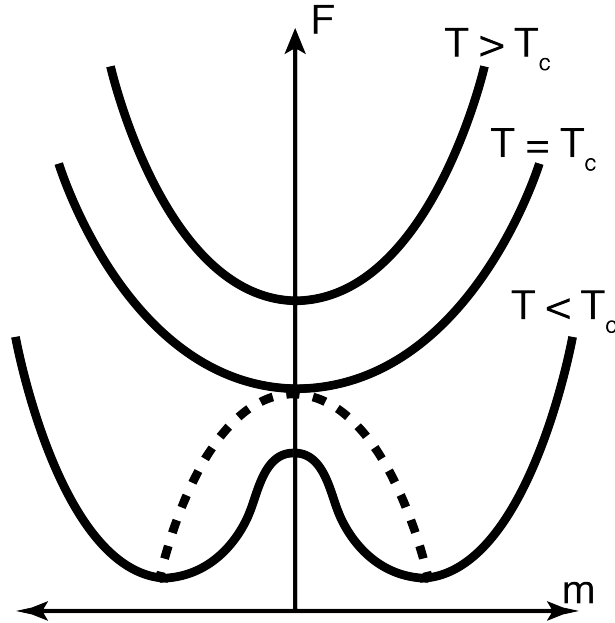
Figure 5.3: Free energy (F) versus order parameter (m) for a second order transition. Each of the curves is on its separate axis. The dotted line represents the equilibrium order parameter. As T goes to T_c, m goes continuously to zero.

diffusion.

5.1.1 Order-Disorder Phase Transitions Type

There are two principle types of order-disorder phase transitions. First order transitions are characterized by a first derivative discontinuity in a thermodynamic state parameter. This is typically measured by the instantaneous change in the volume or enthalpy as a thermodynamic parameter is changed [162]. A second order transition shows a discontinuity in a second or higher order derivative of the thermodynamic quantities. Certain second order transitions, including that of Cu_2Se, have a derivative of free energy that diverges to infinity at the phase transition temperature. Under the old classification system of Ehrenfest these were not considered second order transitions [53]. Instead they were called λ-transitions for the characteristic λ-shape in the dependence of their heat capacity on temperature [65, 157]. In more modern classification systems based on the work of Landau and Ginzburg, all phase transitions with continuous transformation of free energy are considered to be second order or

continuous [95].

Thermodynamic stability must be determined by a formulation that includes it. This formulation is the Free Energy. Without loss of generality, I use the Helmholtz Free (F) energy rather than Gibbs Free Energy. The difference between these two formulations is whether the system is held at constant volume (Helmholtz) or constant pressure (Gibbs); that detail is irrelevant to the argument below. For any given phase, defined as a set of symmetries obeyed by its degrees of freedom, the free energy is:

$$F_i = U_i - TS_i \tag{5.1}$$

There are as many phases as one can dream up. Very few are thermodynamically favorable. At a given set of thermodynamic conditions (*e.g.*, P,T) there will be only one phase or set of phases stable at a temperature. This phase or combination of phases is that which has minimal F_i. Each of these different phases will have a different U_i and S_i. A phase with higher entropy and high internal energy (*i.e.*, a gas) will be more stable at high temperatures than phase with low internal energy and low entropy (*i.e.*, a liquid); the converse is also true. If U_i and S_i are known for both phases the temperature of transition me determined by setting Equation 5.1 equal for each phase. Defining $\Delta U = U_i - U_j$ and $\Delta S = S_i - S_j$, this is equivalent to:

$$\Delta U = T\Delta S \tag{5.2}$$

As a very simple example consider the dissociation of diatomic oxygen into monatomic oxygen. In this hypothetical example $\Delta S = R/2$ where R is the gas constant while $\Delta U = 495 kJ/mol$. Therefore the temperature of the phase transition is $\approx$60,000 K — and indeed monatomic oxygen is very rarely observed.

In the case of the super-ionic transition ΔU is the energy that prefers the ions to be ordered in some way — perhaps a bond energy or the effect of alignment of a dipole with the crystal field — while ΔS is the additional configurational entropy available to the disordered phase. This may not be straightforward to calculate, as a substantial portion of the lifetime of super-ionics is spent between lattice sites in

regions of non-minimal potential [87]. Still, a simple configurational entropy argument helps to contextualize the scale of the phase transition. Following Korzhuev [103], if we assume that there are n_0 accessible vacancies per mobile ion in the super-ionic state then ΔS should be:

$$\Delta S = R\ln(n_0) \tag{5.3}$$

For $n_0 = 3$, $\Delta S = 9.1 \, \mathrm{J \cdot mol^{-1} K^{-1}}$. This is comparable to the entropy of melting.

If ΔS and ΔU are themselves independent of temperature, than there will be a first order phase transition. The difference in the free energy between the two states decreases until the high entropy state becomes more favorable at $T = T_c$. (Figure 5.2). Because the high entropy phase requires input of heat equal to $T\Delta S$ in order to form, there is frequently hysteresis in measurments through first order phase transitions. On heating the temperature rises above T_c, but the material remains ordered until sufficient heat has been absorbed to complete the phase transition. On cooling at a steady rate, a similar but opposite effect occurs. Measurements on heating overestimate the phase transition temperature while measurements on cooling underestimate it.

The assumption that ΔU and ΔS are constant as a function of temperature is generally invalid. Disordering can occur without a phase transition at all. For a phase transition to occur there must be a fundamental change in the symmetry of a system. For example, Arrhenius activation of defects will increase the internal energy and entropy slightly. This will increase T_c slightly and decrease the enthalpy of formation of the transition, but it will not eliminate it. That entropy increase is still much smaller than the entropy increase of the disordering phase transition. It will change the slopes and perhaps add curvature to the lines in Figure 5.2, but the lines will still intercept at an angle. That angle represents the entropy of the transition.

In order for the transition to be continuous rather than abrupt the two curves in Figure 5.2 must intercept tangent to one another, as thermodynamics requires the free energy by analytic for any given phase [31]. Therefore a continuous transition requires that the entropy of the ordered phase increases continuously and that its

internal energy increases continuously to the phase transition temperature. This requires the disordering process to be continuous rather than abrupt.

In proximity to an order-disorder phase transition the free energy is described in terms of an order parameter. For example, in the canonical case of a spin-ordering transition the order parameter is the average spin magnetization. The super-ionic order parameter is theorized to relate to the relative population of different sites by the mobile ion [151, 70]. The free energy contribution associated with the ordering — which is the only free energy terms that differentiates the ordered and disordered phase — is for a first order transition:

$$F = am^2 + bm^4 + cm^3 \tag{5.4}$$

The cubic term leads to a discontinuity in the value of m at $T = T_c$.

For a second order transition the Landau Free Energy is:

$$F = am^2 + bm^4 \tag{5.5}$$

As the phase transition is approached thermodynamic quantities follow critical power laws. For example, the order parameter decreases to zero continuously:

$$m = m_0 \left(\frac{T_c - T}{T_c} \right)^{\beta} \tag{5.6}$$

In which β is called the critical exponent. Order parameter in a structural transformation is related to the diffractogram peaks, so a related power law should be discoverable by analyzing those peaks. A similar power law is expected for heat capacity.

Another type of phase transition is a co-existence phase transformation. This is a temperature extended first order phase transtion. some interaction (*i.e.*, pressure) between the concentration of the two phases elongates the region over which the low-temperature phase transforms into the high temperature phase. This sort of phase is easily distinguished from a true second order transition by diffractogram. In a

coexistence transition the intensities will vary as one phase steadily appears and the other steadily disappears, but the angles at which they have diffraction peaks will remain steady.

A final type of phase transition is a *weakly first-order* phase transition [16]. In this type the symmetry between the multiple minima in free energy is weakly broken so that the two minima in Figure 5.3 are slightly displaced from one another. At temperatures well below the phase transition temperature the symmetry breaking appears very similar to a second order transition, except that one minima is global and so slightly preferred. At temperature near the phase transition this tiny offset is large compared to the difference between the ordered state's minimum and the disordered states minimum, and a first-order aspect of the transition appears. Whenever a lambda type second order transition is heated or cooled through its phase transition at a finite rate, it is to some degree weakly first order. The heat capacity at T_c is infinite and so for even a very slow heating rate and very good connection of the sample to a thermal bath, there will be a moment at which the correct heat cannot be supplied.

5.2 Ag_2Se

The high temperature structure and phase transition of Ag_2Se were first noted by Rahlfs in 1934 [161]. In the high temperature structure (Im3m̄) the selenium is body-centered cubic, while silver ions occupy the interstitial sites. The more complex low temperature phase was described by Wiegers [198]. The silver sits on two sites in the low temperature phase. One of the silver sites is coordinated tetrahedrally by four selenium atoms and the other is coordinated trigonally planar to three selenium atoms.

A diffractogram was measured at room temperature from $2\theta = 10°$ to $2\theta = 100°$. The sample was then heated at 1K per minute to 450 K (well above the nominal phase transition temperature of 413 K [136]. A diffractogram was measured at that temperature as well. The sample was cooled at 1K per minute to room temperature and
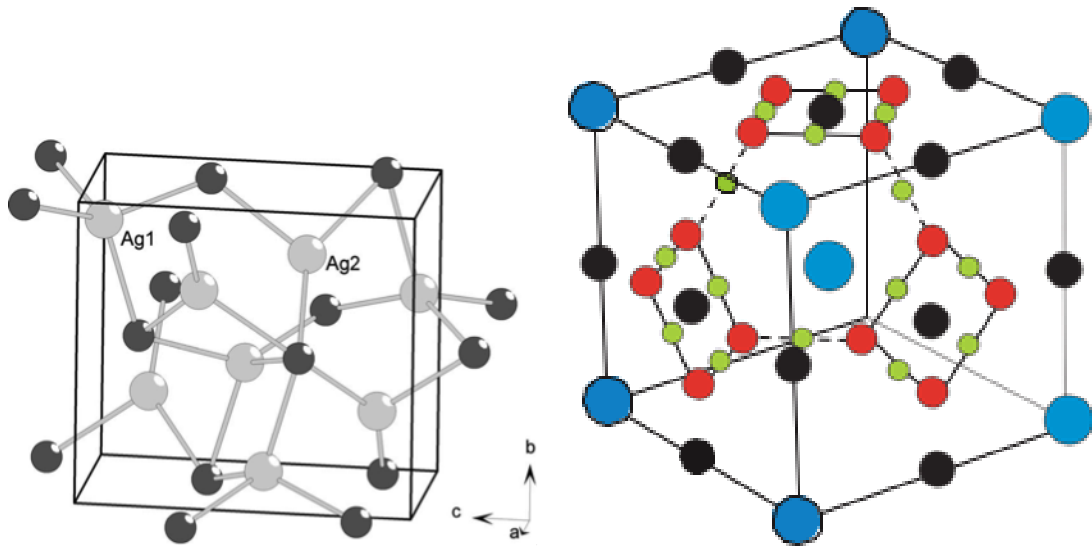
Figure 5.4: Low Temperature (a) [15] and high temperature (b) [18] structure of Ag$_2$Se
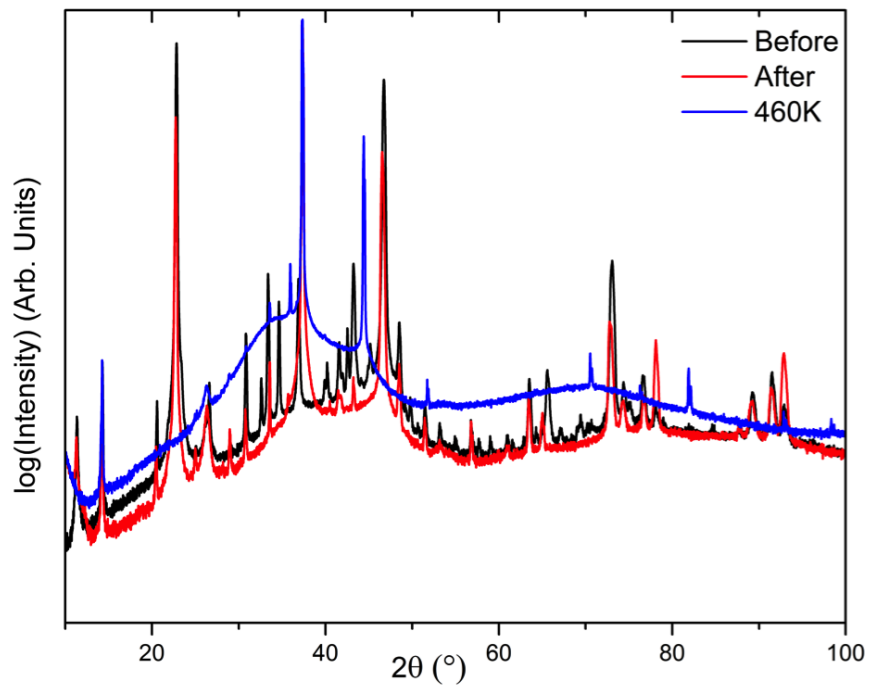
Figure 5.5: Powder X-Ray Diffractogram for Ag$_2$Se above and below its phase transition. All symmetries of the high temperature phase are present in the low temperature phase.
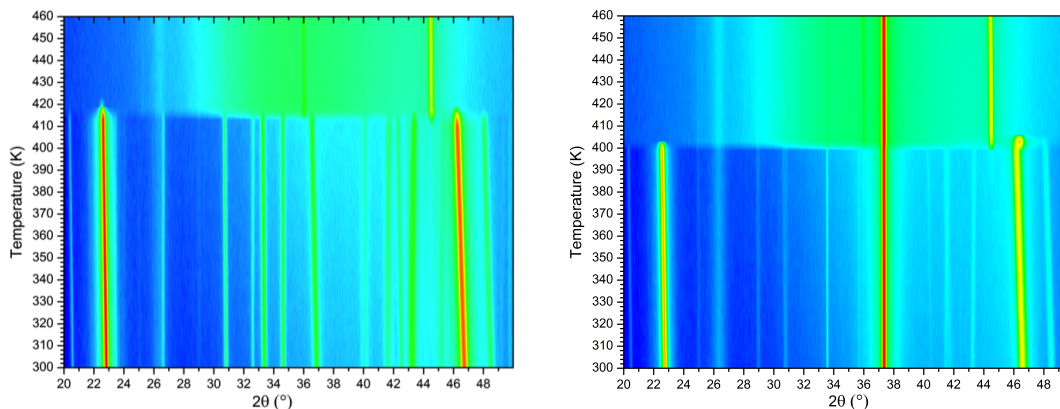
Figure 5.6: Temperature dependent X-ray diffractograms measured on heating (a) and on cooling (b) of Ag$_2$Se. A first order transition is seen at 415 K on heating and 401 K on cooling.

a third diffractrogram measured. All three diffractograms are shown in Figure 5.5(a).

Both above [145] and below [207] the transition the measured peaks index to previously published data, however large intensity mismatches are observed. These intensity mismatches were also observed by Billeter *et al.* [15] and ascribed to Se precipitation. This problem is likely more significant in the powder XRD as compared to bulk samples due to their larger surface area to volume ratio. No Ag is visible in the diffraction patterns at any temperature. Since a bulk synthesis product was used, large grain sizes are expected and the observed intensity mismatch is ascribed to this. The low temperature modification is orthorhombic (Space group P2$_1$2$_1$2$_1$) which explains the different dependences of the peak positions below the transition. The low temperature space group maps homomorphically to the high temperature space group (Im$\bar{3}$m); that is, all symmetries of the low temperature phase are preserved in the high temperature phase.

During the heating and cooling process diffractograms were measured from $2\theta = 20°$ to $2\theta = 52°$ in order to determine the nature of the phase transition. The duration of each scan was three minutes and consequently the temperature changed by 3 K from start to end of each scan. From inspection of a color map of this data there is a first order phase transition observed at 415 K on heating (Figure 5.6(a)) and 401 K on cooling (Figure 5.6(a)), with the phase transition temperature halfway in between
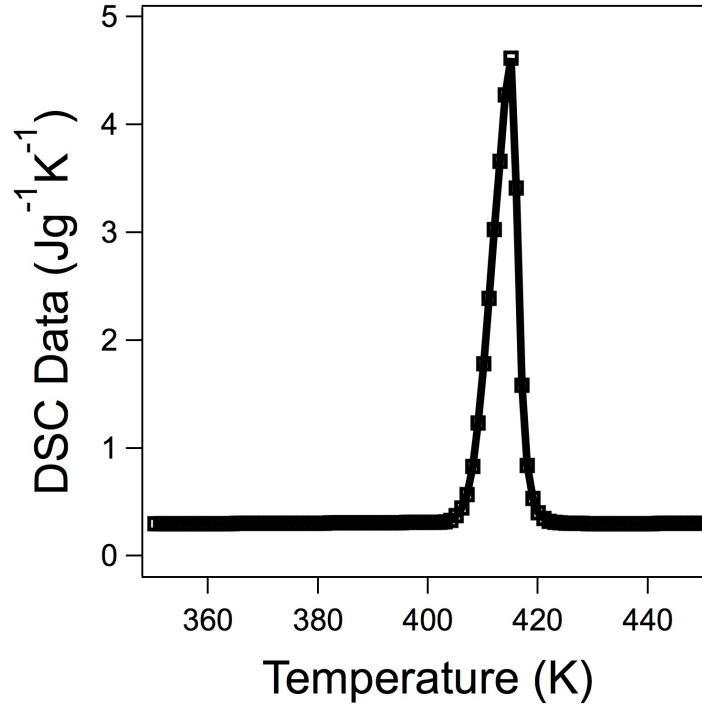
Figure 5.7: Differential Scanning Calorimetry data for Ag$_2$Se

at T$_c$ = 408K. This is consistent with literature reports [15, 136]. The discrepancy of the phase transition on heating and cooling is characteristic of a first order process and a consequence of the non-adiabatic heating.

The color maps show strongly diffuse background scattering. While significant in the low temperature phase, in the high temperature phase it makes distinguishing the peaks visually almost impossible. This suggests diffuse scattering, much like in a glass, that may cause phonon scattering and low thermal conductivity. The exception is a sharp peak at $2\theta = 37.2°$ that is visible on cooling but not on heating.

Differential scanning calorimetry data for Ag$_2$Se(Figure 5.7(a)) shows a sharp symmetric peak centered at 414 K. This peak is characteristic of a first order transition. Due to the preponderance of literature [15, 137, 21] evidence and the crystallographic evidence presented above for Ag$_2$Se's first order transition, it was unnecessary to confirm the order of the phase transition via altering the heating rate. The region of elevated calorimetry data extends from 402 K to 426 K. The DSC curve of a first order transition should *begin* to increase at the phase transition temperature. By
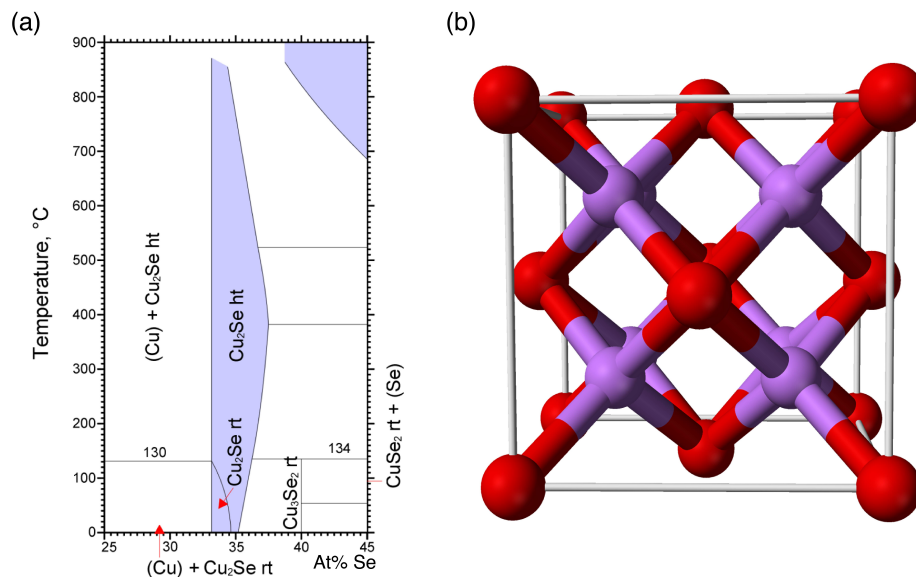
Figure 5.8: Phase diagram (a) of Cu$_2$Se system in the vicinity of Cu$_2$Se adapted from Heyding [78]. The phase transition is between the $\beta -$ Cu$_2$Se(RT) phase and the $\alpha -$ Cu$_2$Se(ht) phase. Anti-fluorite structure (b) of which $\alpha -$ Cu$_2$Se is a modification. Se is coordinated FCC and is represented in red. Ground state Cu is tetrahedral coordinated to the Se though significant occupation of trigonal planar and octahedral interstitials has been measured. The structure of $\beta -$ Cu$_2$Se is unknown.

drawing intercepting tangents to the behavior before and during the rise, the phase transition temperature is determined to be approximately 407 K. This agrees with the temperature of 408 K determined above by crystallography.

Both crystallographic and calorimetric studies indicate Ag$_2$Se to have a phase transition at $408K$.

5.3   Cu$_2$Se

The description of the phase transition behavior of Cu$_2$Se is complicated by the unsettled argument over the nature of that phase transition and the structure of the low temperature phase. The high temperature phase is at this point fairly well understood. The material is a known, if not abundant, mineral under the name of Berzelianite. During the same work in which he indexed high temperature Ag$_2$Se, Rahlfs also indexed high temperature Cu$_{1.85}$Se [161]. All the compositions of Cu$_{2-\delta}$Se

from $\delta = 0$ to $\delta = 0.2$ appear to have the same high temperature anti-fluorite cubic structure [78, 194, 201]. (Figure 5.8) Though that phase is on average anti-fluorite, significant Cu^+ occupation of trigonal planar and octahedral interstices is observed [201]. Hopping through these interstices is the mechanism of fast copper ion transport; the ion transport pathways have been successfully determined to be along the [111] direction from tetrahedral to trigonal planar intersticies [43, 42].

Despite Cu_2Se presence in mineral form and its binary compositon, the ordered low temperature structure is yet unknown. This is not for lack of trying. In 1987 Milat *et al.* [134] proposed a monoclinic supercell and in the course of that work noted eleven other proposed structures. They proposed a structure that assumed significant octahedral occupation. Later authors proposed more complex superstructures [123, 96]. These structures are insufficiently complex to explain the crystallography data presented below.

Multiple authors have proposed a co-existence transformation between the α and β phase with a temperature width of 10's of Kelvins [41, 188, 121]. This hypothesis, though reasonable, is contradicted by the data presented in this chapter. There are three reasons for this. The $Cu_{1.8}Se$ is commensurate with the α Cu_2Se. In the region $\delta = .05$ to $\delta = .2$ there actually is a coexistence of the β-Cu_2Se phase and the $Cu_{1.8}Se$; if the phase diagram is determined imprecisely, the single phase region goes unnoticed. Finally, unknown errors in synthesis have led to samples showing impurity phases of $Cu_{1.8}Se$ [121]. As room temperature $Cu_{1.8}Se$ has the same structure as $\alpha - Cu_2Se$ [78], this is an easy confusion to make. There is indeed co-existence of $\beta - Cu_2Se$ and $\alpha - Cu_{1.8}Se$ in such samples, but it is a co-existence of admixture rather than that of synthesis. Vengalis *et al.* [190] observed that this phase tends to form on the grain boundaries of copper rich phases.

Prior to this work the 410 K phase transition was believed to be first order. This is unsurprising, as it takes careful measurement and analysis to differentiate a lambda second order transition from a first order transition. The difficulties of this determination are well illustrated in the case of the lambda transition of β quartz [184, 82]. As late as 1980 authors were still confused about the lambda nature of its
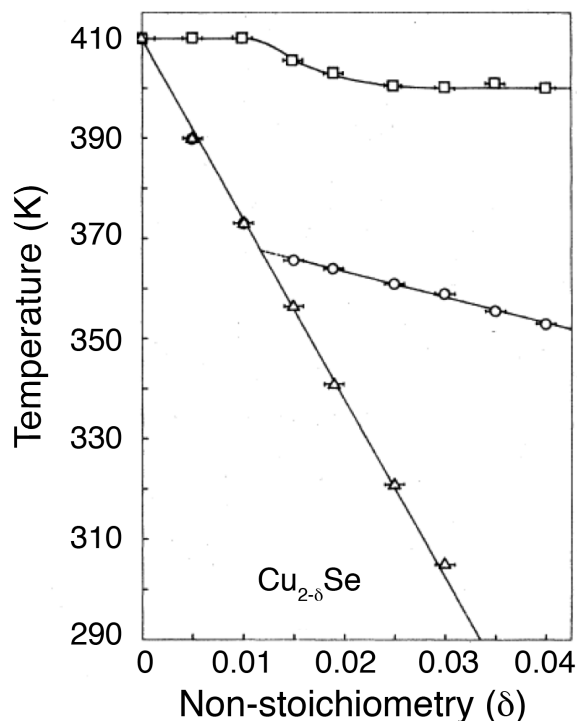
Figure 5.9: The phase diagram of Cu$_2$Se in its single phase region by Vucic.[194] This diagram was established by dilatometry. Notably, there are multiple phase transitions.

phase transition [82]. While structural second order transitions with diverging heat capacity are of interest to the physics community, they are far less common than first order transitions. Korzhuev determined Cu$_2$Se's transition to be first order on the basis of the Clausius-Clapeyron relations [105]. However, Pippard showed than an analagous relation holds for lambda-type transitions [157]. Vucic determined it to be first order on the basis of its sharp feature in their dilatometry data [191]; again, such sharp features are also expected in the case of a lambda-type second order transition [157]. Qualitative assesment of sharpness of thermophysical peak at a phase transition temperature can differentiate a first order transition from a second order transition without diverging heat capacity [140]; it is insufficient for differentiating a first order transition from a lambda-type second order transition.

Despite this confusion there is some certainty about the phase diagram at room temperature. By electrochemical determination [197] Korzhuev *et al.* found there to be a single phase region of Cu$_{2-\delta}$Se [101] for $\delta = 0$ to $\delta = 0.05$ and a range of co-
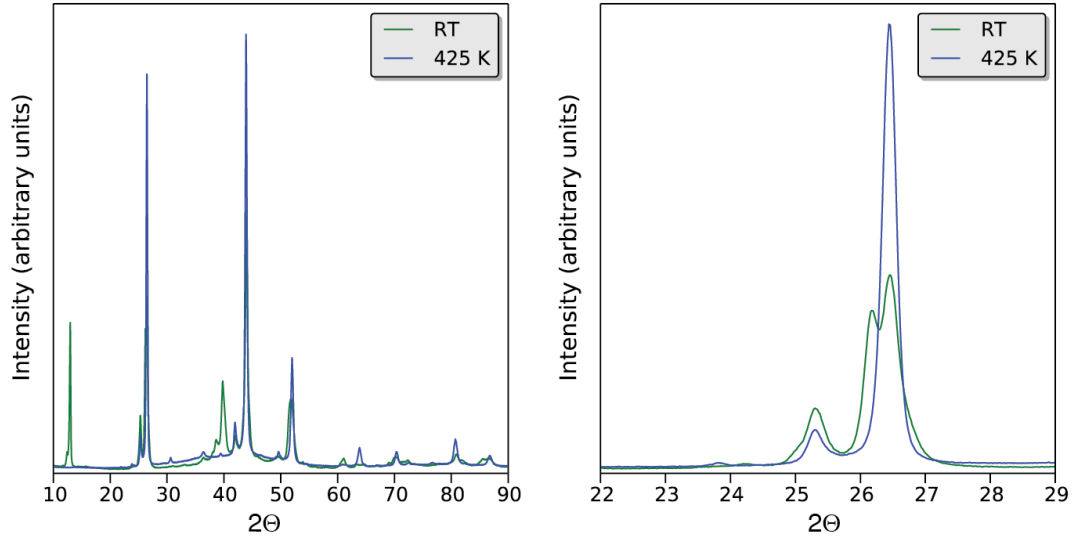
Figure 5.10: Left:PXRD of Cu_2Se at 300 K and 425 K from $2\theta = 10°$ to $90°$. Right: Zoom in near the $26°$ peak set. Peaks positions as identified in literature were observed [96]. The sample is single phase.

existence of $Cu_{1.95}Se$ and $Cu_{1.8}Se$ from $\delta = 0.05$ to $\delta = 0.20$. Temperature dependent dilatometry was performed by Vucic *et al.* in the single-phase region, and he developed a phase diagram on this basis, see Figure 5.9. Vucic's collaboration made follow up transport measurements [194, 134, 84, 192]. In general our sample shows the properties that Vucic observed in his samples of nominal composition $Cu_{1.99}Se$.

5.3.1 Diffractometry

A diffractogram was measured at room temperature from $2\theta = 10°$ to $2\theta = 90°$. The sample was then heated at 1 K per minute to 425 K (above the nominal phase transition temperature of 410 K. A second diffractogram was taken at 425 K. These diffractograms are shown in Figure 5.10. The low temperature diffractogram is consistent with literature reports [96]. The bifurcation of the major $\alpha - Cu_2Se$ peaks in the $\beta - Cu_2Se$ phase is consistent with the β phase being a monoclinic or orthrhombic modification of the anti-fluorites structure. $Cu_{1.8}Se$ impurity phase observed by Liu et al. was not observed here [121].
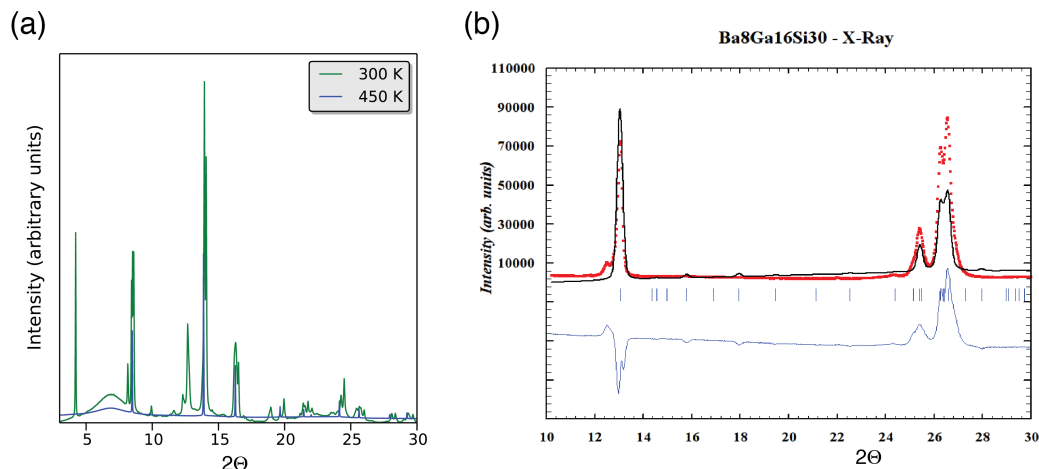
Figure 5.11: High flux low angle synchotron data of Cu_2Se (a) shows significant strong reflections, indicating that a large unit cell to explain the data. The recent models of Liu *et al.* [123] show a better fit than those previously published, [134, 96] but cannot explain all the low angles peaks observed (b). In (b) the black line is the data, the red line the model, and the blue line their discrepancy. Courtesy of Kasper Borup.

My crystallography collaborators were unable to resolve the low temperature structure. They determined that though many authors have proposed structures for Cu_2Se, these structures use a large enough unit cell to explain all of our observed peaks and their intensities. Many of these proposed structures are based on analysis of lower signal to noise diffraction data than that presented here; consequently, those authors propose structures that are too simple. Kashida and Akai [96] proposed a monoclinic unit cell (a = c = 7.14 Å, b = 81.9 Å, $\beta = 120°$) with ordering of copper vacancies, while Milat et al. proposed an even larger monoclinic cell (a = c = 12.30 Å, b = 40.74 Å, $\beta = 120 \pm 1°$). [134] Neither of these unit cells were able to describe the position of all reflections at low angles observed via high flux synchrotron.(Figure 5.11(a)). This indicates the structure to be even more complicated. These low angle peaks were not measured previously with the precision done in this experiment. Since publication of my paper [23], Liu *et al.* [123] proposed a triclinic unit cell (a = 7.12 Å, b = 7.14 Å, c = 7.51 Å, $\alpha = 98.6°$, $\beta = 107.6°$, $\gamma = 60.1°$) and a monoclinic unit cell (a = 7.13 Å, b = 12.36 Å, c = 14.47 Å, $\beta = 100.4°$) with larger unit cells than that proposed before. These structures were also unable to clar-
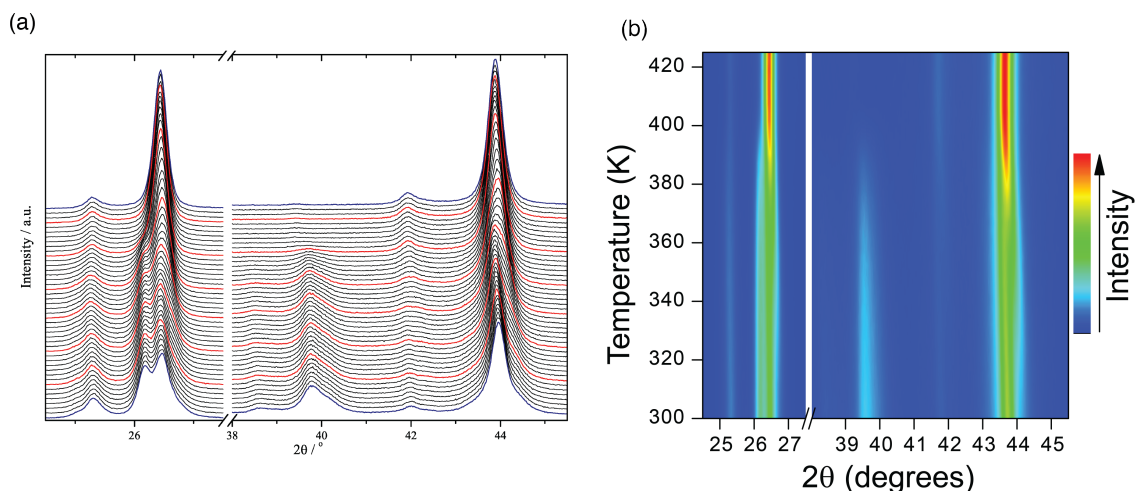
Figure 5.12: Temperature varied diffractograms of Cu$_2$Se. Data is presented as stacked diffractograms (a) and as a color map (b). The peak intensities and angles shift continuously from the low temperature to the high temperature phase.

ify all of our observed peaks nor determine their intensities correctly. This is shown for the proposed monoclinic structure in Figure 5.11(b). Therefore, no structural refinement below the phase transition is possible from PXRD at present, and the order parameter is not easily obtained from this method.

The 425 K diffractogram (Figure 5.10) is well fit by an anti-fluorite structure with the exception of a few anomalous peaks. These anomalous peaks are not present in the synchotron data from 450 K, see Figure 5.11, suggesting that either the phase transition is not fully complete at 425 K or that insufficient time was taken to let the kinetics stabilize at 425 K before measuring the diffractogram. Based on the PXRD and synchrotron data I conclude that the Cu$_2$Se measured for this study is single phase and in concordance with other single phase samples synthesized for literature studies.

For crystallographic determination of the nature of the phase transition, diffractometry must be performed at a series of temperatures that transverse that transition. During the heating process to 425 K for obtainment of the diffractogram of $\alpha - $ Cu2Se (Figure 5.10), diffractograms were continuously measured from $2\theta = 23°$ to $2\theta = 45°$. The duration of each scan was three minutes and consequently the temperature changed by 3 K from start to end of each scan. The 2θ range was chosen
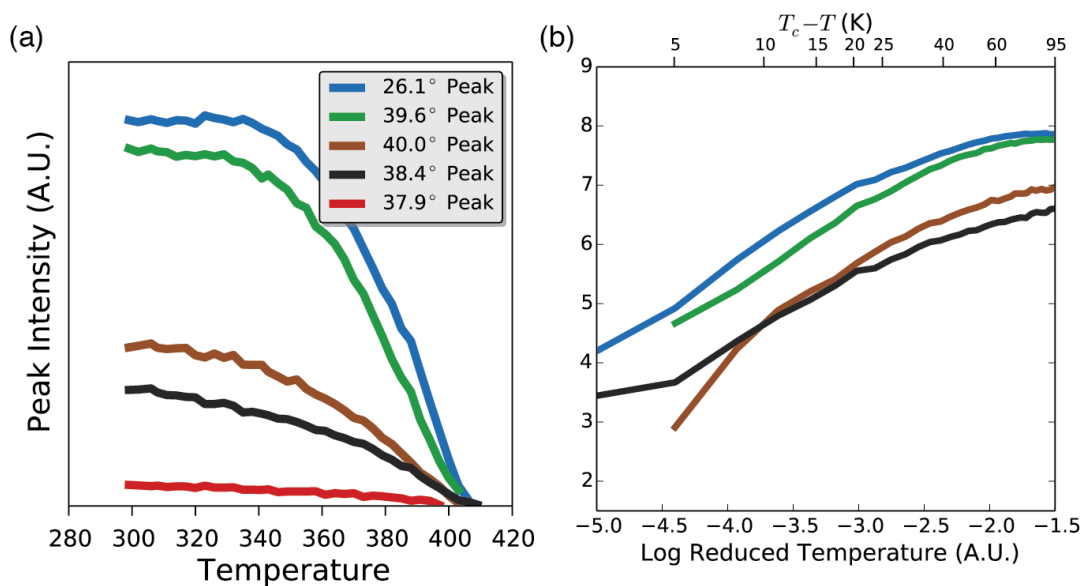
Figure 5.13: Peak intensities versus temperature (a) for selected peaks of Cu_2Se. These peaks were chosen because they only appear in the low temperature phase. They show a continuous decrease to the phase transition temperature. This decrease corresponds well with a critical power law, as seen by the linearity of log-intensity versus log-reduced temperature.

because of the excellent signal intensity and the two separate bifurcated peaks seen. Visualization of this data (Figure 5.12) shows a continuous evolution of the bifurcated peaks at low temperature into the single peaks at high temperature. Both the peak intensities and angles shift continuously from the low temperature to the high temperature phase. This strongly contrasts with the abrupt change that would be seen as in a first order transition (*i.e.*, that of Ag_2Se presented above in Figure 5.6). Cu_2Se does not have a first order transition.

Detailed analysis of the temperature resolved PXRD data confirms Cu_2Se's phase transformation to be continuous. For a second order phase transition, it is expected that a crystallographic order parameter should go to zero with some exponent of the reduced temperature $\tau_r = (T_c - T)/T_c$. To examine this effect, we plot the peaks that disappear at the phase transition temperature (Figure 5.13(a)). These peaks show critical power law behavior as the phase transition temperature is appraoched (Figure 5.13(b)). The data at the phase transition is insufficiently detailed to ex-
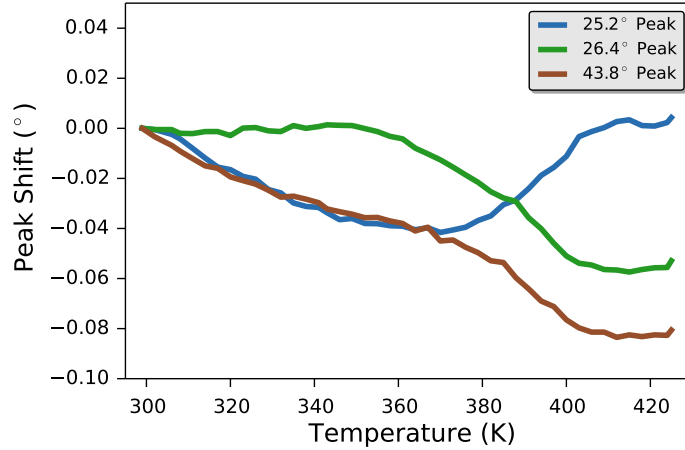
Figure 5.14: Temperature dependence of the peak shift for representative diffraction peaks of Cu_2Se. The peak shifts are incompatible with a coexistence transformation.

tract a precise critical exponent; the data resolution for such a fit must be increase exponentially higher as the phase transition temperature is approached. The critical exponents so obtained would be far larger than unity. This is greater than the critical exponent expected for the Ising model [95] and found in other super-ionic transitions [118]. It is therefore likely that while the critical exponents of the peaks are related to the order parameter, their critical exponent is not that of the order parameter (canonically labeled β). T_c was determined to be 408 K, as that temperature gave approximately the some slope in Figure 5.13(b) for angles analyzed. This critical temperature is consistent with that found in the literature and determined by other thermophysical measurements for this thesis. The noise floor near the phase transition temperature prevented analysis of the critical exponent for the $2\Theta = 37.9°$ peak.

The shift in peak angles with temperature is inconsistent with an $\alpha \rightarrow \alpha + \beta \rightarrow \beta$ coexistence transformation. In a coexistence transformation the secondary peak in the bifurcation should be stable in peak position as its intensity increases, varying only due to thermal expansion. In contrast a second order transition the peaks will bifurcate smoothly from one another. The peak positions of Cu_2Se show such shifts in the temperature range from 360 K to 410 K. (Figure 5.14) Notably the $2\Theta = 25.2°$

and 26.4° shift in opposite directions; this is inconsistent with thermal expansion.

The phase diagram of Vucic (Figure 5.9) anticipates a (non-lambda) second order transition at a lower temperature. At 360 K there is a point of inflection in the peak shift of the $2\Theta = 25.2°$ and 26.4° peaks. The peak intensity and shifts in general begin to shift significantly at this temperature. While that is not definitive evidence of a second order transition at 360 K, more data relevant to that point will be presented later in this document.

A pair distribution function (p.d.f.) was obtained from total scattering data. It describes the distribution of distances between pairs of atoms in the structure. The changes of the p.d.f. are gradual, indicating that the ordering of Cu-interstitials occurs over a wide temperature range. There is no evidence of a first order discontinuity in peak positions nor of the β phase being present below 410 K. The phase transition does not appear to be complete until 450 K; transformation above the phase transition temperature is characteristic of second order transitions. The $Q_{max} = 26\text{Å}$ used is insufficient for truly accurate quantitative fitting, as indicated by the presence of substantial integration error ripples below the first peak maxima.

Even without modeling the data it is possible to extract qualitative information. By studying the high-temperature structure of Cu_2Se it is clear that the peak at $4.1\,\text{Å}$ (Figure 5.15(a)) is a superposition of the shortest Cu-Cu and Se-Se distances in the [110]-direction. Above 300 K the peak becomes increasingly asymmetric, indicative of multiple Cu-Cu distances in the high-temperature phase related to the disorder of Cu interstitials. At low temperature the Cu order to form a superstructure. The superstructure formation is most clearly seen in the region $8\,\text{Å}$ to $9.5\,\text{Å}$ (Figure 5.15(b)). This range corresponds to Cu-Cu distances in the [110]-direction in adjacent cubic unit cells. Below 410 K there are two distinct peaks at $8.2\,\text{Å}$ and $9.3\,\text{Å}$. However in the high temperature phase the same region is a continuum of overlapping peaks arising from the disorder of Cu.

Theoretical models of super-ionic conductivity assume that it is due to Frenkel defect formation — that a number of interstitial sites similar to the number of ions become occupiable in the higher temperature phase [21, 163, 70]. Such significant
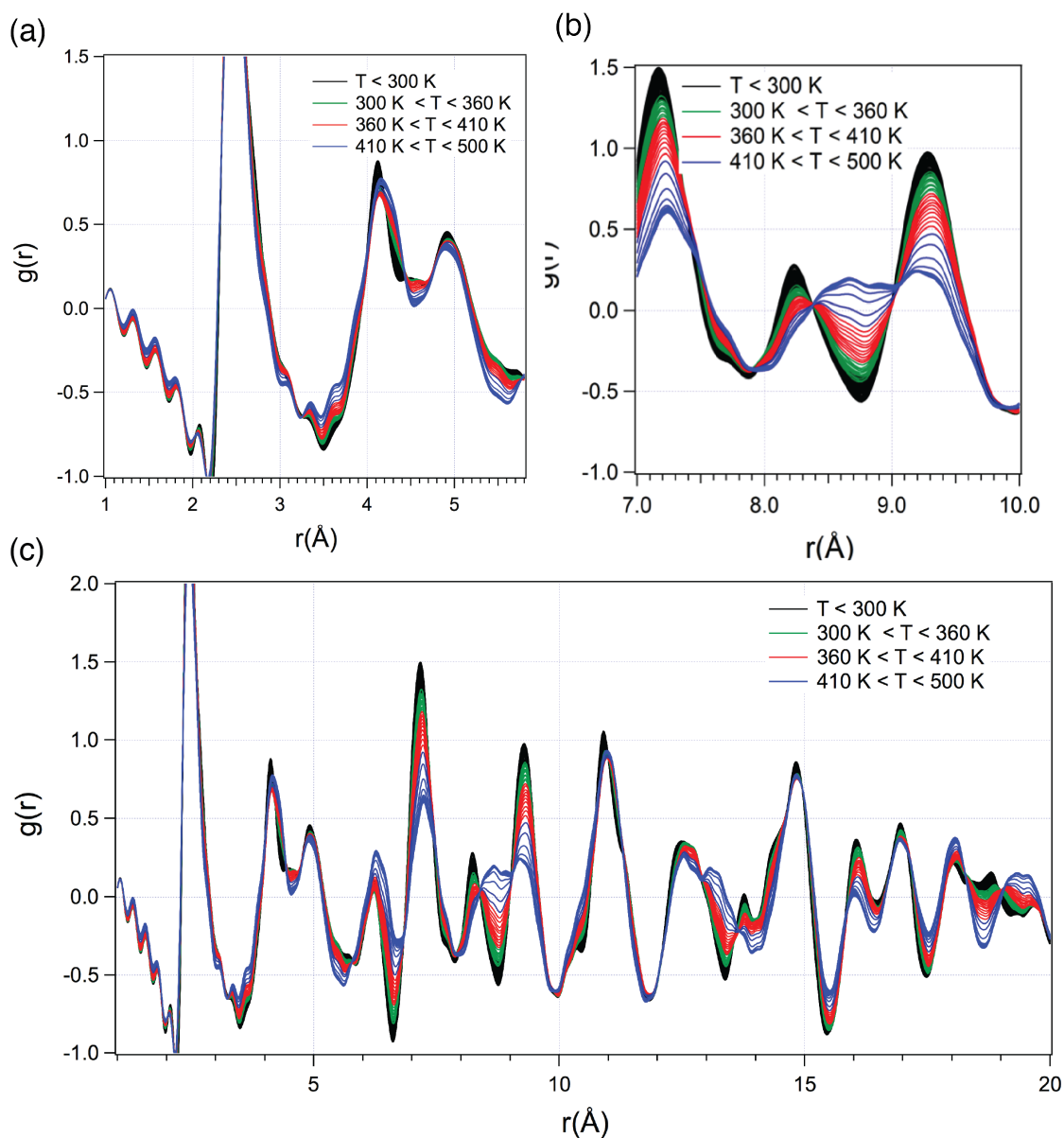
Figure 5.15: Pair distribution function data for Cu$_2$Se. The unit cell size is 5.8 Å. The coordination number remains the same through the phase transition (a) but correlations between high temperature equivalent unit cells breaks down.(b) Full data set. (c)
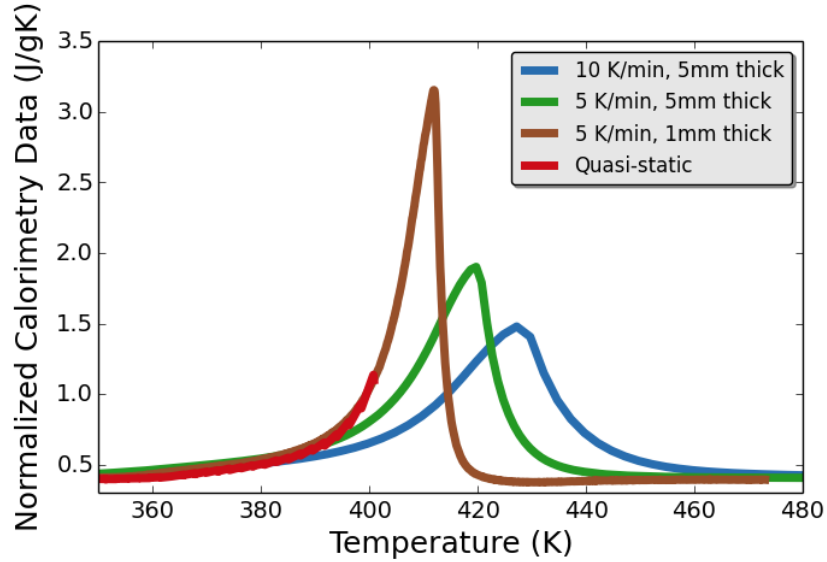
Figure 5.16: Calorimetry data for Cu_2Se under differing measurement condition. As the diffusive time scale is decreased, the data converges to the quasi-static heat capacity measured by Quantum Design Physical Property Measurements System (PPMS). The phase transition temperature is marked with a black dotted line. Data courtesy of SIC-CAS and the JPL Thermoelectrics Group.

Frenkel defect formation should result in new peaks in $g(r)$ for r less than the lattice spacing of the high temperature phase (5.8$\mathring{A}$). While the peaks in this range are broadened, Figure 5.15(a), there is nothing to suggest significant new site occupation. For unit cells greater than $5.8\,\mathring{A}$ a much more substantial change is observed. (Figure 5.15(b)) This suggests that the correlations between high temperature unit cells breaks down substantially. The implication of this is that rather than the disordering being due to Frenkel defect formation, it is primarily due to a breakdown of correlations between unit cells, as represented by the $8.2\,\mathring{A}$ and $9.3\,\mathring{A}$ peaks. It is unclear at this time what the microscopic mechanism for correlations between unit cells is. One possibility is that the order state of the super-ionic transition is supported by a local electronic polarization like in a ferroelectric.

5.3.2 Cu$_2$Se **Calorimetry**

Calorimetry data also supports Cu$_2$Se being a second order transition. In order for a DSC measurement to accurately represent a material's heat capacity, the heating rate should be much faster than the timescale of thermal equilibriation. At a first order transition there is an instantaneous enthalpy release. This enthalpy cannot be transported out of the material instantaneously, and so a temporary difference between the temperature of the bath and the temperature of the sample occurs. Therefore, a first order phase transition will show a peak of finite width at its phase transition. For example, in the Ag$_2$Se calorimetry curve presented above.(Figure 5.7(a)), the heat capacity is elevated over the Dulong-Petit baseline from $405K$ to $420K$. Over this temperature range the sample is not in thermodynamic equilibrium with the bath. For the phase transformation to be complete a quantity of heat equal to the enthalpy of formation may be added, but the rate at which heat may be added is limited by the material's thermal diffusion time scale (t_D) and its heating rate $(\dot{T})$. This can be written mathematically as:

$$\delta T = A t_D \dot{T}, \tag{5.7}$$

in which A is a constant term that serves as a catch-all for the geometric configuration of the apparatus and sample. As discussed in Chapter 2 in the context of thermal diffusvity measurements, the diffusion time scale is related to the diffusion length (l_D) by $t_D = l_D \cdot D_t^{-1}$. This provides a scaling relation by which measurements on different size samples and heating rates can be compared.

$$\delta T = A \frac{l_D^2}{D_T} \dot{T} \tag{5.8}$$

Because of the smearing of the enthalpy of formation, it is easy to accidentally mistake a second order transition with diverging heat capacity for a first order transition. The historical case of the β-quartz transition exemplifies this difficulty [85]. Considerations based on heating rate and sample size have proved successful in the past for differentiating first and second order phase transitions [140].

The enthalpy released per unit temperature of a lambda-type transition is always finite. However, the low thermal diffusivity and non-linearity in the heat capacity may still lead to errors in the DSC derived heat capacity. A fixed temperature rate induces an error in the heat capacity resolution due to the sample's thermal diffusivity. Two separate samples were sent to SIC-CAS and JPL for DSC measurement. The heat capacity measured at these two facilities showed markedly different calorimetry curves (Figure 5.16) that can be explained by Equation 5.7. The JPL sample had a thickness of 2.5 mm, while the SIC-CAS sample had dimensions of approximately 0.8 mm. On this basis the 5 Kelvin per minute and 10 Kelvin per minute JPL measurements are expected to have a temeprature errors 10 and 20 times that of the SIC-CAS sample. The maximum of three curves are at 412 K, 420 K, and 427 K, which corresponds well to the predicted trend and indicates an error on the SIC-CAS temperature resolution of less than 1 Kelvin.

On this basis the c_p derived from the SIC-CAS DSC measurement is judged to be accurate enough for calculating transport data. The DSC heat capacity was further confirmed via the quasi-static method of the Quantum Design Physical Property Measurement System to 400 K with the assistance of Dr. Xun Shi of SIC-CAS. In this methodology the temperature is stabilized before the heat capacity is measured. Within each three point set the variation in measured heat capacity is less than 1%, indicating that the equilibrium condition was met. These measurements confirm that the heat capacity is increased at the phase transition temperature.

At 355 K there is a distinct change in the slope of the heat capacity.(Figure 5.17) This is consistent with a (non-lambda) second order phase transition and the predictions of Vucic. This extended elevation is inconsistent with a first order transition and consistent with a second order transition. There is a distinct change in the slope of c_p with T at 355 K. That feature is indicative of another second order phase transition and accords with the phase diagram of Vucic. A feature near this temperature was observed in the temperature crystallographic measurements discussed in the previous subsection. The calorimetry data is consistent with two second order phase transitions at 360 K and 410 K. The transition at 360 K has a heat capacity that converges
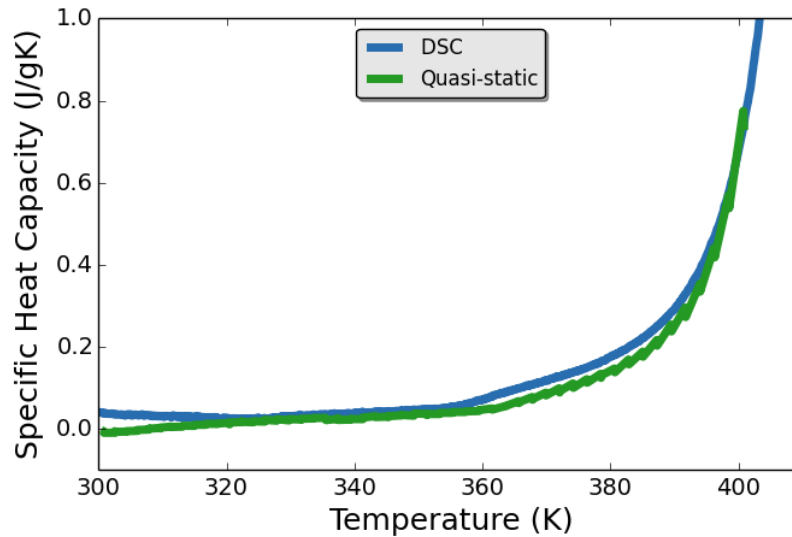
Figure 5.17: Heat capacity minus Dulong-Petit heat capacity below the phase transition temperature. Data is shown both for the DSC measurement and the quas-static PPMS measurement. The non-linear elevation in heat capacity begins at $355K$.

to zero, while the transition at 410 K has a divergent heat capacity.

5.4 $Cu_{1.97}Ag_{0.03}Se$

At room temperature the material's main phase has a structure related to the room temperature structure of Cu_2Se. This structure has not been satisfactorily solved in the literature but it is believed to be equivalent to the high temperature structure but with ordered Cu vacancies and interstitials. The ordering is believed to depend highly on the exact stoichiometry, which may explain the lack of a unit cell that describes the low temperature structure. Of the peaks that could not be related to Cu_2Se peaks, CuAgSe and at least two distinct impurity phases are identified. At least one impurity phase is still present at high temperature and at least one impurity phase dissolves at the phase transition at 400 K, see Figure 5.18. The CuAgSe impurity phase is clearly visible in scanning electron micrographs of the sample, see Figure 5.19. The impurity peaks that dissolve do not have corresponding peaks in Cu_2Se and are hence believed to be impurities; however, it is possible that they belong to the main phase if this has
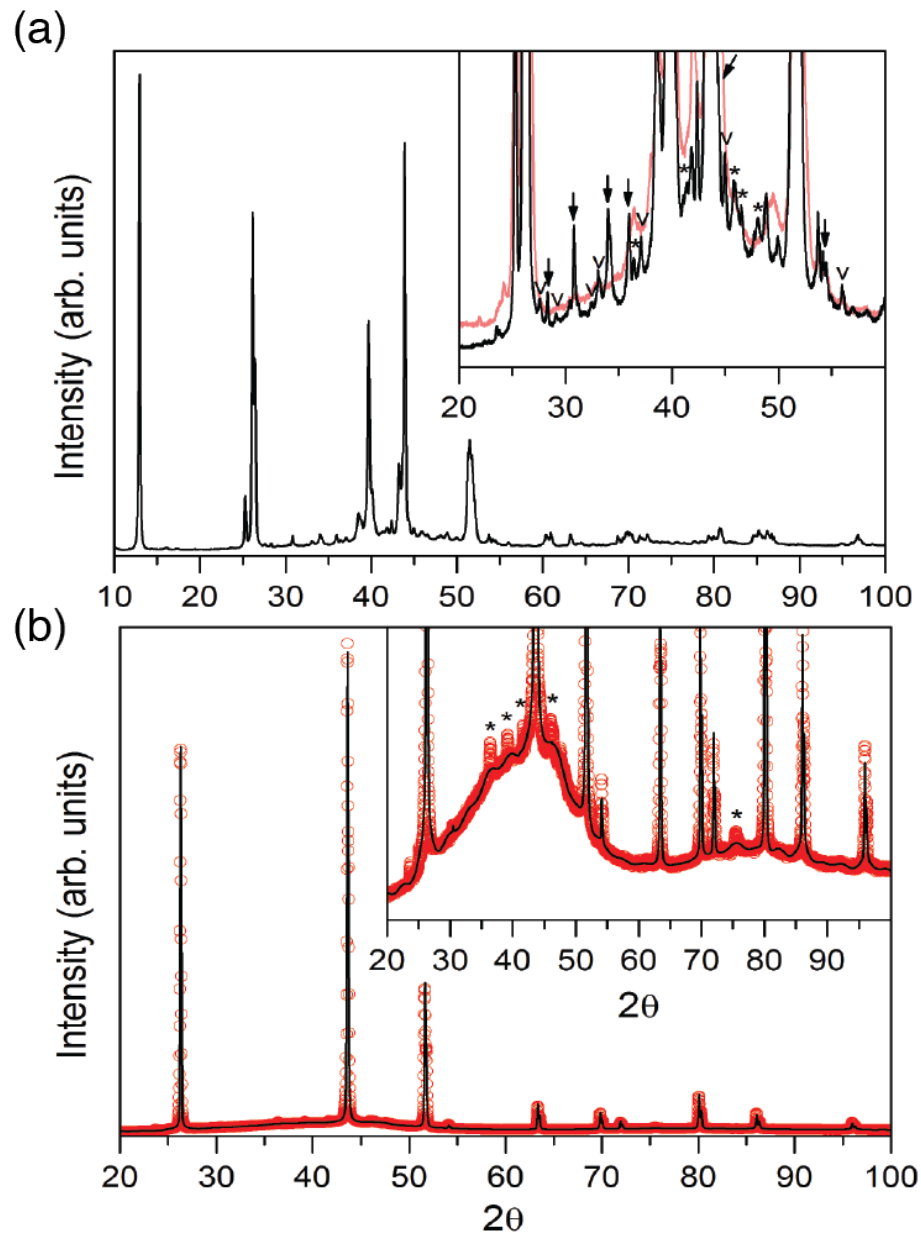
Figure 5.18: Room temperature (a) and 450 K (b) diffractograms of $Cu_{1.97}Ag_{0.03}Se$. Impurity peaks marked v disappear at the phase transition, while those marked * remain. Peaks marked with an arrow correspond to CuAgSe. Courtesy of Kasper Borup.
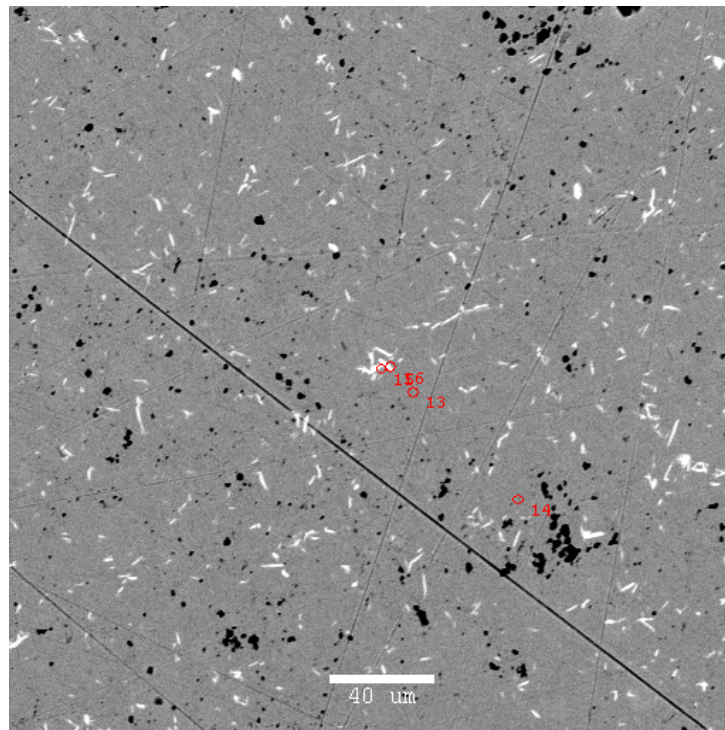
Figure 5.19: Scanning electron micrograph of $Cu_{1.97}Ag_{0.03}Se$ courtesy of Tristan Day. Gray areas are Cu_2Se phase, black areas are voids and white areas are CuAgSe
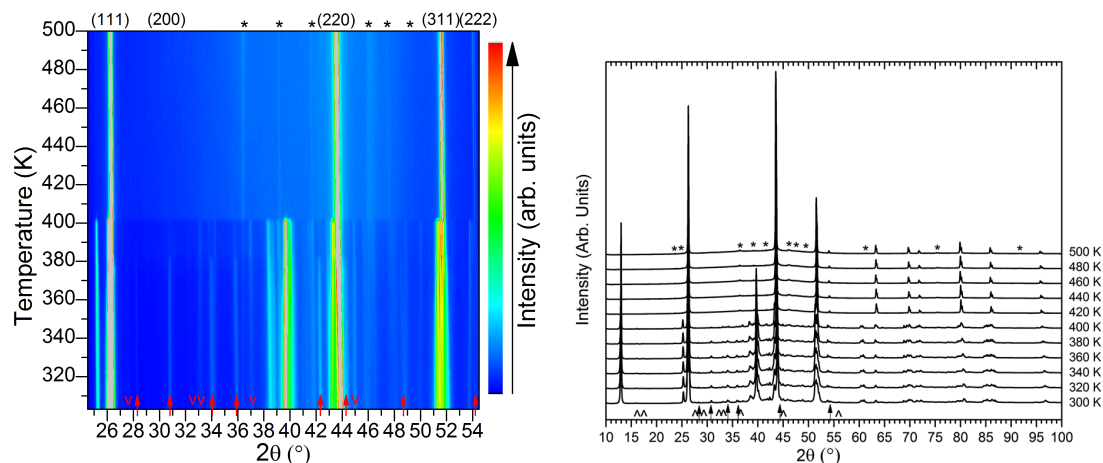
Figure 5.20: Left: Color map of temperature varied diffactrograms of $Cu_{1.97}Ag_{0.03}Se$. Right: Slower diffractograms were performed at 20 K intervals. Impurity peaks marked v disappear at the phase transition, while those marked * remain. Peaks marked with an arrow correspond to CuAgSe and dissolve at 380 K. The high temperature reflections of Cu_2Se are labeled on top of the graph. Courtesy of Kasper Borup.

a structure different from Cu_2Se.

Diffractograms were measured on constant heating continuously from $2\theta = 24°$ to $2\theta = 55°$. A color map is presented in Figure 5.20(a). The duration of each scan was three minutes and consequently the temperature changes by 3 K from start to end of each scan. During heating, dissolution of CuAgSe was observed at 380 K. At $\approx$400 K there was a structural transition of the primary phase to a high temperature structure, which remained present and unchanged to 500 K. All peaks except few low intensity impurity peaks (also present at room temperature) can be indexed and refined with the high temperature Cu_2Se structure. Every 20 K higher quality diffractograms were recorded, during which the sample was held at constant temperature for at least 45 minutes. At 380 K, CuAgSe was present and unchanged both before and after the 45 minute scan, and hence this is not believed to affect the dissolution. No change in CuAgSe is observed until the diffractogram labeled 384 K (scans are labeled according to the sample temperature when they are started). The same is true for the primary phase and dissolved impurity at 400 K.

The structural phase transition has both a first and second order component. The
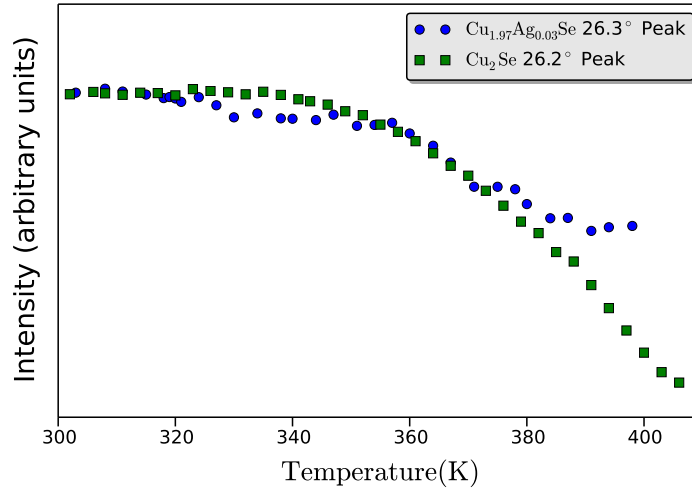
Figure 5.21: Comparison of the $2\Theta = 26.2°$ peaks of both Cu_2Se and $Cu_{1.97}Ag_{0.03}Se$. All units are arbitrary and scaled to be identical at $T = 300$ K. Up to 380 K the peak of $Cu_{1.97}Ag_{0.03}Se$ follows the second order trend of Cu_2Se. On dissolution of CuAgSe at 380 K its intensity stabilizes while temperature increases, until the first order transition at ≈ 400 K eliminates the peak entirely.

structure is gradually changing from room temperature and up. This is evidenced by the peaks moving relative to each other while the intensities also change. At the dissolution of CuAgSe there is a strong change, and again this appears not to be due to the 45 minute rest at 380 K. The dissolution of CuAgSe seems to result in a faster rate of transition. Contrary to pure Cu_2Se, many peaks seem to be shifting position, while others seem to only change intensity (except for a slight shift due to thermal expansion).

5.4.1 Cu_2Se and $Cu_{1.97}Ag_{0.03}Se$

From the crystallography data $Cu_{1.97}Ag_{0.03}Se$ appears to have an *interrupted* and distorted version of the second order transition of Cu_2Se, *i.e.*, it appears to be a weakly first order transition .The distortion occurs on dissolution of the secondary CuAgSe phase near 380 K. The interruption occurs at 403 K at which point the transition becomes first order. This behavior is best seen by comparing the temperature dependence of peak intensity of the $2\Theta = 26.2°$ peaks of both Cu_2Se and $Cu_{1.97}Ag_{0.03}Se$.
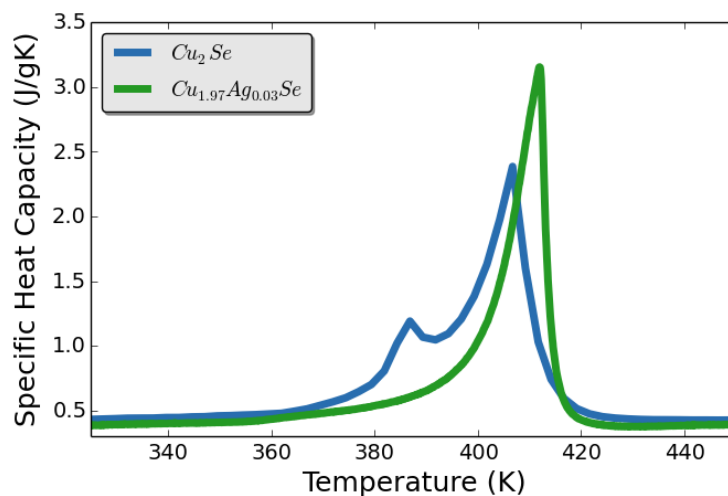
Figure 5.22: Differential scanning calorimetry for $Cu_{1.97}Ag_{0.03}Se$ in comparison with that of Cu_2Se.

Up to 380 K the peak of $Cu_{1.97}Ag_{0.03}Se$ follows the second order trend of Cu_2Se. On dissolution of CuAgSe at 380 K its intensity stabilizes while temperature increases, until the first order transition at $\approx 400\,K$ eliminates the peak entirely. These trends strongly affect the temperature dependence of $Cu_{1.97}Ag_{0.03}Se$'s transport behavior, as is to be discussed later in this thesis.

The heat capacity of $Cu_{1.97}Ag_{0.03}Se$ shows a doubled peak, see Figure 5.22 The temperature of the first peak corresponds to the temperature dissolution of the CuAgSe phase observed by crystallography. The temperature of the second peak corresponds to the first order transition. Some of what is labeled as specific heat in Figure 5.22 is surely enthalpy of formation due to the first order component of the phase transition. However, at this time I am unable to distinguish which portion belongs to the second order transition and which to the fist order transition. I will treat all the measured enthalpy from the DSC measurement as if it were due to a second order transition. This will lead to an overestimate in c_p and therefore an underestimate of zT, but I feel it is best to be conservative in my calculation.

Chapter 6

Transport in Ag_2Se

This chapter is principally about the thermoelectric performance of Ag_2Se near its phase transition. In the sample studied here the Hall carrier concentration does not differ measurably in the order and disordered phases; this fact considerably simplifies arguments based on band structure analysis. While many samples show similar behavior, other samples show a sharp increase in n_H in the disordered phase; the reason for this distinction remains unclear. Without any measured difference in band structure, the Seebeck and zT are enhanced in the ordered phase compared to the disordered.

This increase in zT is not easily explained using standard band-structure analysis (*e.g.*, BoltzTraP) [127]). In this chapter I will introduce super-ionics as thermoelectric materials and explain why they are of interest. Then I will provide a brief overview of the band structure modeling used for this thesis. After this I will present and analyze the transport data of Ag_2Se and argue that the difference in its properties above and below its phase transition are not easily explained by band structure modeling.

In the final chapter, after I have also presented the transport of Cu_2Se, I will develop an explanation for its physics on the basis of the phenomenology of order-disorder transitions [95] and Onsagers phenomenology of non-equilibrium thermodynamics [132]. I will suggest that these effects may occur broadly; it may be that the sudden transformation of the phase transition brings a more general effect into contrast.

6.1   Ion conducting thermoelectrics

Mixed ion-electron conductors (MIECs) are of recent and increased interest as thermoelectric materials [1, 199, 50, 133, 200, 206, 121, 30, 179, 185, 66, 45]. MIECs are materials that conduct both ions and electrons [167]. This is of course a very broad category that includes semiconductors and solid electrolytes. They can be subcategorized by the relative size of ionic conductivity (σ_i) and electronic conductivity (σ_e) with the physics varying substantially from the $\sigma_i \gg \sigma_e$ regime to the $\sigma_e \gg \sigma_i$ regime. In some materials such as solid oxides used in fuel cells, these regimes may be bridged in a single material under varying conditions of oxygen partial pressure and temperature.

Thermoelectric ion conductors operate entirely in the $\sigma_e \gg \sigma_i$ regime. This regime is inescapable unless an entirely new conception of what makes a good thermoelectric material is made as compared to what is studied now. A good thermoelectric is a heavily doped semi-conductor with a carrier concentration generally optimized at between $10^{18}\,\mathrm{cm}^{-3}$ and $10^{21}\,\mathrm{cm}^{-3}$ [180], and an electrical conductivity in the $10^4\,\mathrm{S/m}$ to $10^6\,\mathrm{S/m}$ regime in which the electronic (κ_e) and lattice (κ_L) portion of thermal conductivity are nearly the same. Super-ionics are by their phenomenological definition the best ionic conductors. They have ion conductivities that are similar to that of a liquid, $\approx 10^2\,\mathrm{S/m}$. Therefore even in the most extreme conceivable case an ion-conducting thermoelectric has σ_i less than 5% of σ_e.

Direct enhancement of thermoelectric material conductivity by adding ionic conduction is therefore impossible. Fortunately, this simplifies the measurement procedure for total thermal and electrical conductivity; the great care must be taken in making DC measurements of materials with two species with order of magnitude different diffusion timescales [167, 164, 165] can here be ignored. The principal consideration is that the electrodes are blocking to ions so that the ion conducting specie does not leave the material. Empirically the graphite blocker layer between thermocouple and electrode accomplished this purpose. When that layer was forgotten or broken through, the Niobium thermocouple wire used for the electrode developed a

fine metallic coating and was rendered useless.

The driver of recent interest in MIEC thermoelectrics has been their extremely low thermal conductivity. A principal problem of engineering good thermoelectric material is to find methods for scattering lattice vibrations (phonons) and thereby reduce κ_L without also scattering electrons and thereby reducing σ. In $Ag_2Se_{0.05}Te_{0.05}$ κ_L is only 0.5 W/mK at 400 K [50] and Ag_8GeTe_6 has been reported as having a glass-like thermal conductivity of 0.25 W/mK at 300 K with only negligible contribution from electrons. Though these nobel metal chalcogenides are the subject of this thesis and in fact have a longer history as thermoelectric materials than is commonly appreciated [24], the driver of the recent interest in MIECs has been $\beta - Zn4Sb3$.

In 1997 Caillat *et al.* first synthesized $\beta - Zn4Sb3$ as a thermoelectric material [30]. They determined it to have a maximum zT of 1.3 at 670 K which at the time was the highest ever measured at that temperature. This was driven by a κ_L at or slightly above $0.65 Wm^{-1}K^{-1}$ from $400K$ to $650K$. They determined this to be very close to the thermal conductivity of a glass in accordance with Cahills formalism [28, 29]. On the basis of crystallography Snyder *et al.* [179] suggested that this low κ_L was due to scattering off of disordered interstitals.

Density functional theory analysis by Toberer *et al.* [186] showed that the Zn interstitial sites were of almost identical energy to the ground state sites, with meta-stable pathways connecting them. Both a nearly isoenergetic interstitial site and meta-stable energetic pathways are considered necessary conditions for super-ionic conduction [87]. Tracer diffusion experiments confirmed Zn_4Sb_3 to have a liquid-like ion diffusivity with site hopping activation energy only 20% higher than that of AgI [35]. Zn_4Sb_3 is therefore a super-ionic thermoelectric material [21, 151].

Super-ionic materials are often written about as having a *molten* sub-lattice of conducting ions [22, 103]. As this analogy was coined in reference to the liquid-like diffusivity of the conducting ion ($10^{-5}\,cm^2/s$) and the enthalpy of formation comparable to that of their melt, [21, 22] care must be taken in extending it beyond its physical underpinnings. It has been suggested in two ways that the lattice thermal conductivity may have properties similar to that of a liquid: that they should show
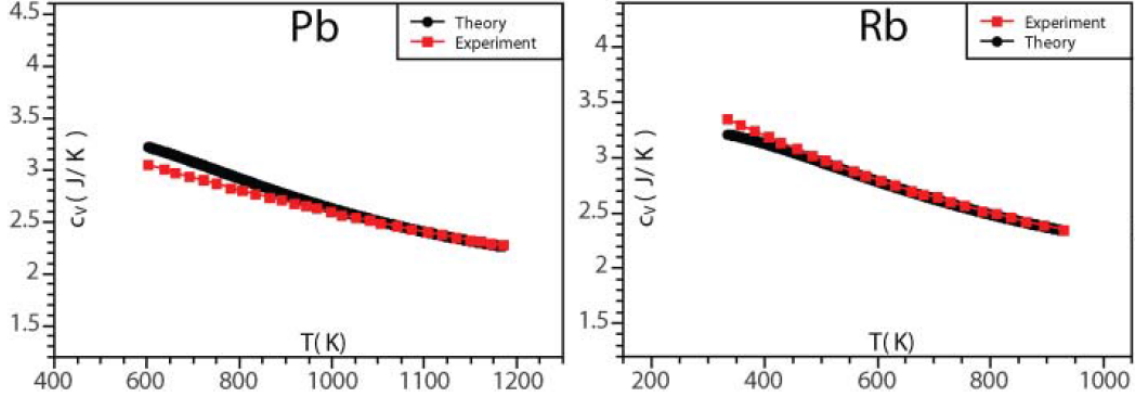
Figure 6.1: Heat capacity of liquid lead and rubidium with fit to theory. As temperature increases low frequence transverse modes disappear and thereby reduce c_V. Figure from Bolmatov *et al.* (2012) [17].

phonon softening due to coherent oscillations like a liquid [6], and that their constant volume heat capacity (c_V) should decrease with increasing temperature like a liquid [122, 189, 17].

The liquid-like heat capacity was proposed by Liu *et al.* in order to explain a decrease in c_P they observed above $800K$ in Cu_2Se [122]. While a solid has $c_V = 3k_b$, a liquid only has $c_V = 2k_b$ [189]. The solid heat capcity is due to the kinetic and potential energy contributions to heat capacity by the equipartition theorem. As in a mono-atomic gas, there are three degrees of freedom for position and momentum each and so c_v of a solid is $6 \times k_b/2 = 3k_b$. In a crytalline solid these contributions are split between two longitudinal and one transverse (or shear) propagation modes. A liquid is incapable of propagating all transverse oscillations and therefore loses the heat capacity associated with the potential energy of those modes (up to k_b).

In real liquids c_V is observed to decrease with temperature. Bolmatov *et al.* compiled data for twenty-one liquids showing this trend [17]. As an example, their data for Pb is shown in Figure 6.1. They model this trend as being due to two characteristic frequency. The first is the characteristic frequency of lattice oscillations, the Debye frequency (Ω_D). The second is the characteristic frequency of liquid hopping, which they call the Frenkel frequency (ω_F). Only shear modes with characteristic frequency ($\omega < \omega_F$) disappear. In this frequency regime the liquid atoms move fast enough to
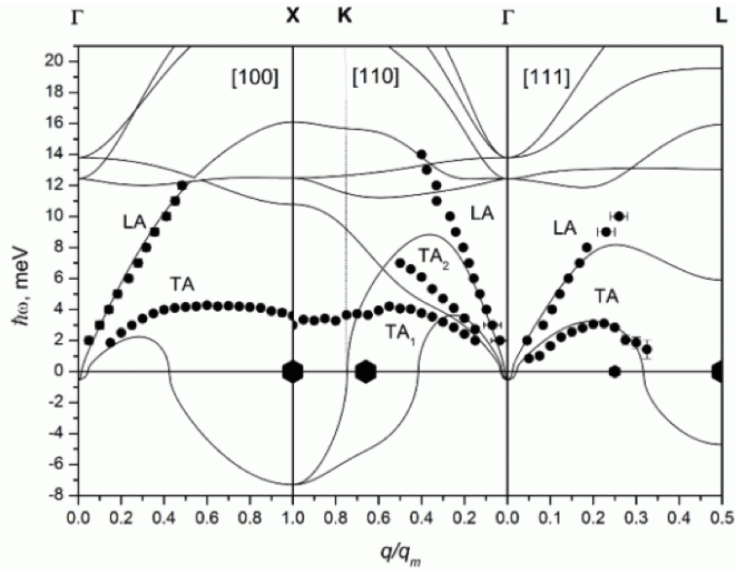
Figure 6.2: The fluctuations of ions between interstitial sites causes phonon mode to soften and scatter. In Zn_4Sb_3 Schwelka *et al.* [173] observed a strong anharmonic ratting of an Sb-dimer that they found could explain its anomalously low thermal conductivity. This behavior was found to effect the heat capacity even in the ordered phase, as evidenced by an Einstein peak in the heat capacity. If this behavior is a more general attribute of super-ionic materials in both their ordered and disordered phases, it may cause their low thermal conductivity. In his studies on single crystal $Cu_{1.8}Se$ Danilkin found substantial mode softening in $Cu_{1.8}Se$ [44].

damp out the oscillation. Above this frequency the liquid atoms move slow compared to the perturbation and so appear as a solid. As temperature increases more lattice vibration modes and ion hopping modes contribute to this behavior, with their contribution determined by the characteristic quantity. At $k_b T \gg \hbar\omega_D, \hbar\Omega_F$, the heat capacity simplifies to:

$$c_v = k_b \left(3 - \left(\frac{\omega_F}{\omega_D} \right)^3 \right) \tag{6.1}$$

From inelastic neutron scattering measurements, the Frenkel timescale of Cu_2Se is 1 picosecond at 430K [42]. This corresponds to a $c_v = 2.98 k_b$. Though this casts doubts on the explanation of Liu *et al.* [122], this author is unaware of any experiments showing the ion hop time of Cu_2Se at high temperature. One should also not discount the possibility that another material may show liquid-like reduction in its heat capacity much more strongly than Cu_2Se does.

While the liquid-like fluctuations of ions may not eliminate phonon propagation modes, they may scatter them. Ultra-sonic attenuation is a common feature of many solid electrolytes [3]. The theoretical explanations of Aniya for this behavior treats the mobile ions as a liquid free to move through out the lattice and thereby collide with the mobile cores [6]. A treatment of this class of materials that ignores the significant portion of ion life-time spent between interstitial sites [87] may not be able to fully capture their behavior.

6.2 Band Structure Modeling

In order to understand how Ag_2Se may have enhanced thermoelectric performance as compared to predictions based on its band structure, a brief overview of the relationship between band structure and Seebeck coefficient is necessary.

The electronic transport properties of heavily doped thermoelectrics can be typically described by modeling their electronic band structures [180, 127]. If the full electronic band structure is known — or more realistically predicted by density func-
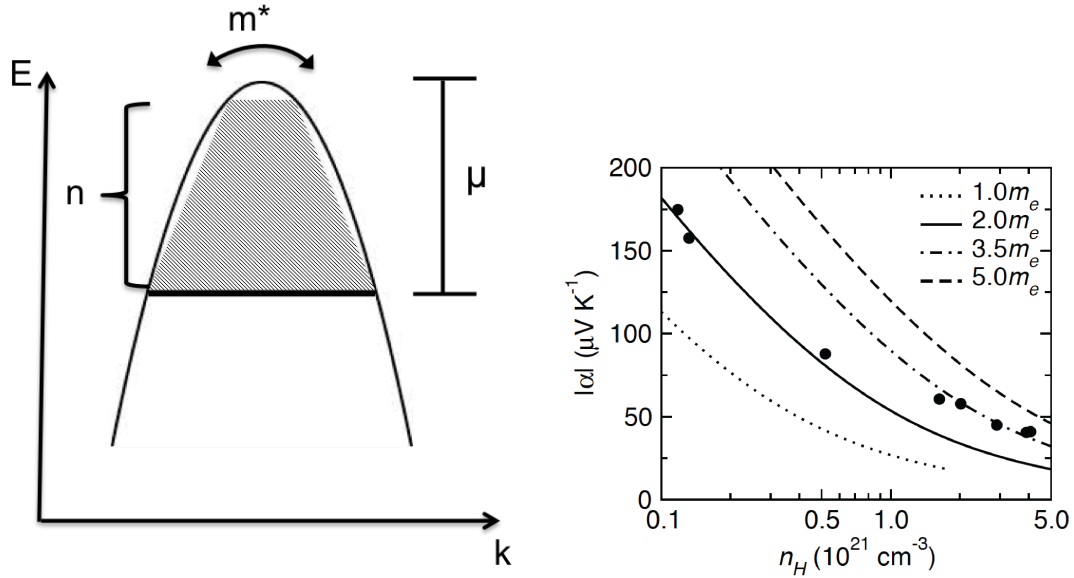
Figure 6.3: Left: Example of a single parabolic band. The band shown is a valence band as for a p-type conductor. The effective mass (m^*) determines the curvature of the band. The carrier concentration is the number of carriers between the band edge and the Fermi level.

Right: Example α versus n_H or *Pisarenko* plot. As m^* increases at constant n_H, α increases.

tional theory — then the transport coefficients could be computationally determined (*e.g.*, by BoltzTRaP [127]). However, simplified models that take into account only part of the band structure are extremely successful at predicting transport properties [154]. These models are successful because only band states within $3k_bT$ of the electron chemical potential (*i.e.*, the Fermi level) contribute significantly to electron transport [128]. The starting point for these models is the single parabolic band [170]. Thermoelectrics are heavily but not metallically doped, so that the band of the dominant conductor tends to dominate, but the Fermi level is not far from the band edge. A single parabolic band (SPB) has a dispersion relationship of form:

$$E = \frac{\hbar^2(k - k_0)^2}{2m^*} \tag{6.2}$$

This structure is shown in Figure 6.3(a). The effective mass (m^*) is typically given in units of electron masses (m_e). A heavier band (large m^*) has a low rate of curvature

of E with respect to k; increasing k increases E only slightly. In a light band (small m^*) increasing k increases E significantly.

If m^* and the band chemical potential (μ) are known, than the carrier concentration may be written as:

$$n = 4\pi \left(\frac{2m^* k_b T}{h^2} \right)^{3/2} F_{1/2}(\eta), \tag{6.3}$$

in which h is Plancks constant, $\eta = \frac{\mu}{k_b T}$ is the *reduced chemical potential* and $F_j(\eta)$ is the Fermi integral of order j.

If the energy dependence of scattering (λ) is also known, than transport variables may be modeled as well. In the case of scattering by acoustic phonons $\lambda = 0$. This is a good assumption for thermoelectric materials above the Debye temperature. In this model the Seebeck coefficient may be expressed as:

$$\alpha = \frac{k_b}{e} \left(\frac{(2+\lambda)F_{\lambda+1}}{(1+\lambda)F_\lambda} - \eta \right) \tag{6.4}$$

The general behavior can be understood well if the degenerate (*e.g.*, metallic) limit of Equation 6.4 is taken.

$$\alpha = \frac{\pi^{8/3} k_b^2}{3qh^2} n^{-2/3} T m^* (1+\lambda) \tag{6.5}$$

The inverse dependence of Seebeck on n argued for generally in the introduction is again present. Notably increased m^* results in increased Seebeck coefficient. This can be explained by a two step argument. A heavy band will have a lower η for the same n compared with a light band. A lower *eta* results in a larger Seebeck coefficient by equation 6.4. This effect is depicted in Figure 6.3(a) by means of a Pisarenko (α versus n or n_H) plot.

6.3 Prior Work on Ag_2Se

As established in Chapter 5 Ag_2Se shows a first order transition at 408 K as seen in both crystallography and calorimetry. Electronically Ag_2Se is a n-type material with high electron mobility and low thermal conductivity. These two attributes in combination give it promise as a high zT material near room temperature [1], but with two principal problems. The first is carrier concentration control, for which there is some uncontrolled effect in synthesis. The sample I will discuss below showed no carrier concentration shift through its phase transition, but many of the samples show a significant shift at that temperature [46]. The Seebeck coefficient of a second sample, produced by a different laboratory, shows the same trend as the sample principally studied here.

The second problem is hysteresis observed in transport properties in the low temperature phase and near the phase transition temperature [2]. These effects may be due to the kinetics of microstructural reorganization, as they appear in multiple materials. One example of this is $Ag_2Se_{0.5}Te_{0.5}$ [50]; other materials showed this effect but these instabilities rendered writing a meaningful publication on their thermoelectric performance impossible. In his paper on Ag_2Se my colleague Tristan Day applied band structure modeling to estimate the effective mass of the low temperature phase $0.2m_e$ and that of the high temperature phase to $0.3m_e$ [46].

6.4 Transport Measurements

Electrical conductivity (Figure 6.4(b)) was measured in the Van der Pauw geometry (see Chapter 2). Substantial hysteresis was observed both in the phase transition temperature and in the data in the low temperature phase. The data above the phase transition temperature is consistent on heating and on cooling. Though the data values on heating and cooling are inconsistent, the shape of the curves shows the same general trend. Above room temperature the conductivity linearly increases with temperature and then flattens out before the phase transition temperature. The
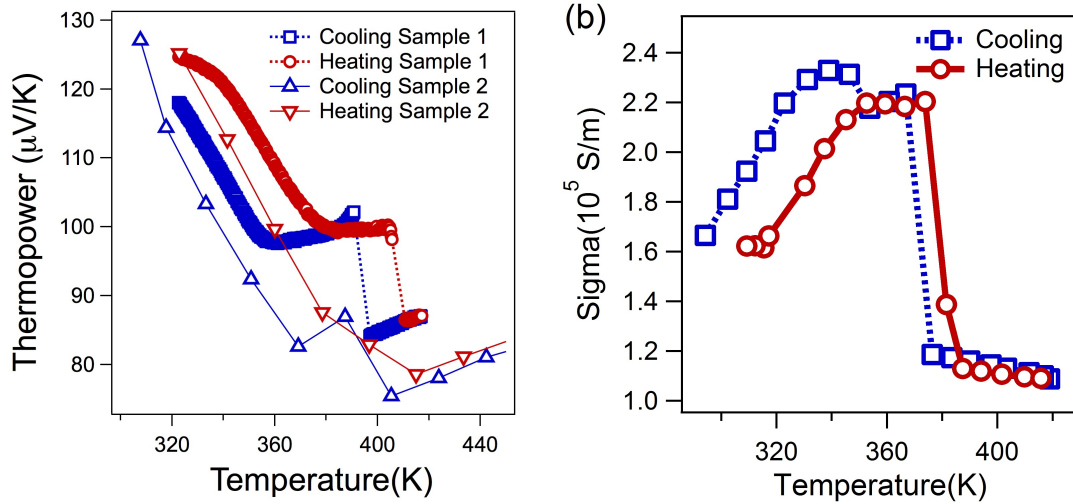
Figure 6.4: Seebeck Coefficient (a) and Electrical Conductivity of Ag$_2$Se measured on both heating and cooling.

conductivity drops by a factor of two at the phase transition temperature.

The Seebeck coefficent (Figure 6.4(a)) was measured by the ramp method discussed in Chapter 3 at 10 Kelvin per minute. It shows a similar behavior to the conductivity. At the temperatures at which the electrical conductivity increases, the Seebeck decreases. At the temperatures at which the electrical conductivity flattens, the Seebeck coefficient flattens. At the phase transitions it decreases slightly. During the phase transition the voltage versus ΔT data could not be fit to a line and so is not shown. The phase transition occurs at 405 K on heating and on 390 K on cooling. This hysteresis is expected for a first order phase transition. A second sample produced in a different lab by Dr. Fivos Drymiotis was measured by the oscillation method and showed a comparable change in the Seebeck coefficient through the phase transition.

The thermal diffusivity (figure 6.5(a) also shows a hysteresis in its phase transition temperature. The thermal diffusivity shows far less consistent behavior on heating and cooling than the electrical properties. In the high temperature phase there is a 10% discrepancy between the heating and cooling data. The phase transition range is extended on cooling over a 15 K range. The low temperature data shows a more significant discrepancy between the heating and cooling data.
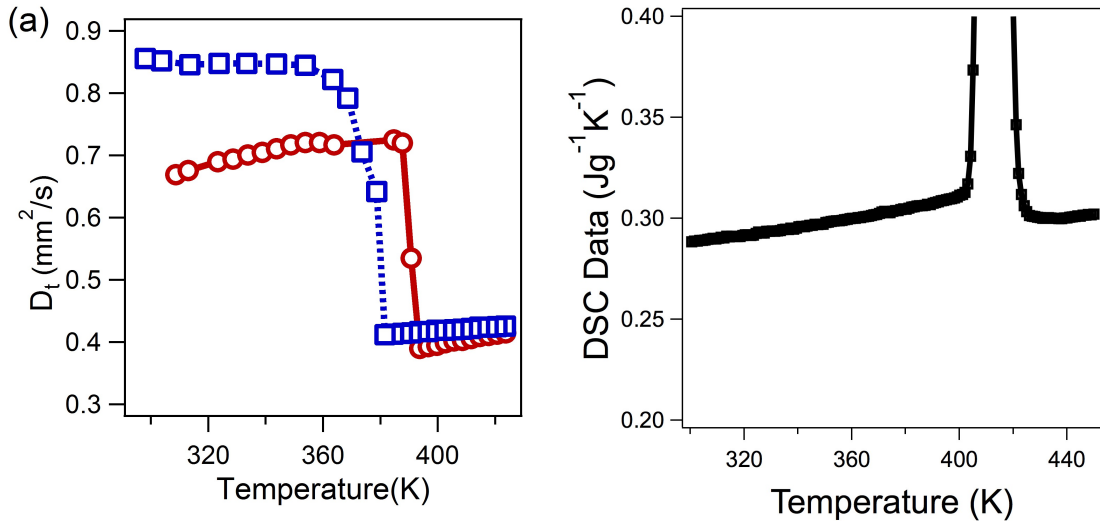
Figure 6.5: Thermal diffusivity (a) and Calorimetry data (b) for Ag_2Se measured on both heating and cooling.

In the context of identification of the order of the phase transition, the calorimetry was also discussed in Chapter 5.2 As Ag2Se has a first order phase transition, the peak in its calorimetry at 410 K represents an enthalpy of formation. At temperatures further below 400 K and above 420 K it is an accurate measurement of the heat capacity, and is used to calculate κ and zT. Between 400 K and 420 K the heat capacity used is that measured at 400 K — 0.317 J/gK.
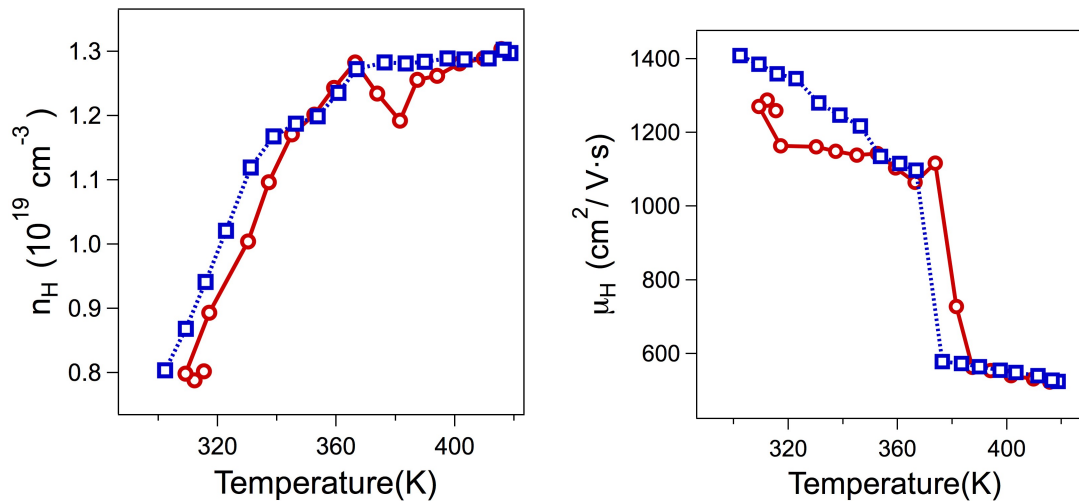
Figure 6.6: Hall Carrier Concencentration (a) and Hall Mobility (b) for Ag_2Se measured on both heating and cooling.

The Hall coefficient was measured concurrently with the electrical conductivity via the Van der Pauw method at 2 Tesla. The Hall carrier concentration (Figure 6.6(a)) and Hall mobility (Figure 6.6(b)) were thereby determined on heating and cooling. The Hall carrier concentration of Ag_2Se varies smoothly through the phase transition. This suggests that the band curvature (*i.e.*, effective mass) and the doping level are not altered measurably by the structural changes of the phase transition. The Hall mobility decreases by 50% through the phase transition. This is consistent with a sudden increase in the ion disorder and conductivity leading to increased scattering of electrons. It also explains the decrease in electrical conductivity observed at the phase transition temperature. Pardee and Mahan suggested that a steady Arrhenius increase in ion conductivity is observed due to Frenkel defect formation in both type I and type II super-ionics [151]. Such defect formation in Ag_2Se may alter the carrier concentration by localizing electrons more or less than the ground state sites. This would be indicated by a difference in Ag ion effective valency.

Below 360 K, the cooling Hall carrier concentration increases steadily with temperature; over the same range Seebeck decreases steadily. As the Hall carrier concentration become constant, so does the Seebeck coefficient. The data was of insufficient quality to prove this connection as causal. The Seebeck coefficient shows a 15% decrease from the low temperature to the high temperature phase, despite no measured shift in the carrier concentration. This data is inconsistent with the band model advanced in equation 6.5.

The total thermal conductivity of Ag_2Se is decreased by a factor of two in the disordered high temperature phase as compared to the ordered low temperature phase, see Figure 6.7(a). The Lorenz number of $L = 1.8 \times 10^{-8}$ $W\Omega K^{-2}$ was used to calculate the electronic portion of the thermal conductivity. This quantity is taken from Day *et. al*'s [46] single parabolic band model of data from their samples and literature samples. From this Lorenz number κ_e and κ_L may be calculated. The lattice thermal conductivity of Ag_2Se decreases only slightly as the temperature increases through the phase transition temperature, indicating that the majority of the change in total thermal conductivity is due to the decrease in electrical conductivity, see Figure 6.7(a).
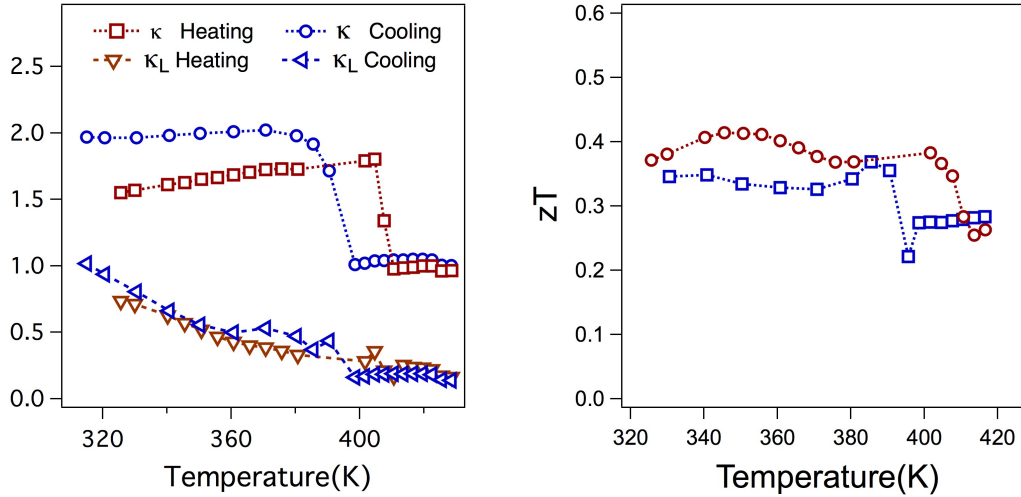
Figure 6.7: Left: Measured total and modeled lattice thermal conductivity of Ag$_2$Se. Right: zT of Ag$_2$Se. The zT in the ordered phase is markedly higher than the zT in the disordered phase.

The resulting lattice thermal conductivity is 0.35 W/mK below the phase transition temperature and 0.25 W/mK above it. This indicates that the Lorenz number of Day *et. al* is correct.

From the transport data presented above, the zT of Ag$_2$Se was determined on both heating and cooling, see Figure 6.7(b) Where necessary corrections to the temperature were made to align the phase transitions of all transport properties. In the calculated range between 320 K and 420 K zT is bound between 0.3 and 0.4, and it decreased upon transition to the disordered phase. The decrease in zT is 30%, which is consistent with the anomalous 15% decrease in the Seebeck coefficient at the phase transition temperature as zT varies with Seebeck squared. What explains this anomalous enhancement in Seebeck and zT?

One possible explanation would be a decrease in m^* from the ordered to the disordered phase. By equation 6.5 decreasing m^* should result in a decreased Seebeck coefficient. However, the band structure model of Day *et al.* suggests a moderate *increase* in m^* from the ordered to the disordered phase, see Figure 6.8(b). Such an increase is not compatible with the observed decrease in Seebeck coefficient. Day *et. al* suggest that the increase is from 0.2m$_e$ to 0.3m$_e$, but the error bars on their fit are
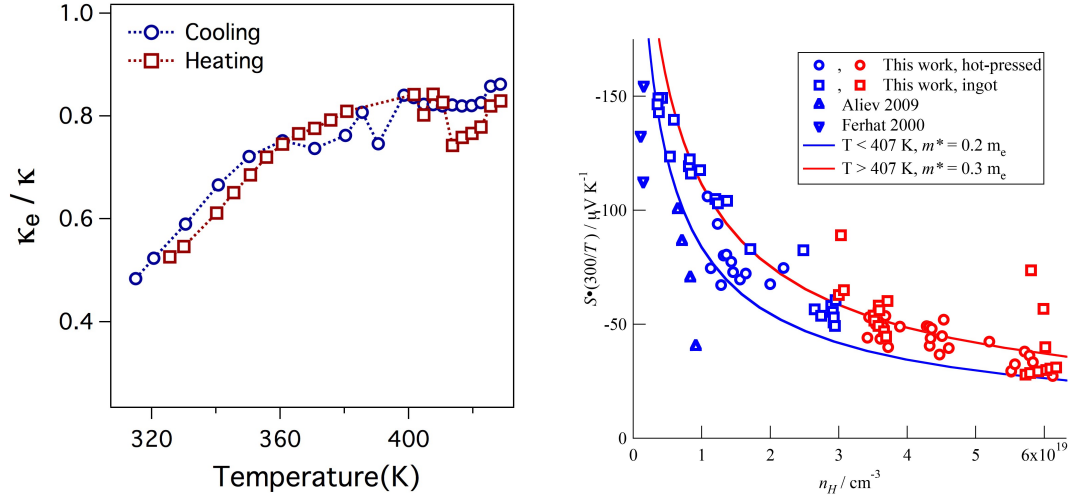
Figure 6.8: The ratio (a) of κ_E to κ is nearly identical on either side of the phase transition.
Pisarenko plot (b) for Ag$_2$Se. The disorder phase has a slightly larger m^* than the ordered phase. Modified version of Figure 2a in Day*et al.* [46] Courtesy of Tristan Day

such that the increase may be much smaller even than that.

Thermoelectric performance can also improve a more favorable portion of thermal transport due to electrons rather than the lattice; this is certainly possible given the decrease in κ_L observed, see Figure 6.7(a). The formula for $zT = \sigma\alpha^2/\kappa T$ can be reformulated in terms of L and κ_e as:

$$zT = \frac{\alpha^2}{L}\frac{\kappa_e}{\kappa} \tag{6.6}$$

With the contribution due to α discussed above and L varying significantly only for large changes in the Fermi level, the remaining contribution can be expressed as $\frac{\kappa_e}{\kappa}$. This term varies by less than 5% through the phase transition temperature, see Figure 6.8(a). This indicates that the enhancement in zT is entirely due to the enhancement in α noted above.

The enhancement in zT and α requires an alternate explanation from the single parabolic band model. More complex band effects such as band convergence [153] or resonant impurities [77] might be considered to explain the behavior. However,

these features are inconsistent with the constant n_H observed and the near constant m^* [154]. This suggests that an alternate explanation for the Seebeck and zT enhancement is required. This explanation must in some way be beyond that which even complex band structure modeling can capture. Over the next two chapters I will develop that explanation: co-transport of entropy associated with the order process leads to enhanced Seebeck and zT.

Chapter 7

Transport in Cu_2Se and $Cu_{1.97}Ag_{0.03}Se$

In the previous chapter I introduced super-ionic materials and band structure modeling of thermoelectrics. In that context I introduced the thermoelectric super-ionic material Ag_2Se, and in analyzing its transport I noted an increase in its Seebeck in its ordered phase compared to its disordered phase that appeared directly responsible for an increase in its thermoelectric performance. This change in its Seebeck coefficient was not explained with the band structure models typically used to explain thermoelectric transport.

In this chapter I will discuss Cu_2Se, which also shows an unexplained increased in its Seebeck and zT at its phase transition. In chapter 5 I noted that Cu_2Se shows a second order transition while Ag_2Se shows a first order transition. Its phase transition thermoelectric behavior reflects that characteristic. Before I discuss the transport behavior of Cu_2Se and $Cu_{1.97}Ag_{0.03}Se$ I will introduce the concept of coupled entropy transport; this concept can be used to explain the behavior of these materials which will be done in detail in the concluding chapter.

7.1 Entropy and Charge Transport

A thermoelectric material is treated as a having two principle interacting thermodynamic quantities: heat and electron current [31]. The equilibrium thermodynamics

of such a system are described by:

$$dS = \frac{1}{T}dU - \frac{\tilde{\mu}}{T}dN, \tag{7.1}$$

in which S and U are the entropy and internal energy of the system and N is the number of particles (carriers). Though I will address this part of my analysis in terms of these extensive quantities, it is often convenient to use the corresponding intensive quantities of entropy density (s), energy density u, and carrier concentration (n). Conversion from extensive to intensive quantities in these formulations is simply a matter of substituting the intensive variable for an extensive variable.

The nature of an irreversible process is that it produces entropy. A thermodynamic formulation in which the extensible quantities are expressed as differentials, as in Equation 7.1, will have a simple equivalent in irreversible thermodynamics. The entropy production associated with a linear process is: Equation 7.1 is [32]:

$$\dot{S} = \nabla \frac{1}{T} \cdot J_U - \nabla \frac{\tilde{\mu}}{T} \cdot J_N, \tag{7.2}$$

in which the J_x are thermodynamic fluxes and the gradient terms are thermodynamic affinities. Under a given set of boundary condition, *i.e.*, a particular resistor acting as a load and under steady state, the systems properties will be arranged such that $\dot{S}$ is minimized. This theoretical result is known as the minimum entropy principle. Of course $\dot{S}$ is always greater than or equal to zero, or else the second law of thermodynamics would be violated. The ratio of the second term in Equation 7.2 to its first terms describes the reversibility of the heat engine. When the load is varied to maximize that ratio, that maximal value is zT.

On the micro-foundation of the fluctuation-dissipation theorem Onsager proved that thermodynamics forces and fluxes associated in entropy production could be related linearly [147]. Generally:

$$\begin{bmatrix} J_1 \\ J_2 \end{bmatrix} = - \begin{bmatrix} L_{11} & L_{12} \\ L_{21} & L_{22} \end{bmatrix} \begin{bmatrix} \nabla X_1 \\ \nabla X_2 \end{bmatrix}] \tag{7.3}$$

The L_xy are known as the Onsager coefficients and they may depend on any set of thermodynamic quantities that describe the system. By the Onsager reciprocity theorem $L_{12} = L_{21}$. For the specific case of thermoelectricity:

$$\begin{bmatrix} J \\ J_S \end{bmatrix} = - \begin{bmatrix} L_{ee} & L_{es} \\ L_{se} & L_{ss} \end{bmatrix} \begin{bmatrix} \nabla V \\ \nabla T \end{bmatrix} \tag{7.4}$$

Here I use entropy transport instead of heat transport to avoid the confusion between the two different definitions of heat flux commonly used [49]. The Callen heat flux $Q \equiv TJ_s$ describes the heat transport through the material, while the DeGroot heat flux $J_q \equiv\equiv \mu J_e + TJ_s$ decribes that transporting from one heat reservoir to another [132] In the case of thermoelectrics that distinction does not lead to any difference in description of the Onsager coefficients [49].

The Onsager coefficients may be related to σ,α, and κ by:

$$\alpha = -\frac{L_{es}}{L_{ee}} \tag{7.5}$$

$$\sigma = L_{ee} \tag{7.6}$$

$$\kappa = T \left(\frac{L_{ee}L_{ss}L_{es}^2}{L_{ee}} \right) \tag{7.7}$$

While ideal for describing the macroscopic relations between the phenomenological transport coefficients, the irreversible thermodynamics of the Onsager relations cannot actually produce the values of those coefficients. The kinetic theory approach is therefore preferred for understanding how chemical sturcture, bands structure, and doping give the values of these coefficients. For this the Boltzmann transport equation is used:

$$\frac{\partial f}{\partial T} = \left(\frac{\partial f}{\partial T} \right)_{force} + \left(\frac{\partial f}{\partial T} \right)_{diff} + \left(\frac{\partial f}{\partial T} \right)_{coll} \tag{7.8}$$

Here f is the electron state occupation probability density. When eq (7.8) is solved

it will generally have the form given by Kubo [112, 113]:

$$q\alpha = -\frac{\mu}{T} - k_b T \frac{M_{qe}}{M_{ee}} \tag{7.9}$$

M_{qe} and M_{ee} are transport integrals representing heat transport per electron and current transported per electron. A comparable expression may be derived from only non-equilibrium thermodynamics considerations [49].

$$\alpha \equiv \frac{-\mu}{T} + \frac{1}{qT} J_q \tag{7.10}$$

From comparison with Equation 7.10, we see that Equation 7.9 is actually the sum of two separate thermodynamic transport quantities. The first term represents the entropy transport due to the change in the number of carrier present. It is the thermodynamic equivalent of heat transport by mass flow in a liquid-based heat exchanger. Following Emin [61], we refer to the first term as the presence Seebeck, $\alpha_{presence}$. The presence Seebeck is convenient to work with because it can be expressed entirely in terms of equilibrium thermodynamics:

$$\alpha_{presence} \equiv -\frac{\mu}{qT} \equiv \frac{1}{q} \left(\frac{\partial S}{\partial n} \right)_U \tag{7.11}$$

The second term in Equations 7.9,7.10 represents the part of the Seebeck that results from the manner in which charge is transported. It reflects contribution from the scattering interaction of the moving heat and charge and the distortion transport effects on the state occupations and energies. For this reason, again following Emin, we refer to it as the transport portion of Seebeck, $\alpha_{transport}$.[61] Solving for $\alpha_{transport}$ exactly would require a perfect understanding of all electron scattering mechanisms and the band structure, and its determination is the primary focus of band structure modeling.

7.2 Entropy Co-Transport

In the discussion in section 7.1 above we implicitly assumed that the only thermodynamic quantities that transported were charge and entropy. While the formulations of eqs.7.4,7.9 are completely phenomenological and general, calculating the Onsager coefficients under this assumption will lead to a discrepancy with measurement. The entropy associated with co-transport of the non-electronic thermodynamic flux will be attribute to $\alpha_{transport}$; however, the transport calculations based on a static band structure will be unable to replicate that effect.

To include the effect of another thermodynamic variable, I first add an additional term to equation 7.1.

$$dS = \frac{1}{T}dU - \frac{\tilde{\mu}}{T}dN + hdm \qquad (7.12)$$

There will be a thermodynamic flux (J_m) associated with m and a thermodynamic force (∇h) associated with h. If a flux of electrons drags a flux of m, then that the entropy transported per carrier should be enhanced by the presence entropy of those units of m. The presence entropy is then:

$$\alpha_{presence} = \frac{1}{q}\left(\frac{\partial S}{\partial n}\right)_U + \frac{1}{q}\left(\frac{\partial S}{\partial m}\right)_{U,N}\left(\frac{\partial m}{\partial n}\right)_{U,S} \qquad (7.13)$$

In chapter 8 this relation will be motivated from non-equilibrium thermodynamics.

Entropy co-transport enhancements to Seebeck and zT have been observed in several material systems. Aselage *et. al* [7] determined $B_{12+x}C_{3-x}4$, $0.15 < x < 1.7$ to have a Seebeck coefficient of $\approx 200\mu V/K$ despite a carrier concentration of $\approx 10^{21}\,cm^{-3}$. A Seebeck coefficient of $10\,\mu V/K$ would be expected at such a high carrier concentration. In this material carriers transport as polarizable pairs, called *bipolarons*. The presence of these bipolarons modifies by a dipole interaction atomic vibrational frequencies [62]. By modeling the entropy contribution associated with this bipolaron mode softening, Emin was able to explain the behavior of these Boron Carbides as due to phonon entropy co-transport [61] Such vibrational softening enhancements of Seebeck are referred to as phonon drag Seebeck effects, and they have

been observed in other systems [39, 11, 10].

By coupling the spin degree of freedom to entropy transport, increased Seebeck in Na_xCoO_2 has been shown [196, 110, 139]. The differing spin degeneracy of electron-occupied and electron-unoccupied cobalt sites provides the mechanism for this coupling of carrier transport to entropy transport [138]. Here we consider coupling the carrier transport to degrees of freedom associated with the structural changes of a phase transition. A phase transition is always associated with an entropy change because there is always a concurrent transformation in system symmetries [162]. In continuous (*i.e.*, second order) phase transitions the entropy will change over an extended temperature range. In chapter 5, we found the phase transition of Cu_2Se to have a substantially elevated heat capacity over a wide temperature range. If some part of the entropy associated with the phase transition is coupled to transport, a large Seebeck enhancement may be possible.

7.3 Cu_2Se Transport near the Phase Transition

Copper (I) selenide is a p-type semiconductor [54]. Above 410 K Cu_2Se becomes super-ionic, which is characterized by its disordered Cu^+ ions, and shows good thermoelectric properties [122]. Except at the highest temperatures, charge transport is dominated by holes rather than Cu^+ ions. As the temperature drops below 410 K the ion mobility decreases [84] and eventually the Cu ions become ordered [96]. It is known that copper (I) selenide can be copper deficient ($Cu_{2-\delta}Se$) with copper vacancies, and this has a large effect on transport properties and the phase structure [194].

Horvatic *et al.* showed that the ion conductivity of $Cu_{1.99}Ses$ increases from 1 S/m at 374 K to almost 100 S/m at 410 K [84], demonstrating it to have a super-ionic phase transition. Below 374 K and above 410 K, he found that the ion conductivity followed an Arrhenius law with $E_A = 0.29\,eV$ and $E_A = 0.07\,eV$, respectively. Each of these temperatures had been previously identified as corresponding to a phase transition in $Cu_{2-\delta}Se$ ($\delta < 0.045$) [194, 177]. In the intermediate temperature range, the ion conductivity changed rapidly. This behavior is indicative of a continuous phase
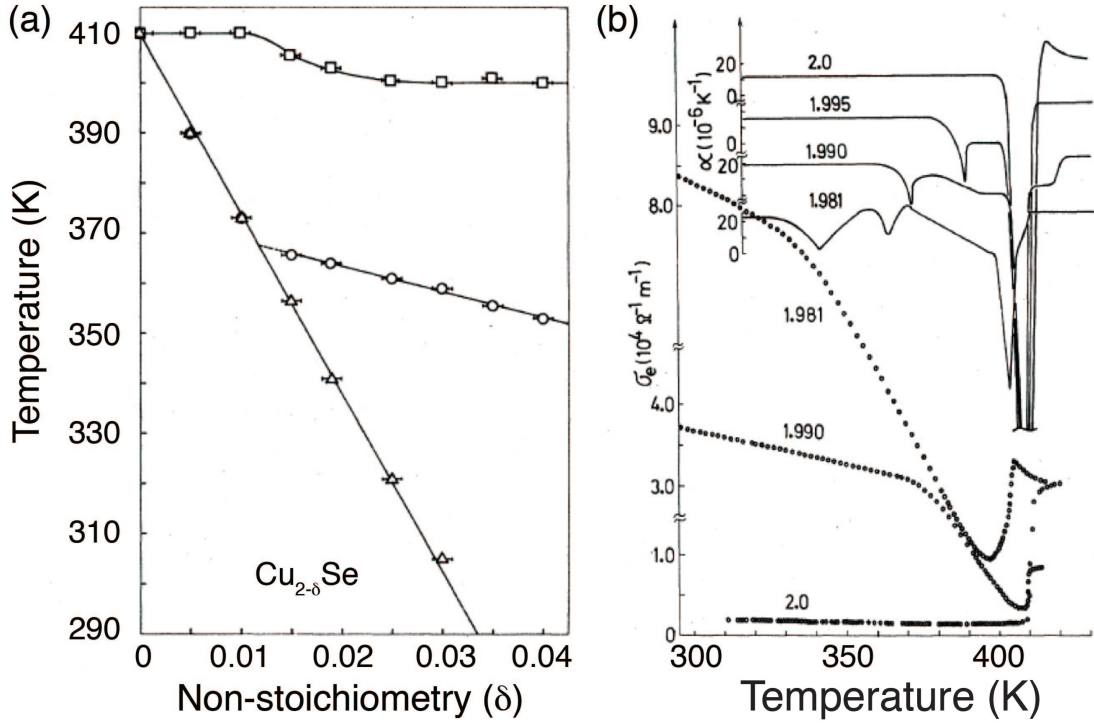
Figure 7.1: Phase diagram (a) determined by Vucic [194] on the basis of dilatometry (b) measurements. Adapted from Vucic *et al.* [192].

transition in a super-ionic material [21, 118]. An observation of not only structural entropy change at the phase transition but also of structural entropy transport is given by Korzhuev and Laptev [107]; they measured a sharp peak in the thermodiffusion of Cu^0 in Cu_2Se at the 410 K phase transition. From this they calculated a heat of transport of Cu atoms of 1 eV.

Unusual transport effects have been observed before near the critical temperature in Cu_2Se [54, 122, 143, 144, 123, 200, 27], however, this is the first work that also considers changes in all thermal transport measurements (D_t, κ, c_p) to derive an improved value for zT. Liu *et al.* report a zT greater than 1 [121], however their work assumes all the heat released as measured by DSC is due to a first order structural transformation. In that case it would be appropriate, as is done by Liu et. al., to calculate κ and zT using the smaller Delong-Petit heat capacity. As discussed in detail in chapter 5 the elevated peak in calorimetry is an equilibrium rather than kinetic aspect of the system behavior and must be used to determine zT.
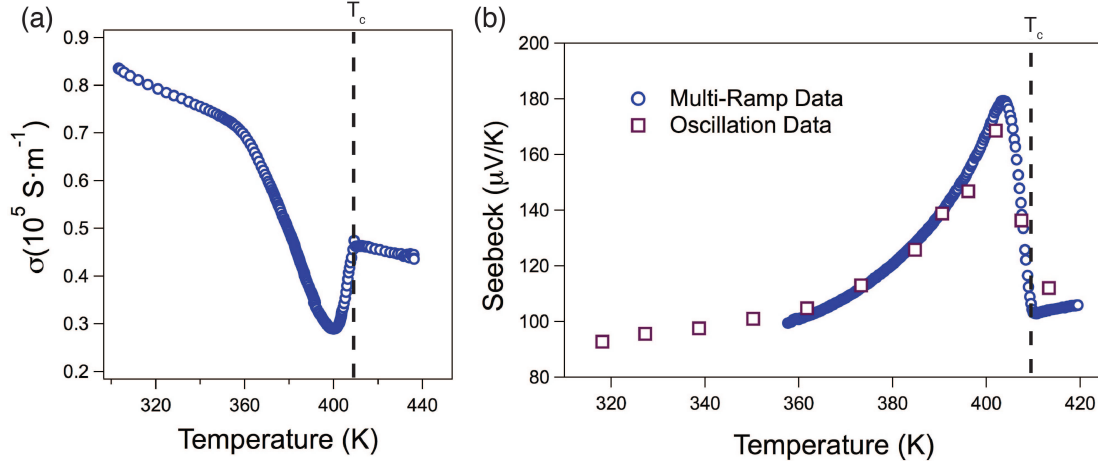
Figure 7.2: Electrical conductivity (a) and Seebeck Coefficient (b) measured through the $410K$ phase transition.

The study of electrical transport near the phase transition of $Cu_{2-\delta}Se$ owes mostly to the work of Zlatko Vucic and his collaborators at the University of Zagreb [84, 194, 192, 191, 134, 193]. His measurements spanned the $\delta = 0$ to $\delta = 0.045$ single phase range [106]. Based on dilatometric measurements he developed a phase diagram for $Cu_{2-\delta}Se$, see Figure 7.1. At all compositions he found a phase transition at ≈ 410 K and a second phase transition at a lower temperature with temperature dependent on δ. The data presented on the sample of Cu_2Se presented here corresponds generally to his observations of his $\delta = 0.01$ sample. WDS data on Cu_2Se bounded $\delta < 0.005$ for this sample; the reason for this disagreement is unclear.

Electrical conductivity (Figure 7.2(a)) was measured at a heating rate of 10 K/hr. It shows three main features: a knee at 355 K, a minimum at 400 K, and a kink at 410 K. The kink at 410 K corresponds to the observed phase transition in my crystallography data (section 5.3). In general shape $\sigma(T)$ strongly resembles the data in Vucic's studies(Figure 7.1), though it corresponds best to his $Cu_{1.99}Se$ stoichiometric sample.

The knee in conductivity at $T_{c2} = 355\,K$ corresponds to the lower temperature second order phase transition measured by Vucic [192]. He empirically determined a

power law for σ below T_{c2}:

$$\sigma = \sigma_0 \left(1 - \frac{T}{T_{c2}} \right) \tag{7.14}$$

From the low temperature slope a predicted $T_c = 360\,\text{K}$ was determined, which is consistent with the T_{c2} determined by inspection. Above the phase transition the conductivity is again linear, though 20% lower than the value predicted by extrapolation from the low temperature behavior.

Seebeck was measured first by the standard oscillation method as described in chapter 3, see Figure 7.2(b). This showed a clear peak in the Seebeck, but the rapid non-linear change raised clear questions about the accuracy of those results. For this reason the ramp Seebeck approach was developed as described in chapter 3, allowing for detail temperature-resolved measurement of Seebeck through the phase transition. The three significant features observed in σ are echoed in α. There is a kink in the Seebeck at 410 K, corresponding to the main phase transition observed in crystallography. Below 360 K α is a linear function of temperature; above it shows non-linear behavior. There is a maxima in α at 403 K, at a slightly elevated temperature compared to the 400 K minima in electrical conductivity. Above the phase transition the Seebeck is locally linear, though 10% lower than the value predicted by extension of the low temperature trend.

Thermal conductivity was calculated from measurements of density(ρ), DSC heat capacity (C_p) and laser flash diffusivity (D_T) as detailed in chapter 2. Density was measured to be $6.7\,\text{g/cm}^3$ by geometric calculation and confirmed by principle of Archimedes. Thermal diffusivity decreases linearly from 300 K to 360 K, see Figure 7.3(a). From 360 K to 410 K the thermal diffusivity shows an excellent fit to a critical power law with $T_c = 410\,\text{K}$ and critical exponent $r = 0.80$. Above the 410 K phase transition the thermal diffusivity is again changes only in a steady linear fashion with temperature.

Heat capacity is presented here in Figure 7.3(b), but it was discussed in great detail in section 5.3. Below 360 K and above 425 K the heat capacity gives a baseline value of $0.374\,\text{J} \cdot \text{g}^{-1}\text{K}^{-1}$, consistent with the Dulong-Petit c_p for Cu_2Se, $0.361\,\text{J} \cdot \text{g}_{-1}\text{K}_{-1}$.
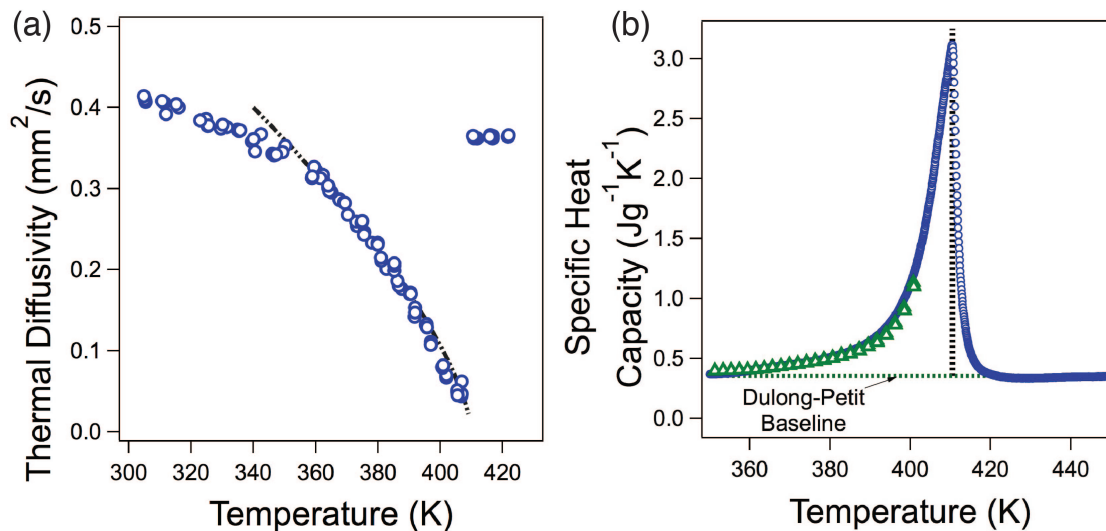
Figure 7.3: Thermal diffusivity (a) and specific heat capacity (b) for Cu_2Se from its room temperature through its $410K$ phase transition

The 60 K breadth of the peak is indicative of the continuous nature of the transition. In the transition region there is a lambda-type peak, as is characteristic of continuous phase transitions in ionic conductors [118].

From the transport properties described above, zT was calculated. (Figure 7.4). zT doubles over a 30 K range peaking at 0.7 at 406 K. Though strong non-linearity in each of the individual transport variables onsets at 360 K, there is no non-linear in zT until 390 K. This suggests that more than different effects — perhaps associated with the multiple Cu_2Se phase transitions — are needed to explain the anomalous transport behavior between 360 K and 410 K.

7.3.1 Analysis

Excepting the region of elevated zT (390 K to 410 K) all the observed variation in transport can be explained by a simple band structure model. From knowledge of the band structure, the energy dependence of scattering, and the reduced chemical potential, all thermoelectric transport properties can be modeled for typical systems. Though η cannot be easily measured, it can be inferred from the Seebeck coefficient from Equation 6.3. In the degenerate (metallic) limit this dependence can be
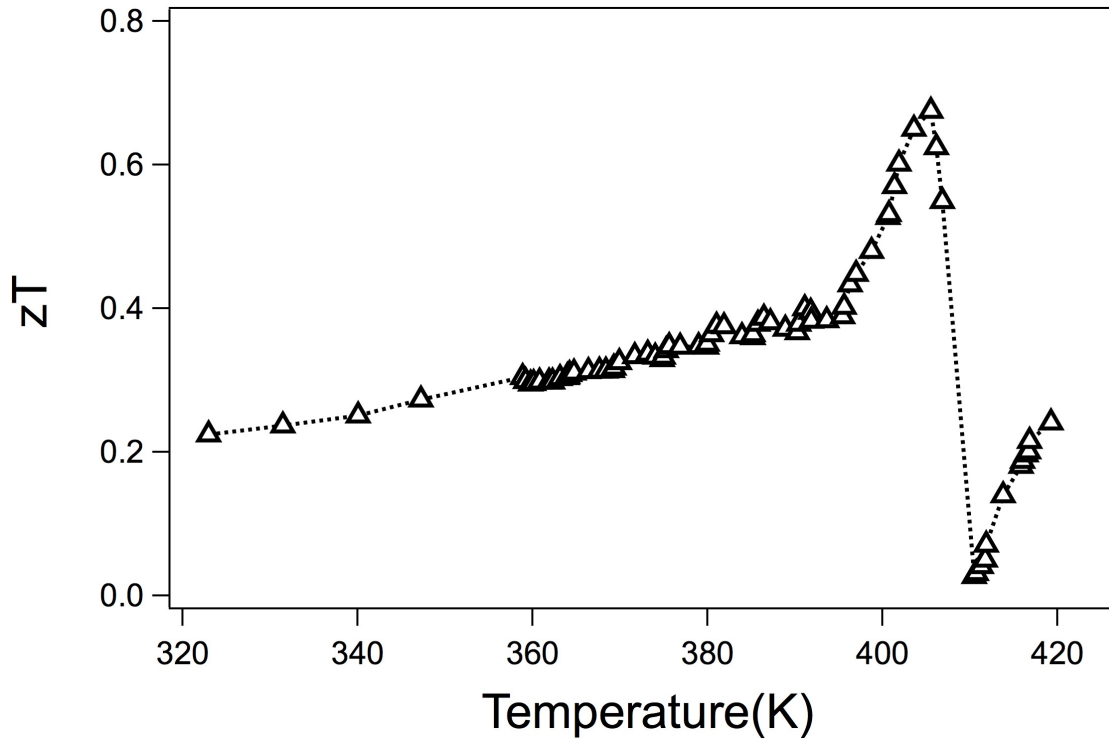
Figure 7.4: zT for Cu$_2$Se from its room temperature through its 410 K phase transition.
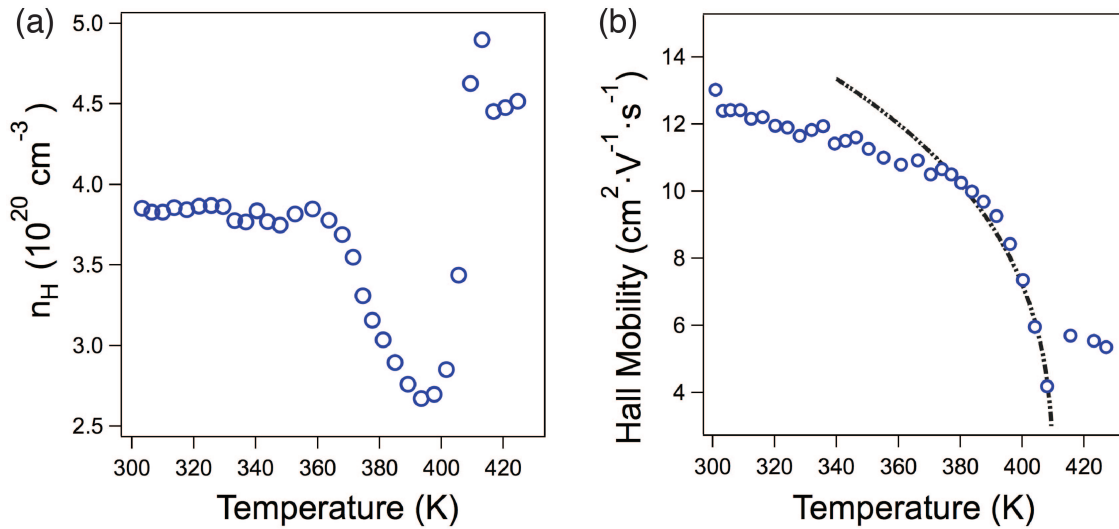
Figure 7.5: Hall Carrier Concencentration (a) and Hall Mobility (b) of Cu$_2$Se. The minimum of n_H is at 390 K, while μ_H decreases until 410 K. μ_H could be fit to a power law with critical exponent r $= 0.32$

expressed in a simple closed form:

$$n = 4\pi \left(\frac{2m^*kT}{h^2}\right)^{3/2} F_{1/2} \tag{7.15}$$

The Hall coefficient (R_H) and electrical conductivity were measured via the Van der Pauw method using a 1 Tesla magnetic field at the NASA-JPL thermoelectrics laboratory. From these measurements n_H and the Hall carrier mobility were extracted, see Figure 7.5. From 300 K to 360 K n_H is constant while μ_H steadily decreases. The linear decrease in σ (Figure 7.2a) observed is entirely due to a decrease in mobility. Given the association with the copper disordering phase transition, it is possible that a scattering mode like the dumb-bell mode of Zn_4Sb_3 is steadily activated in this temperature range [173]. Between 360 K and 410 K, the Hall carrier concentration dips until it reaches a minimum of $2.7 \times 10^{20}\,\mathrm{cm}^{-3}$. This minimum occurs at 393 K, 10 K lower than the minimum in electrical conductivity and the maxima in Seebeck coefficient. This minima is also very close in temperature to where the zT shows its non-linear increase in temperature, suggesting that the mechanism that causes the increase in zT also cause the change in trend of n_H. During this temperature range μ_H could be fit to a power law with critical exponent r = 0.32. The Hall mobility remains low in the high temperature phase — the mobility is 30% below the value expected from extrapolation of low temperature behavior. This is unsurprising given the phonon softening observed in the structurally identical room temperature $Cu_{1.8}Se$ [44].

Equation 7.15 suggests that three factors may cause an anomalous increase in the Seebeck coefficient: a decrease in the carrier concentration (n_H), an increase in the scattering parameter (λ), or an increase in the band effective mass (m^*). An increase λ is unlikely. The structural delocalization as presented in our p.d.f. data in section 5.3 may lead to an increase in the intensity of acoustic phonon scattering, but it will not alter that effect's energy dependence. Near a phase transition a low frequency optical phonon mode — a *Goldstone* mode — may be present. However, the energy dependence of optical phonon scattering via lattice deformation is the
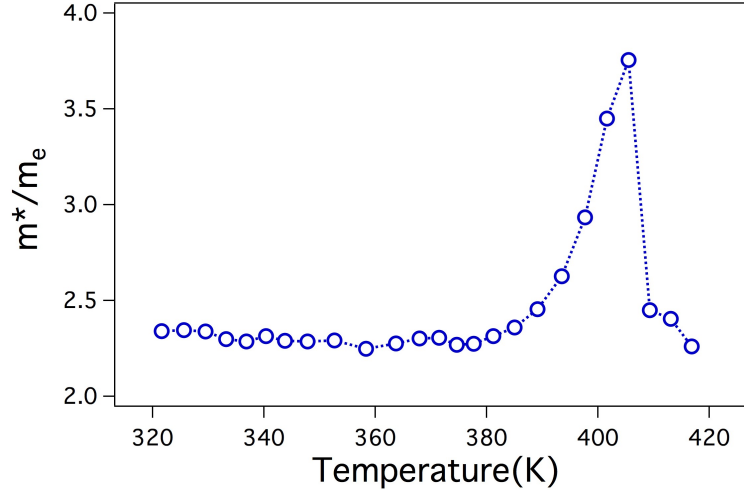
Figure 7.6: Band effective mass need to explain the n_H and α data for Cu_2Se. The transient 50% increase in m^* needed to explain the data is inconsistent with the continuous transformation observed in crystallography.

same as that for electrons and the dependence via dipole effects is only slightly larger than that for acoustic phonons [8].

By modeling with a single parabolic band using measured values of temperature, Seebeck, and n_H, the shift in m^* required to explain the data can be calculated, see Figure 7.6. Up to 380K the data can be explained entirely with a SPB with m* $= 2.3\,m_e$ ($\pm 5\%$). Above this temperature an increase in m^* of up to 50% is required followed by an even more sudden decrease. This is physically inconsistent with the continuous transformation observed via crystallography, see section 5.3. Effective mass can be related to the band structure at the Fermi level by the formula:

$$m^* = \hbar^2 \left(\frac{\partial^2 E}{\partial k^2} \right)^{-1} \tag{7.16}$$

Equation 7.16 means that a substantial change in m^* requires a substantial change in the reciprocal space band structure. As the reciprocal space band structure is related by Fourier transformation to the physical spatial representation of the atomic orbitals and thus the coordination of the atoms. A substantial change in m^* would therefore require a significant change in local electron coordination — a change that is inconsistent with the minor change in band structure seen in temperature-resolve
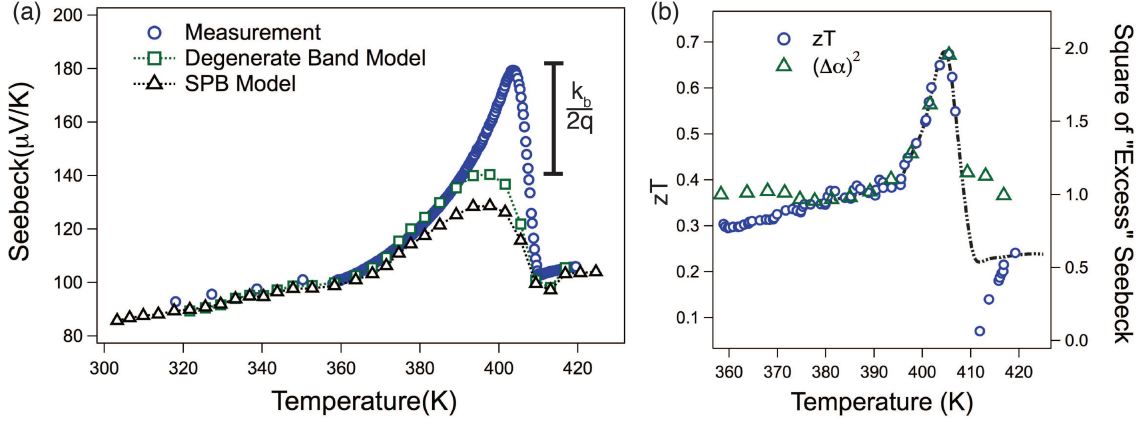
Figure 7.7: Measured Seebeck coefficient compared with predictions from band structure model with $m^* = 2.3\,m_e$ and measured n_H (a). The square of the Seebeck excess to the band structure prediction (b) explains the zT peaks size and breadth.

PXRD. It would further require this change to be transient, existing only in proximity to the 410 K. However, the electron bands are dependent on the average structure rather than the correlation length of the order parameter. Thus we expect the effective mass and other band structure attributes should vary smoothly from one phase to the other, rather than peaking at the phase transition.

While the observed shift in carrier concentration cannot explain the peak in Seebeck, it does elucidate one apparent anomaly in the transport data. As discussed in the previous section the onset of non-linear transport behavior occurs at 360 K, but the zT shows a visible deviation from a linear trend only at 393 K. In Figure 7.6 it is seen that deviation from a constant m^* begins at 380 K to 385 K. The measured Seebeck coefficient and that predicted by Equation 6.5 and a single parabolic band model with $m^* = 2.3\,m_e$ are compared in Figure 7.7. Near 385 K both models show a increasing deviation from the measured data. This increase is of order of the natural scale of Seebeck, $k_b/2q = 43\,\mu V/K$; the increase corresponds to transport of the entropy of an additional degree of freedom per electron.

When the square of the measured Seebeck divided by the band structure predicted Seebeck is compared with zT, as in Figure 7.7b, it is seen that the anomalous increase in Seebeck almost explains the observed breadth and height of the zT peak. The measured Seebeck is 48% higher than the prediction of the SPB model and 40% higher

than the prediction of the degenerate band model at the temperature of peak zT, 406 K. The measured zT is 60% higher at its 406 K peak compared to linear extrapolation from its increase from 360 K to 385 K. The excess Seebeck ($\Delta\alpha$) compared to the band structure slightly overestimates the height of the zT peak. Both the zT and $\Delta\alpha$ are increased noticeably over the exact same temperature range of 393 K to 410 K. This suggests that some aspect of the lambda-type phase transition is increasing the zT of Cu$_2$Se.
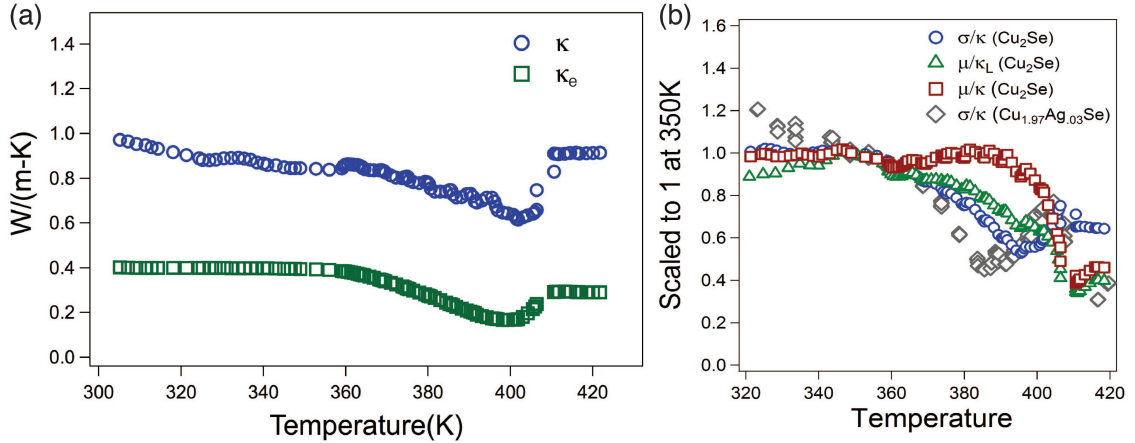
Figure 7.8: Decreasing thermal conductivity does not cause the zT peak. (a) The decrease in κ is due to the electronic contribution (κ_e). (b) Electrical properties decrease slower than thermal properties in the phase transition region and thereby diminish the zT peak.

The zT increase cannot be explained by a relative improvement of phonon to electron scattering; that is by the σ/κ contribution to zT. While there is insufficient data to truly determine the Lorenz number (L) over the entire phase transition region, single temperature estimates bound it between 1.8 and 2.0 WΩ^{-1}K^2. This allows estimation of κ_e by the formula, $\kappa_e = L\sigma T$. The estimated electronic portion of the thermal conductivity qualitatively explains the observed decrease in total thermal conductivity, see Figure 7.8(a).

Direct comparison of electron (μ_H,σ) and thermal transport (κ,κ_L) indicates that the zT is not increased by preferential scattering of phonons over electrons, see Figure 7.8(b). Though thermal conductivity decreases between 360 K and 410 K, this decrease is more than counteracted by a decrease in electrical mobility over the same

range. The observed increase in zT is not due to the reduction of the thermal conductivity via preferential scattering of phonons over electrons. This trend is particularly clear when comparison is made with κ_L instead of κ. This suggests that across the entire temperature range κ_L is close to its glass-like minima, such that further increased scattering from thermally activated modes associated with ion disordering cannot reduce it significantly further. This contradicts the proposal of Liu *et al.* that the increase in zT is due to preferential scattering of phonons as compared to electrons due to interaction with a soft optical (Goldstone) mode [123].
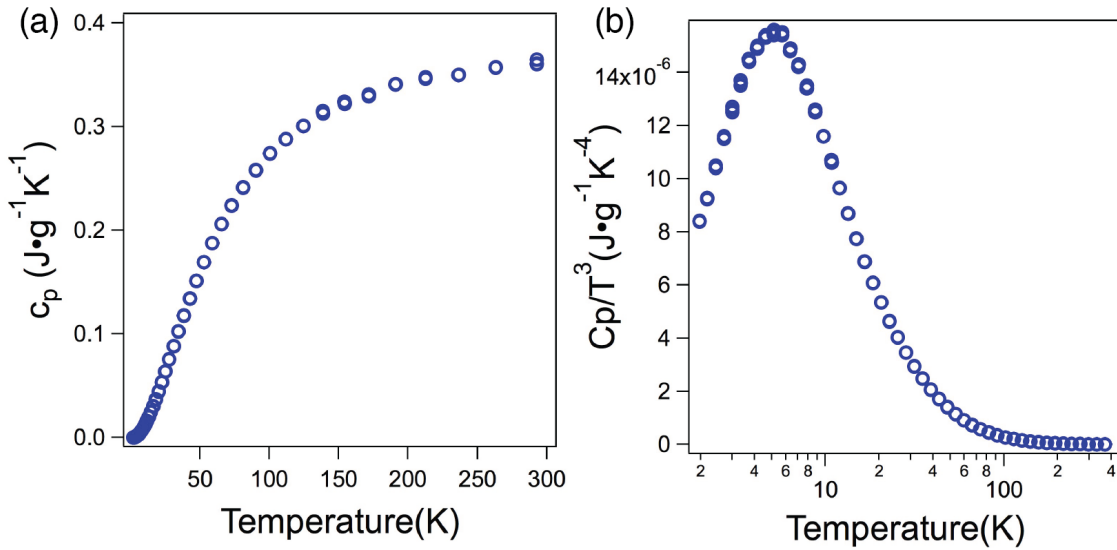
Figure 7.9: Low temperature heat capacity of Cu_2Se (a) indicates an Einstein mode (b) at approx 400 GHz.

It is likely that the measured κ is at or close to its particular glassy limit; this is a major reason for the excellent thermoelectric performance of Cu_2Se. A true glass is characterized by occupation of localized vibrational states instead of extended phonon states. These states will be of relatively low frequency — less than a terahertz — and their occupation will be by the Bose-Einstein distribution:

$$P = \frac{g_i}{e^{hf/k_bT} - 1} \tag{7.17}$$

With resulting heat capacity contribution of:

$$c_V = 3k_b \left(\frac{hf}{k_bT}\right)^2 \frac{e^{hf/k_bT}}{\left(e^{hf/k_bT} - 1\right)^2} \tag{7.18}$$

When c_v/T^3 is plotted as a function of T for a Bose oscilator, it indicates a peak at approximately $h_f = -0.2k_bT$ [98]. This peak is known as a Bose peak and it is characteristic of glassy behavior. A similar feature was observed in the heat capacity of low-temperature Zn_4Sb_3. That feature was successfully associated with phonon softening and that material's low thermal conductivity [173]. Analysis of low temperature heat capacity data shows Cu_2Se to have a pronounced Boson peak at 4 K, see Figure 7.9. This suggests a vibrational mode at 400 Gigahertz, and it is strongly indicative of glassy behavior.

We observed a zT peak concurrent with the lamba-type phase transition in Cu_2Se. Simultaneously, there is a dramatic increase in thermopower which cannot be explained in terms of a single parabolic band model using the measured Hall carrier concentration and transport data. Transport parameters are strongly affected by the continuous phase transition, with Hall mobility and thermal diffusivity in particular clearly following a critical power law, and the heat capacity showing a characteristic lambda shape. This behavior strongly suggests that Cu_2Ses phase transition zT peak is driven by entropy co-transport.

7.4 $Cu_{1.97}Ag_{0.03}Se$

In the prior section I explored how at the phase transition the figure-of-merit of Cu_2Se can be measured and a strong enhancement shown. However, it is unlikely that Cu_2Se is the ideal thermoelectric material of its class. In synthesizing the samples no care was given to the stoichiometry or the grain structuring. In fact, the source of the intrinsic high carrier concentration we observed in Cu_2Se, see Figure 7.5(a), remains a mystery. And though our understanding of the mechanism behind Cu_2Se phase transition performance is incomplete, we hope that by examining materials with
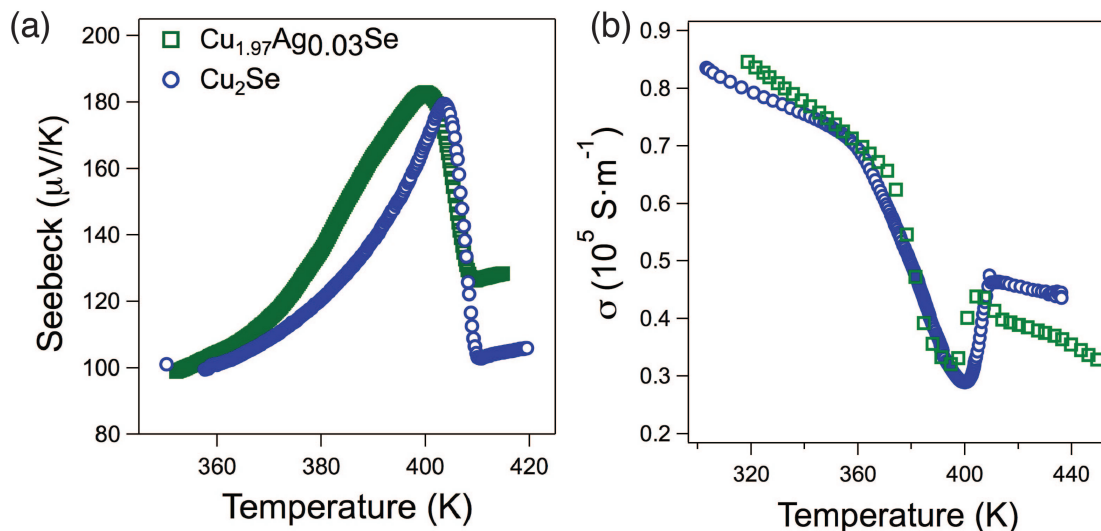
Figure 7.10: Comparison of Electrical Conductivity (a) and Seebeck (b) of $Cu_{1.97}Ag_{0.03}Se$ with Cu_2Se.

similar compositions that these properties may be expanded upon. Unfortunately, substituting a different element for the copper or the selenium may lead to secondary phase formation; the dissolution of these secondary phases — perhaps more soluble in $\alpha - Cu_2Se$ — may alter the nature of the phase transition and thereby destroy the effect in question of this study.

An interesting case is that of $Cu_{1.97}Ag_{0.03}Se$. In Chapter 5, section 5.4 I examined its structural phase transition through temperature-resolved PXRD. I determined it to show both a first order transition at $403K$, slightly lower than of Cu_2Se, but also to show a similar peak evolution as Cu_2Se below 380 K. At 380 K the secondary phase of $CuAgSe$ dissolves, and while some peaks change with the Cu_2Se trend until the first order phase transitions, others showed quite different behavior. There are a few other peaks which slowly diminish to the phase transition temperature; it is unclear if they are an unidentified impurity or additional peaks of a main phase that is slightly different from Cu_2Se.

The transport properties of $Cu_{1.97}Ag_{0.03}Se$ were measured via the same methods as those described for Cu_2Se in section 7.3 as well as in the chapters on experimental methodology (Chapter 2) and Sebeck metrology techniques (Chapter 3). For the sake

of comparison I plot the data for Cu_2Se and $Cu_{1.97}Ag_{0.03}Se$ together.

The electrical conductivity of $Cu_{1.97}Ag_{0.03}Se$, see Figure 7.10(a), is visually similar to that of Cu_2Se, showing all three characteristic features: a knee at 370 K, a minimum at 395 K, and a kink at 403 K. All three of these features occur at slightly different temperatures for the two samples. The decrease in temperature for the kink corresponds to the sudden first order transition observed. The slope of the conductivity below the knee at 370 K does not follow the power law described by Vucic; the temperature his empirical model predicts for Cu_2Se is 270 K. The concavity of the conductivity of $Cu_{1.97}Ag_{0.03}Se$ changes sign near 380 K, coincident with the dissolution of the $CuAgSe$ secondary phase into the matrix.

While the value of electrical conductivity is similar for both compositions in the phase transition range, the Seebeck of $Cu_{1.97}Ag_{0.03}Se$, see Figure 7.10(b), is markedly higher than that of Cu_2Se from 370 K to 400 K. In its increase it is broadened and shows an inhomogeneous shape. While its increase compared to Cu_2Se from 370 K to 380 K is correlated with the faster decrease in electrical conductivity, the increase and broadening above that temperature are likely due to the complicated interaction of the dissolved Ag with the Cu_2Se main phase. Above the phase transition, the Seebeck coefficient of Cu_2Se is slightly higher than of $Cu_{1.97}Ag_{0.03}Se$, but the electrical conductivity is correspondingly lower.

Comparison of the thermal properties of $Cu_{1.97}Ag_{0.03}Se$ and Cu_2Se are particularly illustrative. Just as in Cu_2Se the region of decreasing slope in σ matches a corresponding region in the thermal diffusivity, see Figure 7.11(a). The diffusivity decrease in $Cu_{1.97}Ag_{0.03}Se$ from 320 K to 360 K is much less than that in the same temperature range for Cu_2Se. Most notably there are two distinct minima in the diffusivity. The minima at 385 K resembles a critical power law decrease, as seen at the 410 K phase transition of Cu_2Se. Between 390 K and 410 K there is a steady decrease in the diffusivity, suggesting that the dissolution of the secondary phases is broadening out the phase transition region. As expected the phase transition temperature in thermal diffusivity occurs at a lower temperature for $Cu_{1.97}Ag_{0.03}Se$ than for Cu_2Se. In the high temperature phase D_T for Cu_2Se is slightly higher than that
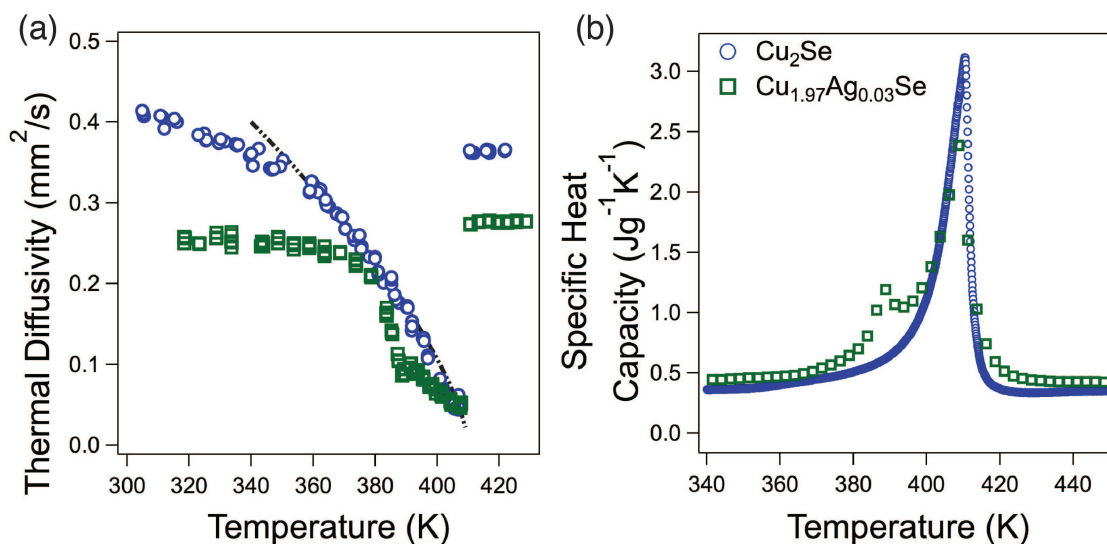
Figure 7.11: Comparison of D_t (a) and C_p(b) of $Cu_{1.97}Ag_{0.03}Se$ with Cu_2Se.

of $Cu_{1.97}Ag_{0.03}Se$. As this difference is similar to that of Cu_2Se, it is probably driven by a corresponding decrease in electronic thermal conductivity.

The double minima in D_T corresponds to a doubled peak in c_p, see Figure 7.11(b). The heat capacity baseline of $Cu_{1.97}Ag_{.03}Se$ is slightly higher than that of Cu_2Se — $0.42\,J/gK$ as compared to $0.37\,J/gK$. As the compositions are nearly identical, the Dulong-Petit heat capacity should be nearly the same, so this difference is due to systematic measurement error or from a higher coefficient of thermal expansion. The heat capacity from 320 K to 360 K is greater than he high temperature baseline, and it shows a linear increasing trend. At 360 K there is a kink in the heat capacity above which the data is non-linear. This kink exactly mirrors that seen in Cu_2Se, suggesting that though the middle temperature second order transition is more difficult to observe in $Cu_{1.97}Ag_{0.03}Se$ than Cu_2Se, it is a feature of both systems. The 403 K peak, representing in part a first order transition, must include a discrete enthalpy of formation. As I cannot determine which portion of the DSC curve is due to the enthalpy release of a first order phase transition, I treat all of it as a portion of the specific heat capacity. This will result in an unknown underestimate of the zT between 400 K and 420 K.

The zT of $Cu_{1.97}Ag_{0.03}Se$ dwarfs that of Cu_2Se, reaching a maximum of 0.95 at
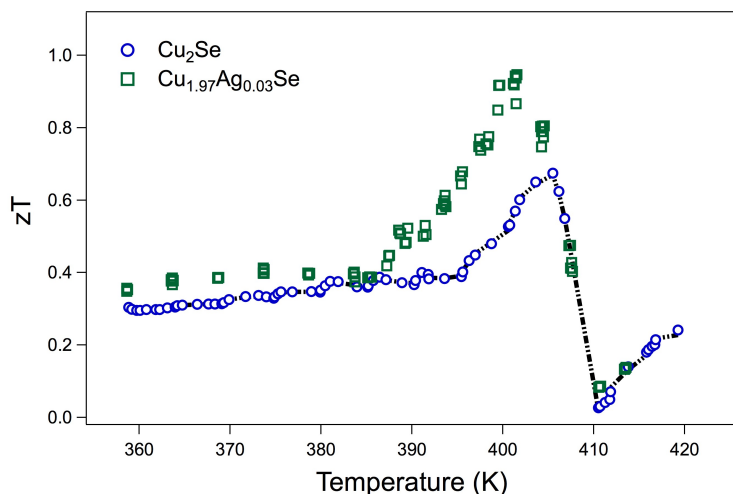
Figure 7.12: Comparison of zT of $Cu_{1.97}Ag_{0.03}Se$ with Cu_2Se.

402 K, see Figure 7.12. The maximum zT is reached just prior to the 1st order phase transition temperature. The zT shows a kink at 385 K, corresponding to the temperature of the secondary diffusivity minima and heat capacity peak as well as the dissolution of the CuAgSe phase. This is the same temperature at which the measured Seebeck for Cu_2Se begins to exceed the value predicted by the single parabolic band. This correlation may be causal. The disordering of the main phase may decrease the chemical potential for additional Ag or Cu to be added to it. By doing so it may instigate the dissolution.

Band structure analysis could not be performed on $Cu_{1.97}Ag_{0.03}Se$ due to bipolar affects from the secondary phase of CuAgSe. Measurements of Hall coefficient in the low temperature phase (Figure 7.13(a)) show it to be negative. For a single band thermoelectric the Hall coefficient and the Seebeck should have the same sign — that of the majority carrier. As discussed in detail in chapter 2, the effect of a minority carrier band is linear with its mobility in Seebeck but quadratic in the Hall coefficient. The CuAgSe secondary phase high mobility n-type bands with mobility of order $10^4 \, cm^2/V \cdot S$ [88]. As a band's Hall coefficient characteristic field is the inverse of its field, this indicates a transformation from electron to hole dominated behavior should occur in the 1 to 10 T range.
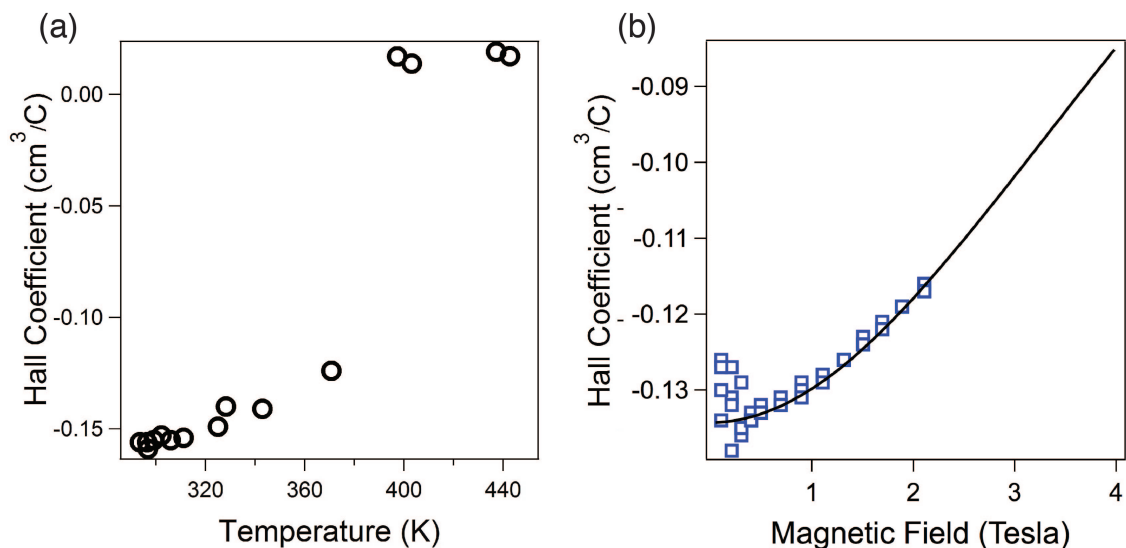
Figure 7.13: Hall coefficient for $Cu_{1.97}Ag_{0.03}Se$ at 2 T and varying temperature (a) and at 293 K with varying magnetic field.

The Hall coefficient was measured under magnetic fields varying from 0.1 T to 2.2 T in steps of 0.1 T below 1 T and in steps of 0.2 T above it. Though low field measurements were below the noise floor, data above 0.3 T showed a clear increasing trend, see Figure 7.13(b). This trend is consistent with two single carrier bands with $n = 1 \times 10^{17}\,cm^{-3}$, $\mu_n = 1440\,cm^2V^{-1}s^{-1}$, $p = 4 \times 10^{20}\,cm^{-3}$, and $\mu_p = 11cm^2V^{-1}s^{-1}$. The p-type characteristics were chosen to be similar to that of Cu_2Se and the n-type parameters adjusted until a visual fit could be made. This fit is shown as a black line in Figure 7.13(b).

When examining the transport properties near a phase transition, it is of utmost importance to verify that they are stable. When measuring the Seebeck coefficient via the ramp method, half of the data used was measured while the average sample temperature was increasing (on heating), and half the data was measured while the average sample temperature was decreasing (on cooling). From all of the voltage ΔT points measured at a given temperature, the Seebeck data shown in Figure 7.10 were determined. If the phase transitions are interfering with the transport properties, this should be visible in a difference between the Seebeck of the data from heating and cooling.
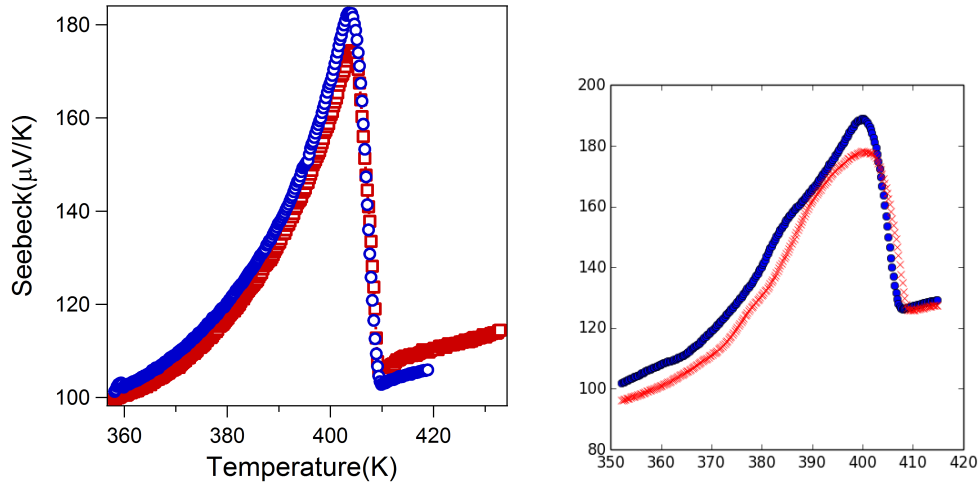
Figure 7.14: Ramp Seebeck fits for the cooling data (blue) and heating data (red) separately in Cu_2Se (a) and $Cu_{1.97}Ag_{0.03}Se$ (b)

The ramp method Seebeck determined for both the heating and cooling data is show in Figure 7.14(a) for Cu_2Se and in Figure 7.14(b) for $Cu_{1.97}Ag_{0.03}Se$. The data for Cu_2Se shows an offset of less than 5% between heating and cooling across the temperature range. The value at the 406 L zT peak is identical on both heating and cooling. The average value is midway between the heating and cooling curves. The differences between the curves are within systematic measurement uncertainty; they are probably due to a slight alteration in thermal contact resistance on heating and on cooling.

The data for $Cu_{1.97}Ag_{0.03}Se$ shows values that are within 10% on heating and cooling, other than in the small tempearture range above the 403 K phase transition. A small hysteresis in the data is observed. The line shapes of the curve are slightly different. The average Seebeck shown in Figure 7.14(b) is much closer to the date measured on heating than that measured on cooling. This suggests that the visually notable 5% discrepancy in the data at 400 K is driven by greater noise in the data on cooling than on heating. Another possibility is that there is a longer time-scale required for precipitation of an impurity phase than there is for its dissolution at the 403 K phase transition. The discrepant range corresponds to the temperatures between the first order phase transition and the dissolution of the CuAgSe secondary

phase. The precipitation and dissolution of the CuAgSe phase may increase the kinetics of secondary phase restructuring.
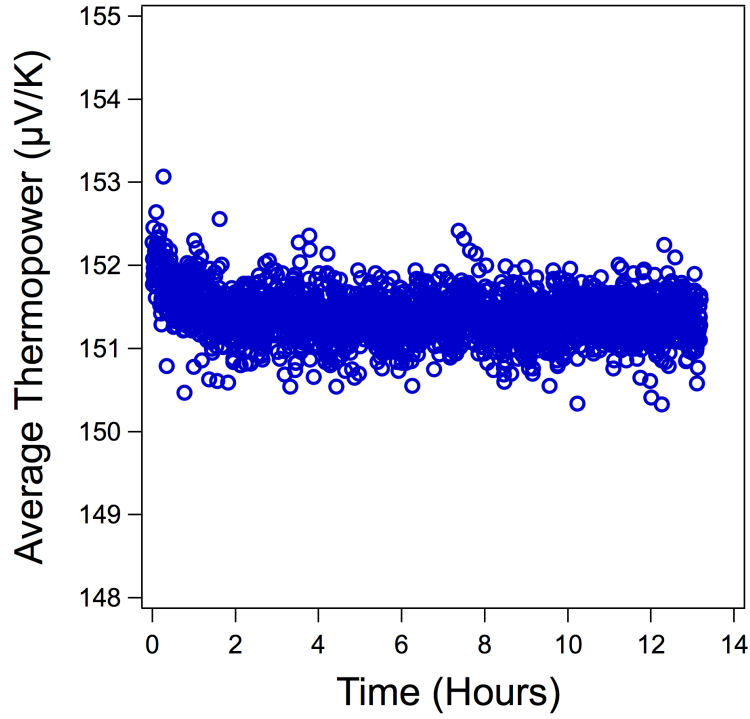
Figure 7.15: Measured Seebeck voltage of Cu_2Se at $\bar{T} = 390\,K$ and $\Delta T = 16\,K$. There was a variation of less than 1% in the measured values. After the temperature gradient stabilized there was no variation.

The Seebeck coefficient of Cu_2Se just below its phase transition temeprature is very stable, indicating it is a steady state property of the material, see Figure 7.15. The sample was held at an average temperature of 390 K and a temperature difference of 16 K for 13 hours. The measured thermopower, 152 $\mu V/K$, varied by less than 1% during this time period. The predicted average thermopower for this range was calculated by integration of the data show in Figure 7.2(a) as 143 $\mu V/K$. This 6% discrepenacy between the predicted and measured value is consistent with the repition error of Seebeck measurements. As the discrepancy would suggest that Seebeck and zT are underestimated, it does not undermine the conclusion of phase transition enhanced thermopower.

In the next and concluding chapter I will summarize the experimental results in the context of super-ionic phase transitions. I will present a suggestion for how the

data for Ag_2Se and Cu_2Se may be explained based on the irreversible thermodynamics of phase transitions.

Chapter 8

Order and Ion Enhanced Thermoelectrics

In Chapter 6 I presented data showing that the ordered phase of Ag_2Se has a larger zT in its ordered phase than its disordered phase, see Figure 8.1(a). This zT enhancement was predicted to within 5% by a corresponding enhancement of Seebeck, see Figure 8.1(b). The Seebeck change was shown to be neither predicted by the effective mass determined by Day *et al.* [46] or the measured Hall carrier concentration through the phase trasnsition.

In Chapter 7 I presented data showing that just below Cu_2Se and $Cu_{1.97}Ag_{0.03}Se$'s phase transition an enhancement in their zTs of 100% or more was observed, see Figure 8.1(c). This enhancement seemed driven by an 80% increase in their Seebecks over a 60 K temperature range, see Figure 8.1(d). In Cu_2Se n_H and μ_H could be measured through the phase transition in temperature. It was shown that the variation in n_H explained half of the peak in Seebeck, and that the temperature profile of the remaining part of the Seebeck peak explained the peak in zT. Bipolar conduction made a similar analysis of $Cu_{1.97}Ag_{0.03}Se$ impractical.

In this chapter I will provide an explanation for this enhancement in thermoelectric performance. First, I will explain based on the Onsager equations how there might be additional Seebeck and zT beyond that predicted by band structure modeling. Second, I will show that the differing behaviors of Ag_2Se and Cu_2Se can be explained by the Landau theory of order-disorder phase transitions. Finally, I will present
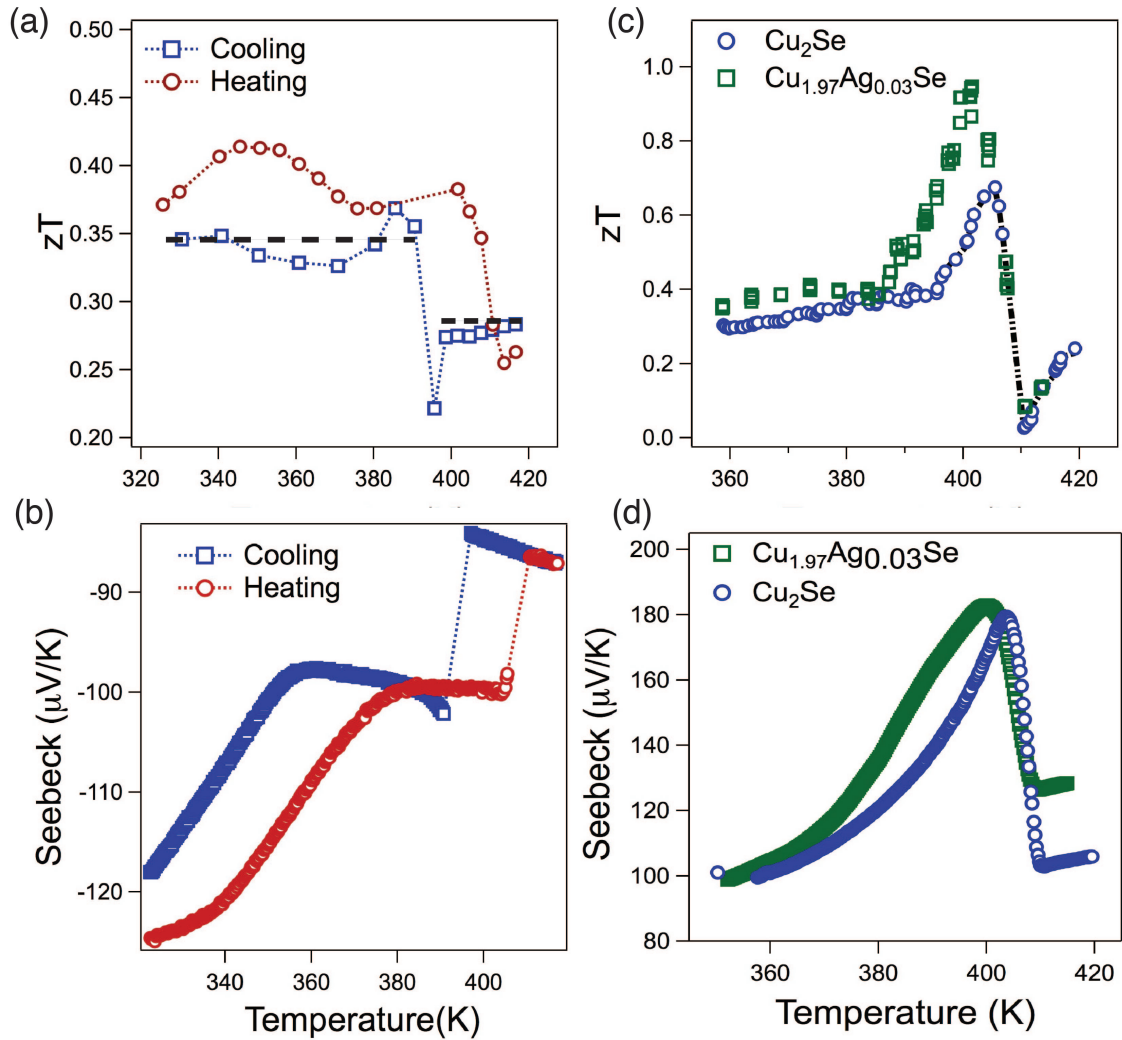
Figure 8.1: Key results of this thesis. Concurrent with its first order transition there is a step change in Ag_2Ses zT (a) and Seebeck (c). The second order transition of Cu_2Se results in a sharply peaked zT (a) and Seebeck (d). The zT and Seebeck of the mixed phase transition of $Cu_{1.97}Ag_{0.03}Se$ resembles that of its Cu_2Se main phase. Dotted lines are guides for the eye.

in detail a similar analysis on the basis of the ionic nature of the particular order-disorder phase transitions. This will allow me to present particular literature results supportive of my hypothesis and provide an experimentally tractable basis for testing these theories.

8.1 Ordering Entropy Enhancement

In Chapter 7 I presented the Onsager coefficients typically presented [69] for a thermoelectric system. It was on the basis of a two term entropy production equation of form:

$$T\dot{S} = -J_s \cdot \nabla T - J_e \cdot \nabla \mu_e \tag{8.1}$$

In which $V \equiv \frac{\tilde{\mu}_e}{e}$ and J_e is a quantity flux rather than a charge flux, *i.e.* defined by $J = qJ_e$. This leads an Onsager matrix of form:

$$\begin{bmatrix} J_e \\ J_s \end{bmatrix} = - \begin{bmatrix} {}^2L_{ee} & {}^2L_{es} \\ {}^2L_{se} & {}^2L_{ss} \end{bmatrix} \begin{bmatrix} \nabla\tilde{\mu}_e \\ \nabla T \end{bmatrix} \tag{8.2}$$

In which the subscript 2 is used for didactic purposes. But imagine if there is a second thermodynamic quantity that transports. Without loss of generality, lets call it m and lets call its conjugate flux h. Then the corresponding internal energy differential to that used for Equation 8.2 is:

$$du = Tds + \tilde{\mu}_e dn_e + hdm \tag{8.3}$$

The corresponding entropy production is:

$$T\dot{S} = -J_s \cdot \nabla T - J_e \cdot \nabla \mu_e - J_m \nabla h \tag{8.4}$$

As a sidenote, if $J_m > 0$ than Equation 8.4 will apparently not capture the entirety of the entropy transported, though this problem can be overcome if J_s is replaced with some other entropy-like flux [132]. In this case there would be dissipation from

a non-electronic transport quantity that must affect the maximal zT and η of the system. In the analysis below I principally consider the condition of $J_m = 0$, and so this complication does not enter in.

The Onsager matrix that corresponds to Equation 8.4 is:

$$
\begin{bmatrix} J_e \\ J_m \\ J_s \end{bmatrix} = - \begin{bmatrix} {}^3L_{ee} & {}^3L_{ms} & {}^3L_{es} \\ {}^3L_{me} & {}^3L_{mm} & {}^3L_{ms} \\ {}^3L_{se} & {}^3L_{sm} & {}^3L_{ss} \end{bmatrix} \begin{bmatrix} \nabla\tilde{\mu}_e \\ \nabla h \\ \nabla T \end{bmatrix}
$$
(8.5)

The essential complication arises from this: ${}^2L_{se} \neq^3 L_{se}$ for all conditions, but ${}^3L_{se}$ is that which is calculated by the band structure models presented earlier and generally calculated from density functional theory. The discrepancy between them gives the contribution of entropy co-transport to thermoelectric performance. This is not to say that the kinetic theory that underlies such calculations is incorrect, but rather that if incomplete information is given to them they cannot provide the correct results. The measure Seebeck coefficient is always give by:

$$
\alpha = \frac{\nabla V}{\nabla T}_{J_e=0} = \frac{1}{q}\frac{-{}^2L_{se}}{{}^2L_{ee}}
$$
(8.6)

With $J_e = 0$ indicating the material is measured with an open electrical circuit. The relation between the Onsager L coefficients from Equation (8.1) and those from Equation (8.4) will depend on the boundary conditions, i.e. $\nabla h = 0$ or $\nabla m = 0$. The cases of both ∇h, $\nabla\tilde{\mu}_e = 0$ and $J_m = 0$, $J_e = 0$ were both considered by DeGroot in the context of thermodfifusion [132], while the case of $J_e = 0$, $\nabla m = 0$ was recently consider by Sandbakk *et al.* [171] in the context of coupled ion and volume transport in ion-membrane thermoelectrics.

In the case of $\nabla h = 0$, the Seebeck expressed in terms of Equation 8.5 is:

$$
\alpha = \frac{\nabla V}{\nabla T}_{J_e=0,\,\nabla h=0} = \frac{-1}{q}\frac{{}^3L_{se}}{{}^3L_{ee}}
$$
(8.7)

This gives the same form as that of Equation 8.6, except that there may be some

external dissipation due to $J_m \neq 0$ that limits the heat to electron conversion efficiency possible. The conditions of a normal thermoelectric may be thought of as having $L_{mm} = 0$, so that $J_m = 0$ implies $\nabla h = 0$ — and there is therefore neither co-transport or dissipation. The other transport coefficients (σ, κ) will behave similarly [171].

In the case of $J_m = 0$, the Seebeck expressed in terms of Equation 8.5 is:

$$\alpha = \frac{\nabla V}{\nabla T}\bigg|_{J_e=0,\,J_m=0} = \frac{-1}{q}\frac{^3L_{se}}{^3L_{ee}}\left(\frac{1 - \frac{^3L_{ms}}{^3L_{mm}}\frac{^3L_{me}}{^3L_{es}}}{1 - \frac{^3L_{me}}{^3L_{mm}}\frac{^3L_{me}}{^3L_{ee}}}\right) \tag{8.8}$$

The expression $\frac{^3L_{ms}}{^3L_{mm}}$ is the equivalent to the Seebeck coefficient but associated with transport of m instead of electron transport. That is:

$$\alpha_m \equiv \left(\frac{\nabla h}{\nabla T}\right)_{\nabla\tilde{\mu}_e,\,J_m=0} = \frac{^3L_{ms}}{^3L_{mm}} \tag{8.9}$$

Like α, α_m has its own presence contribution and that may be defined as:

$$\alpha_{m,\,presence} = -\left(\frac{\partial s}{\partial m}\right)_{u,n} \tag{8.10}$$

The expression $\frac{^3L_{em}}{^3L_{ee}}$ is the co-transport of J_m with J_e when there is no driving force for direct transport of m. It will have its own presence contribution:

$$\left(\frac{J_m}{J_e}\right)_{\nabla T=0,\,\nabla h=0} \approx \left(\frac{\partial m}{\partial n}\right)_{u,s} \tag{8.11}$$

This expression will be most accurate if all transport of m is mediated by transport of the electrons. This is certainly the case in the spin-state enhancement of Seebeck observed in oxide thermoelectrics [109, 196]. Due to the independent mobility of ions in Ag_2Se and Cu_2Se, Equation 8.11 is here only an approximation.

By combining Equation 8.10 and Equation 8.11 into a single expression, a quasi-thermodynamics expression for the entropy co-transport Seebeck may be obtained. Lets call this term $\alpha_{order-entropy}$. It can be formulated in terms of the free energy

density (f) and T as:

$$\alpha_{order-entropy} = \frac{-1}{q} \left(\frac{\partial f}{\partial m}\right)_{T,n} \left(\frac{\partial m}{\partial n}\right)_{T,s} \tag{8.12}$$

The behavior of the order-entropy contribution to Seebeck near the phase transition will depend on the behavior of the order parameter (m) near the phase transition. This is expressed as a polynomial expansion in m with phenomenological thermodynamic coefficients. For a first order transition the form is [32]:

$$f_{1st} = am^2 + cm^3 + bm^4 + hm \tag{8.13}$$

With a, b, and c thermodynamic coefficients The cubic term causes the first order transition. Equation 8.13 can be solved for m such that $f_{1st}(m, h = 0) = 0$. For example, under the condition $c \gg b$, a:

$$m = \begin{cases} \frac{-c}{b} & T < T_c \\ 0 & T > T_c \end{cases} \tag{8.14}$$

From Equation 8.14 $\frac{\partial m}{\partial n}$ will be a value that is dependent on the systems microscopics below T_c as expressed in the quantities b and c. Above the phase transition $\frac{\partial m}{\partial n}$ must be zero, because m is zero. By substituting Equation 8.14 in Equation 8.13 the relation $\left(\frac{\partial f}{\partial m}\right)_{T,n} = h$ is determined. Though there is no externally applied h, there is an internally induced h. The temperature gradient will induce a gradient in the order parameter. That order parameter gradient must induce a restoring force through a non-zero h. Using the functional forms of $\frac{\partial m}{\partial n}$ and $\frac{\partial f}{\partial m}$ described above, Equation 8.12 indicates that a first order transition may have a step change in $\alpha_{order-entropy}$ at T_c. An order entropy induced step change in Seebeck would explain the increase in the Seebeck and zT of Ag_2Se in its ordered phase.

Below a second order transition, the order parameter follows a critical power law. As dicussed in Chapter 5 it is characterized by a critical exponent, $m = m_0\tau_r^\beta$, with reduced temperature $\tau_r \equiv (T_cT)/T_c$ and $\beta > 0$. The Seebeck coefficient should also

include a critical exponent contribution and be of form:

$$\alpha = \alpha_0 + \alpha_1 \tau_r^r, \qquad (8.15)$$

in which α_0 and α_1 may have a separate temperature dependence.

Laguesse et al [115] suggested that Seebeck should have a critical exponent of $r = 1 - \lambda$, where λ is the critical exponent for heat capacity. As λ is less than unity, Laguesse et al. predicted r to be greater than 0. This would imply no Seebeck peak and thereby contradict both our observations in Cu_2Se [23] and also the critical exponent of $r = -1$ that Laguesse et al. measured in $YBa_2Ca_3O_{7-y}$ [115]. If h is large (relative to τ_r^Δ, where Δ is the gap exponent) [95], then the critical exponent for Seebeck will be larger than $1 - \lambda$. The free energy can be expressed as [95]:

$$f_{2nd} = \begin{cases} f_0 \tau_r^{2-\lambda} & \text{h small} \\ f_1 \tau_r^{\beta} & \text{h large} \end{cases} \qquad (8.16)$$

A form for $\frac{\partial f}{\partial n}$ can be obtained from Equation 8.16:

$$\alpha_{order-entropy} = -\frac{\partial f_{2nd}}{q \partial n} = \begin{cases} \alpha_1 \tau_r^{1-\lambda} \frac{\partial T_c}{\partial n} & \text{h small} \\ \alpha_2 \tau_r^{\beta-1} \frac{\partial T_c}{\partial n} & \text{h large} \end{cases} \qquad (8.17)$$

From Equation 8.17b if h is large enough, the critical exponent for Seebeck is $r = \beta - 1$. As β is typically a small fraction of unity, r should be slightly more than -1. That critical exponent is consistent with that measured in both our work on Cu_2Se and the work by Laguesse et al. on $YBa_2Ca_3O_{7-y}$ [115]. The form in of Equation 8.17b can also be determined from our Equation 8.13 and the definition of $m(T)$:

$$\frac{\partial m}{\partial n} = m_0 \tau_r^{\beta-1} \frac{T}{T_c^2} \frac{\partial T_c}{\partial n} \qquad (8.18)$$

As per our discussion of the first order transition, the temperature gradient will induce $h \neq 0$. Therefore $\left(\frac{\partial f}{\partial m}\right)_{T,n} = h$ is non-zero. If this is applied with Equation 8.18 to
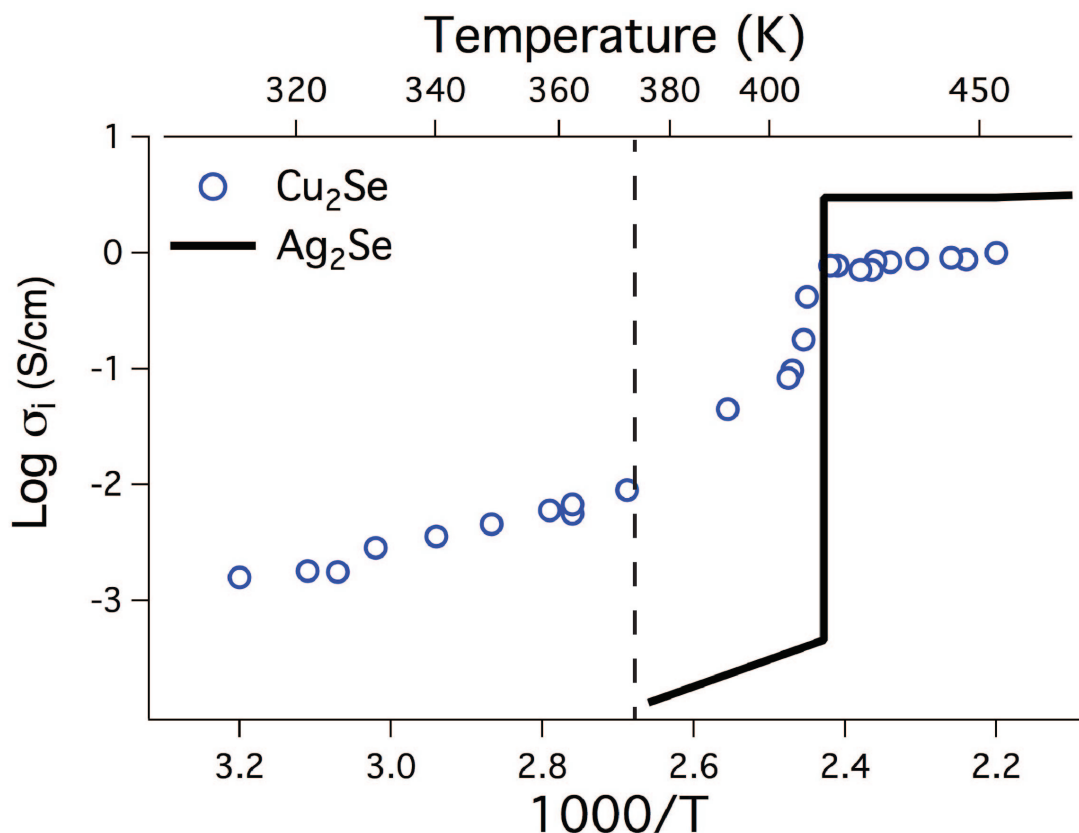
Figure 8.2: Ion conductivity of Cu_2Se [84] and Ag_2Se [136] through their phase transitions. Ag_2Se shows a step increase in ion conductivity at its phase transition, while Cu_2Se shows a super-exponential increase in ion conductivity to the phase transition temperature. The dotted line corresponds to 374 K, at which temperature the super-exponential increase begins.

Equation 8.12, the form and critical exponent of Equation 8.17b are obtained.

8.2   Ion-mediated Enhancement

When considering the specific case of super-ionic transitions, ionic transport properties may function as a convenient and metrologically tractable proxy for measurements of the order parameter. A super-ionic transition is a disordering of mobile ions that results in a substantial change in ionic transport properties. The enhancements in ionic transport may be much more significant than those of electronic transport, and

the phase transition may act on the electrons indirectly through the ions. In this case we have:

$$\frac{\partial T_c}{\partial n} = \frac{\partial T_c}{\partial n_i}\frac{\partial n_i}{\partial n} \qquad (8.19)$$

Where n_i is the concentration of mobile ions. If ionic transport is directly enhanced by the phase transition, $\frac{\partial T_c}{\partial n_i}$ will be non-zero.. Such a variation has been observed in both Cu_2Se [194] and Ag_2Se [15] as well as other super-ionics [111, 114]. Electrons and ions may interact through both chemical and electrostatic processes; their co-transport interaction would indicate a significant value for $\frac{\partial n_i}{\partial n}$. Polarization measurements of some oxygen conductors have revealed such coupled transport [205, 119, 36], which has been explained as being due to a long range electrostatic interaction changing the effective charge of the transported ions [99]. As $\frac{\partial T_c}{\partial n}$ and $\frac{\partial \alpha}{\partial n}$ may be obtainable via gated transport measurements [172], future studies may be able to precisely test Equation 8.17b.

Super-ionic materials are defined phenomenologically as those with ion conductivity greater than 1 S/cm at elevated temperatures [21, 87, 163]. They are divided into three classes by the manner in which they achieve high ion conductivity. Type III super-ionics are those without a phase transition (*e.g.* β-Alumina) [21] and therefore are not of interest here. This study is of the ordered or non-superionic phase of both Ag_2Se and Cu_2Se and therefore their classification within the broader contexts will be helpful in finding similar materials.

Type I and type II super-ionic conductors are characterized by a structural phase transition with an entropy change close to that of melting (i.e. order $10\,JK^{-1}mol^{-1}$ and a concurrent increase in ion conductivity [151]. For type I super-ionic conductors there is a sudden enthalpy release at the phase transition temperature (i.e. a first order phase transition) and a concurrent discontinuous increase in ionic conductivity [21]. For type II super-ionic conductors the ionic conductivity increases super-exponentially up to the phase transition temperature, the structure changes continuously, and there is a lambda-shaped peak in heat capacity like that characteristic of a second order phase transitions [87].
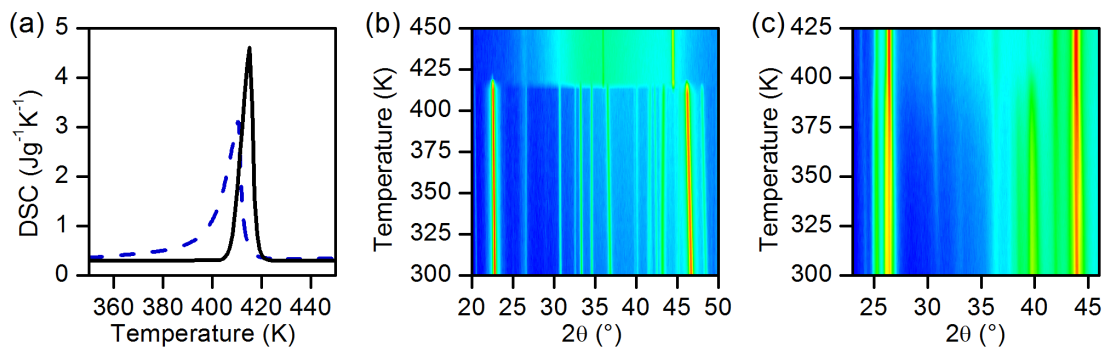
Figure 8.3: Calorimetry data (a) for Ag_2Se (solid line) and Cu_2Se (dotted line) on heating. Ag_2Se shows a characteristic symmetric peak in its DSC curve due to the enthalpy release of its first order phase transition. Cu_2Se shows an extended asymmetric elevation in its heat capacity due to its second order phase transition. Temperature resolved powder X-ray diffractograms of Ag_2Se (b) and Cu_2Se (c). The structural transformation of Ag_2Se is first order, while that of Cu_2Se is second order.

To determine whether a material in this study has a type I or type II super-ionic phase transition, three physical properties are examined through the phase transition: ionic conductivity, calorimetry, and crystallographic structure. A type I super-ionic transition (typically first order) is characterized by a sudden disordering of the ions [21, 87, 151]. As the number of mobile ions and their diffusivity increase suddenly, they show a concurrent step increase in ion conductivity. Literature results show that Ag_2Se ion conductivity increases by four orders of magnitude at 412 K, see Figure 8.2 [136] The disordering of the ions requires the absorption of enthalpy. DSC data for Ag_2Se shows a sharp symmetric peak centered at 414 K, see Figure 8.3(b). As the ordering of the ions is lost suddenly, there should be a corresponding change in the crystal symmetries represented by disappearance of peaks in the diffractogram. Temperature resolved PXRD shows numerous strong crystallographic peaks disappearing at the phase transition temperature, see Figure 8.3(b), indicative of a sudden disordering of the Ag ions.

In a type II super-ionic phase transition the ions disorder continuously (as in a second order transition) until the phase transition temperature is reached. The ionic conductivity increases super-exponentially below the phase transition temperature [21, 87, 151]. Horvatic et al. measured such a super-exponential increase in

the ionic conductivity of Cu$_2$Se, see Figure 8.2 [84] As the ionic disordering occurs continuously over a significant temperature range, the heat capacity is elevated over that range [151]. The DSC data for Cu$_S$e shows a broad asymmetric lambda peak, see Figure 8.3(a). Its crystal structure indicates gradual disordering and a second order phase transition, see Figure 8.3(c). From the behavior of its ionic conductivity, heat capacity and crystallography through its phase transition temperature, we conclude that Cu$_2$Se has a type II super-ionic phase transition.

Experimentally, we have seen an example of the contrast between a type II and type I super-ionic thermoelectric material in Ag$_2$Se and Cu$_2$Se. Consider transport of heat, ions, and electrons:

$$du = Tds - \tilde{\mu}_e dn_e - \tilde{\mu}_i dn_i \tag{8.20}$$

The corresponding entropy production is:

$$T\dot{S} = -J_s \cdot \nabla T J_e \cdot \nabla \tilde{\mu}_e J_i \cdot \nabla \tilde{\mu}_i \tag{8.21}$$

The corresponding Onsager relationships are [132]:

$$\begin{bmatrix} J_e \\ J_i \\ J_s \end{bmatrix} = - \begin{bmatrix} {}^3L_{ee} & {}^3L_{is} & {}^3L_{es} \\ {}^3L_{ie} & {}^3L_{ii} & {}^3L_{is} \\ {}^3L_{se} & {}^3L_{si} & {}^3L_{ss} \end{bmatrix} \begin{bmatrix} \nabla \tilde{\mu}_e \\ \nabla \tilde{\mu}_e \\ \nabla T \end{bmatrix} \tag{8.22}$$

If the Seebeck coefficient is measured in an open circuit system with ion blocking electrodes (*i.e.* $J_i = 0$, $J_e = 0$):

$$\alpha = \frac{\nabla V}{\nabla T}_{J_e=0,\, J_i=0} = \frac{-1}{q} \frac{{}^3L_{se}}{{}^3L_{ee}} \left(\frac{1 - \frac{{}^3L_{iq}}{{}^3L_{ii}} \frac{{}^3L_{ie}}{{}^3L_{eq}}}{1 - \frac{{}^3L_{ie}}{{}^3L_{ii}} \frac{{}^3L_{ie}}{{}^3L_{ee}}} \right) \tag{8.23}$$

The first term in the numerator is the band structure electronic Seebeck. The second term in the numerator is the Seebeck enhancement due to the ions. The term in the denominator is an ionic drag term. The ionic drag term will be small because

$L_{ii} \ll L_{ee}$ and L_{ie} is even in the largest measured case only on the order of L_{ii}. If L_{is} and L_{ie} are significant compared to L_{es} and L_{ee}, analysis of only electronic properties will lead to an incomplete description of the thermoelectric properties.

The first condition for the ion transport enhancing Seebeck is that $\frac{L_{ie}}{L_{ee}} = \frac{\sigma_{ie}}{\sigma_{ee}}$ be large. $\frac{L_{ie}}{L_{ee}} = \frac{\sigma_{ie}}{\sigma_{ee}}$ is the ratio between ions transported and electrons transported under a gradient in $\tilde{\mu}_e$ but no gradient in $\tilde{\mu}_i$. Mixed ion-electron conductors can show electron-ion transport coupling. Electrons and ions may interact through both chemical and electrostatic processes. Polarization measurements of some oxygen conductors have revealed such a coupling [205, 119], which has been explained as due to a long range electrostatic interaction changing the effective charge of the transported ions [99]. Thus in both low temperature type I Ag_2Se and type II Cu_2Se $\frac{L_{ie}}{L_{ee}}$ may be significant. In the high temperature phase of Ag_2Se $\frac{L_{ie}}{L_{ee}}$ has been measured to be less than 10^{-2} [137]. This has been explained by Ogawa and Kobayashi [141, 142] to be due to the high concentration of ionic carriers. In the super-ionic limit they found that $\frac{L_{ie}}{L_{ii}} < \frac{n_e}{n_i}$. n_i is much larger in the superionic phase than the ordered phase [142].

The second condition is that ionic Seebeck, $\alpha_i = -\frac{L_{is}}{L_{ii}}$ be significant. The coupling of concentration of Ag and Cu to the thermodynamics of disordering has been observed via the dependence of T_c on composition in Cu_2Se [194] and Ag_2Se [15]. Mechanistically this may function through a dependence of occupation of soft modes (e.g. the Zn_4Sb_3 rattler) [173] on the concentration of Ag^+ and Cu^+. An observation of not only structural entropy change at the phase transition but also of structural entropy transport is given by Korzhuev and Laptev [107]; they measured a sharp peak in the thermodiffusion of Cu^0 in Cu_2Se at the 410 K phase transition. From this they calculated a heat of transport of $Q^*_{Cu^0}$ of Cu atoms of 1 eV. Conservation of particles and charge requires that:

$$Q^*_{Cu^0} = Q^*_{Cu^+} Q^*_p = qT(\alpha_{Cu^+} - \alpha) \tag{8.24}$$

Therefore $Q^*_{Cu^0} = 1\,eV$ corresponds to $\alpha_{Cu^+} \approx 2500\,\mu V/K$ at the phase transition. If even 2% small fraction of this copper entropy were co-transported with Cu_2Se, than

the Seebeck and zT enhancement observed would be completely explained.

8.3   Future work

Other super-ionic materials should be evaluated for their phase transition thermo-electric properties. The thermoelectric materials Ag_2S, Ag_2Te, Cu_2S, and Cu_2Te are all type I super-ionics [87]; like Ag2Se, they are not expected to show phase transition enhanced Seebeck. There are many other known type II super-ionic conductors [21] such as PbF_2 [9, 34] and K_2S [51]. Like Cu_2Se they have a modified fluorite (or anti-fluorite) structure. Because of their large band gaps, their thermoelectrics properties are unexamined. It may be possible to change Ag_2Se from a type I to a type II superionic material. The order of the phase transition has been changed in certain super-ionic materials by alloying. PbF_2 is type II super-ionic. Alloying it with KF changes the temperature dependence of its ionic conductivity. At 10% KF and above it becomes a type I super-ionic [86]. Though AgI is type I, $RbAg_4I_5$ has both a type I and type II super-ionic transition [93]. Additionally, when a pressure of 2.6 GPa is applied to AgI, it becomes a type II super-ionic conductor [97].

Critically increased entropy may be present in other materials systems. $AgCrSe_2$ [66] which is also an ion transporting materials shows a small Seebeck enhancement near a phase transition, though there is no evidence that this is associated with critical phenomena. The temperature of the continuous transition in the CuI-AgI system shows a composition dependence [114]. The effect on Seebeck from order entropy is likely not limited to mixed ion-electron conductors. Any material in which the entropy associated with a phase transition might be coupled to transport is a candidate. For example, the magnetic ordering phase transition associated with giant magneto-resistance is often accompanied by a corresponding significant Seebeck change [91, 120]. Applying a magnetic field to these materials induces ordering and results in a corresponding reduction in Seebeck.

In order to understand and engineer this phenomenon, substantial future work needs to be done. The ionic properties, both the conductivity [107] and the See-

beck, [12] may need to be measured and considered when engineering these materials. Further synchotron and neutron crystallographic work may be able to uncover the structure and order parameter. The Onsager coefficient analysis above may be used to relate separate measurements of ion and electronic properties, in order to directly test the hypothesis of ion-mediated or perhaps even order-mediated Seebeck enhancment.

The best thermoelectric performing materials in this class of compound are yet to be synthesized. Through such future work a greater understanding of the excellent thermoelectric properties of the ordered phases of super-ionic materials may be understood and engineered.

Bibliography

[1] FF Aliev, MB Jafarov, and VI Eminova. Thermoelectric figure of merit of Ag$_2$Se with Ag and Se excess. *Semiconductors*, 43(8):977–979, 2009.

[2] SA Aliev. Hysteresis in Ag$_2$Te near and within the phase transition region. *Semiconductors*, 38(7):796–799, 2004.

[3] D. P. Almond and A. R. West. Ultrasonic attenuation studies of solid electrolytes. *Solid State Ionics*, 26(4):265–278, 1988.

[4] M. Aniya. A chemical approach for the microscopic mechanism of fast ion-transport in solids. *Solid State Ionics*, 50(1-2):125–129, 1992.

[5] M. Aniya. Superionicity as a local fluctuation of the chemical-bond. *Solid State Ionics*, 70:673–677, 1994.

[6] M. Aniya, T. Usuki, M. Kobayashi, and H. Okazaki. Liquidlike model for thermal conductivity in superionic conductors. *Physical Review B*, 41(10):7113–7117, 1990.

[7] TL Aselage, D Emin, SS McCready, and RV Duncan. Large enhancement of boron carbides' seebeck coefficients through vibrational softening. *Physical review letters*, 81(11):2316, 1998.

[8] Bahram M Askerov. *Electron transport phenomena in semiconductors*, volume 394. World Scientific, 1994.

[9] T. S. Aurora, D. O. Pederson, and S. M. Day. Thermal-expansion and index-of-

refraction variation in Lead Fluoride between 300 and 850 k. *Physical Review B*, 41(14):9647–9649, 1990.

[10] M. Bailyn. Transport in metals - effect of the nonequilibrium phonons. *Physical Review*, 112(5):1587–1598, 1958.

[11] M. Bailyn. Phonon-drag part of thermoelectric power in metals. *Physical Review*, 157(3):480, 1967.

[12] M. Kh Balapanov, I. B. Zinnurov, and G. R. Akmanova. The ionic seebeck effect and heat of cation transfer in Cu_2Se superionic conductors. *Physics of the Solid State*, 48(10):1868–1871, 2006.

[13] Lon E. Bell. Cooling, heating, generating power, and recovering waste heat with thermoelectric systems. *Science*, 321(5895):1457–1461, 2008.

[14] Gerardo Beni. Thermoelectric power of the narrow-band hubbard chain at arbitrary electron density: Atomic limit. *Physical Review B*, 10(6):2186–2189, 1974.

[15] Heinrich Billetter and Uwe Ruschewitz. Structural phase transitions in ag2se (naumannite). *Zeitschrift fr anorganische und allgemeine Chemie (1950)*, 634(2):241–246, 2008.

[16] Kurt Binder. Theory of first-order phase transitions. *Reports on progress in physics*, 50(7):783, 1987.

[17] D. Bolmatov, V. V. Brazhkin, and K. Trachenko. The phonon theory of liquid thermodynamics. *Sci. Rep.*, 2:421, 2012.

[18] P. Boolchand and W. J. Bresser. Mobile silver ions and glass formation in solid electrolytes. *Nature*, 410(6832):1070–1073, 2001.

[19] J. M. Borrego. Zener's maximum efficiency derived from irreversible thermodynamics. *Proceedings of the IEEE*, 52(1):95–95, 1964.

[20] K. A. Borup, E. S. Toberer, L. D. Zoltan, G. Nakatsukasa, M. Errico, J. P. Fleurial, B. B. Iversen, and G. J. Snyder. Measurement of the electrical resistivity and hall coefficient at high temperatures. *Review of Scientific Instruments*, 83(12):123902, 2012.

[21] J. B. Boyce and B. A. Huberman. Superionic conductors - transitions, structures, dynamics. *Physics Reports-Review Section of Physics Letters*, 51(4):189–265, 1979.

[22] J. B. Boyce, J. C. Mikkelsen, and M. Okeeffe. Ion dynamics and sublattice melting in superionic conductor PbF_2. *Solid State Communications*, 21(10):955–958, 1977.

[23] David R. Brown, Tristan Day, Kasper A. Borup, Sebastian Christensen, Bo B. Iversen, and G. Jeffrey Snyder. Phase transition enhanced thermoelectric figure-of-merit in copper chalcogenides. *APL Materials*, 1(5):052107, 2013.

[24] David R. Brown, Tristan Day, Thierry Caillat, and G. Jeffrey Snyder. Chemical stability of (ag,cu)2se: a historical overview. *Journal of Electronic Materials*, 42(7):2014–2019, 2013.

[25] David R Brown, Yanzhong Pei, Heng Wang, and G Jeffrey Snyder. Linear dependence of the hall coefficient of 1% Na doped PbTe with varying magnetic field. *physica status solidi (a)*, 2014.

[26] D.R. Brown. In preparation.

[27] G. Bush and P. Junod. Relations between the crystal structure and electronic properties of the compounds Ag_2S, Ag_2Se, Cu_2Se. *Helvetica Physica Acta*, 32(6-7):567–600, 1959.

[28] David G Cahill and RO Pohl. Lattice vibrations and heat transport in crystals and glasses. *Annual Review of Physical Chemistry*, 39(1):93–121, 1988.

[29] David G. Cahill, S. K. Watson, and R. O. Pohl. Lower limit to the thermal conductivity of disordered crystals. *Physical Review B*, 46(10):6131–6140, 1992.

[30] T. Caillat, J. P. Fleurial, and A. Borshchevsky. Preparation and thermoelectric properties of semiconducting zn4sb3. *Journal of Physics and Chemistry of Solids*, 58(7):1119–1125, 1997.

[31] H.B. Callen. *Thermodynamics: an introduction to the physical theories of equilibrium thermostatics and irreversible thermodynamics*. Wiley, 1960.

[32] Herbert B. Callen. The application of onsager's reciprocal relations to thermoelectric, thermomagnetic, and galvanomagnetic effects. *Physical Review*, 73(11):1349–1358, 1948.

[33] Sadi Carnot, Hippolyte Carnot, and William Thomson Baron Kelvin. *Reflections on the motive power of heat and on machines fitted to develop this power*. J. Wiley, 1890.

[34] M. J. Castiglione and P. A. Madden. Fluoride ion disorder and clustering in superionic pbf2. *Journal of Physics-Condensed Matter*, 13(44):9963–9983, 2001.

[35] Eric Chalfin, Hongxia Lu, and Rdiger Dieckmann. Cation tracer diffusion in the thermoelectric materials $Cu_3Mo_6Se_8$ and $\alpha - zn_4sb_3$. *Solid State Ionics*, 178(5):447–456, 2007.

[36] Christodoulos Chatzichristodoulou, Woo-Seok Park, Hong-Seok Kim, Peter Vang Hendriksen, and Han-Ill Yoo. Experimental determination of the onsager coefficients of transport for $Ce_{0.8}Pr_{0.2}O_2$-[small delta]. *Physical Chemistry Chemical Physics*, 12(33):9637–9649, 2010.

[37] Steven Chu and Arun Majumdar. Opportunities and challenges for a sustainable energy future. *nature*, 488(7411):294–303, 2012.

[38] Rudolf Clausius. *The mechanical theory of heat*. Macmillan and Company, 1879.

[39] JL Cohn, SA Wolf, V Selvamanickam, and K Salama. Thermoelectric power of yba 2 cu 3 o 7-: Phonon drag and multiband conduction. *Physical review letters*, 66(8):1098, 1991.

[40] 3M Corporation. Program to design an advanced technology thermoelectric module for a 2 kw power system and to fabricate and test a heat pipe/thermoelectric module. Report, 1970.

[41] S. A. Danilkin, M. Avdeev, T. Sakuma, R. Macquart, and C. D. Ling. Neutron diffraction study of diffuse scattering in $Cu2 - \delta Se$ superionic compounds. *Journal of Alloys and Compounds*, 509(18):5460–5465, 2011.

[42] S. A. Danilkin, M. Avdeev, M. Sale, and T. Sakuma. Neutron scattering study of ionic diffusion in cu-se superionic compounds. *Solid State Ionics*, 225:190–193, 2012.

[43] Sergey Danilkin. Diffuse scattering and lattice dynamics of superionic copper chalcogenides. *Solid state ionics*, 180(6-8):483–487, 2009.

[44] Sergey Danilkin, Mohana Yethiraj, and Gordon J. Kearley. Phonon dispersion in superionic copper selenide: Observation of soft phonon modes in superionic phase transition. *Journal of the Physical Society of Japan*, 79(Suppl. A):25–28, 2010.

[45] T. Dasgupta, C. Stiewe, A. Sesselmann, H. Yin, B. B. Iversen, and E. Mueller. Thermoelectric studies in -zn4sb3the complex interdependence between thermal stability, thermoelectric transport, and zinc content. *Journal of Applied Physics*, 113(10):103708, 2013.

[46] Tristan Day, Fivos Drymiotis, Tiansong Zhang, Daniel Rhodes, Xun Shi, Lidong Chen, and G. Jeffrey Snyder. Evaluating the potential for high thermoelectric efficiency of silver selenide. *Journal of Materials Chemistry C*, 1(45):7568–7573, 2013.

[47] J. de Boor and E. Muller. Data analysis for seebeck coefficient measurements. *Rev Sci Instrum*, 84(6):065102, 2013.

[48] Gilles Dennler, Radoslaw Chmielowski, Stphane Jacob, Frdric Capet, Pascal Roussel, Sebastian Zastrow, Kornelius Nielsch, Ingo Opahle, and Georg K. H. Madsen. Are binary copper sulfides/selenides really new and promising thermoelectric materials? *Advanced Energy Materials*, pages n/a–n/a, 2014.

[49] Charles A Domenicali. Irreversible thermodynamics of thermoelectricity. *Reviews of Modern Physics*, 26(2):237, 1954.

[50] Fivos Drymiotis, Tristan W. Day, David R. Brown, Nicholas A. Heinz, and G. Jeffrey Snyder. Enhanced thermoelectric performance in the very low thermal conductivity ag2se0.5te0.5. *Applied Physics Letters*, 103(14):–, 2013.

[51] A. S. Dworkin and M. A. Bredig. Diffuse transition and melting in fluorite and anti-fluorite type of compounds - heat content of potassium sulfide from 298 to 1260 degrees k. *Journal of Physical Chemistry*, 72(4):1277, 1968.

[52] B. F. Dyson, T. Anthony, and D. Turnbull. Interstitial diffusion of copper and silver in lead. *Journal of Applied Physics*, 37(6):2370–2374, 1966.

[53] Paul Ehrenfest and Tatiana Ehrenfest. *The conceptual foundations of the statistical approach in mechanics.* Courier Dover Publications, 2002.

[54] F. El Akkad, B. Mansour, and T. Hendeya. Electrical and thermoelectric properties of Cu_2Se and Cu_2S. *Materials Research Bulletin*, 16(5):535–539, 1981.

[55] N.B. Elsner and J. Chin. Radioisotope space power generator. Annual report for the period July 1, 1973 – June 30, 1974. Report, 1975.

[56] N.B. Elsner, J. Chin, and G.H. Reynolds. *Fabrication of selenide segmented elements.* 1980.

[57] N.B. Elsner, J. Chin, G.H. Reynolds, J.H. Norman, J.C. Bass, and H.G. Staley. Isotec final report. Report GA-A-16584; Other: ON: DE82015077

United States10.2172/5437033Other: ON: DE82015077Thu Jul 05 07:24:33 EDT 2012NTIS, PC A07/MF A01.GA; INS-82-013511; NTS-82-011522; ERA-07-047144; EDB-82-114375English, 1981.

[58] N.B. Elsner, J. Chin, and H.G. Staley. Radioisotope space power generator annual report, july 1, 1974–june 30, 1975. [tpm-217 p-type material and sige technology]. Report, 1976.

[59] N.B. Elsner, J. Chin, H.G. Staley, J.C. Bass, E.J. Steeger, P.K. Gantzel, and J.M. Neill. Radioisotope space power generator annual report for the period october 1, 1976-september 30, 1978. Report, 1980.

[60] N.B. Elsner, J. Chin, H.G. Staley, E.J. Steeger, and P.K. Gantzel. Radioisotope space power generator. annual report, july 1, 1975–september 30, 1976. [tpm-217 p-type selenides]. Report, 1977.

[61] D. Emin. Enhanced seebeck coefficient from carrier-induced vibrational softening. *Physical Review B*, 59(9):6205–6210, 1999.

[62] David Emin. Phonon-mediated attraction between large bipolarons: Condensation to a liquid. *Physical Review B*, 49(13):9157–9167, 1994.

[63] John Fairbanks. Thermoelectric applications in vehicles status 2008. *US Department of Energy*, 2008.

[64] Marhoun Ferhat and Jiro Nagao. Thermoelectric and transport properties of -ag2se compounds. *Journal of Applied Physics*, 88(2):813–816, 2000.

[65] RA Ferrell, N Menyhard, H Schmidt, F Schwabl, and P Szepfalusy. Fluctuations and lambda phase transition in liquid helium. *Annals of Physics*, 47(3):565–613, 1968.

[66] F. Gascoin and A. Maignan. Order-disorder transition in $AgCrSe_2$: a new route to efficient thermoelectrics. *Chemistry of Materials*, 23(10):2510–2513, 2011.

[67] H Julian Goldsmid. *Introduction to thermoelectricity*, volume 121. Springer, 2009.

[68] Hiroshi Julian Goldsmid and L Jacob. *The thermal properties of solids*. Dover Publications, 1965.

[69] C. Goupil, W. Seifert, K. Zabrocki, E. Muller, and G. J. Snyder. Thermodynamics of thermoelectric phenomena and applications. *Entropy*, 13(8):1481–1517, 2011.

[70] N. Hainovsky and J. Maier. Simple phenomenological approach to premelting and sublattice melting in frenkel disordered ionic crystals. *Physical Review B*, 51(22):15789–15797, 1995.

[71] E. F. Hampl, J. D. Hinderman, W. C. Mitchell, R. S. Reylek, and D. A. Wald. Design of a thermoelectric converter using 3M high-performance thermoelectric material. *IEEE Transactions on Aerospace and Electronic Systems*, 11(5):952–952, 1975.

[72] E.F. Jr. Hampl. Thermoelectric materials evaluation program. quarterly technical task report no. 39. Report MMM–2473-342, 1972.

[73] E.F. Jr. Hampl. Thermoelectric materials evaluation program. Quarterly technical task report no. 43. Report MMM-2473-0398, 1974.

[74] E.F. Jr. Hampl. Thermoelectric materials evaluation program. Quarterly technical task report no. 44. [gdse/sub x/; tpm-217]. Report MMM-2331-0408, 1974.

[75] E.F. Jr. Hampl. Thermoelectric materials evaluation program. quarterly technical task report no. 46. [minnesota mining and manufacturing company, technical ceramic products div. , st. paul, 10/1 to 12/31/1975]. Report MMM-2473-0422, 1976.

[76] Terry Hendricks and William T Choate. Engineering scoping study of thermo-electric generator systems for industrial waste heat recovery. *US Department of Energy*, 20(0):6, 2006.

[77] J. P. Heremans, V. Jovovic, E. S. Toberer, A. Saramat, K. Kurosaki, A. Charoenphakdee, S. Yamanaka, and G. J. Snyder. Enhancement of ther-moelectric efficiency in PbTe by distortion of the electronic density of states. *Science*, 321(5888):554–557, 2008.

[78] RD Heyding. The copper/selenium system. *Canadian Journal of Chemistry*, 44(10):1233–1236, 1966.

[79] J.D. Hinderman. SIG galileo final converter. technical summary report. Report DOE/ET/33008-1, 1979.

[80] J.D. Hinderman. Thermoelectric materials evaluation program. annual techni-cal report for fiscal year 1979. Report MMM-2331-0642, 1979.

[81] J.D. Hinderman. Thermoelectric materials evaluation program. Technical sum-mary report. Report MMM-2331-0602 United States10.2172/5434752Thu Jun 28 08:45:09 EDT 2012NTIS, PC A13/MF A01.OSTI; ERA-05-026019; EDB-80-077515English, 1979.

[82] UT Hochli and JF Scott. Displacement parameter, soft-mode frequency, and fluctuations in quartz below its alpha-beta phase transition. *Physical Review Letters*, 26(26):1627, 1971.

[83] H. Holtan Jr, P. Mazur, and S. R. de Groot. On the theory of thermocouples and thermocells. *Physica*, 19(112):1109–1118, 1953.

[84] M. Horvatic and Z. Vucic. Dc ionic-conductivity measurements on the mixed conductor cu2-xse. *Solid State Ionics*, 13(2):117–125, 1984.

[85] Koross R Hosieni, Reed A Howald, and Matthew W Scanlon. Thermodynamics of the lambda transition and the equation of state of quartz. *American Mineralogist*, 70(7-8):782–793, 1985.

[86] S. Hull, P. Berastegui, S. G. Eriksson, and N. J. G. Gardner. Crystal structure and superionic conductivity of PbF_2 doped with KF. *Journal of Physics-Condensed Matter*, 10(38):8429–8446, 1998.

[87] Stephen Hull. Superionics: crystal structures and conduction processes. *Reports on Progress in Physics*, 67(7):1233–1314, 2004.

[88] S Ishiwata, Y Shiomi, JS Lee, MS Bahramy, T Suzuki, M Uchida, R Arita, Y Taguchi, and Y Tokura. Extremely high electron mobility in a phonon-glass semimetal. *Nature materials*, 12(6):512–517, 2013.

[89] Andrei A Istratov, Christoph Flink, Henry Hieslmair, Eicke R Weber, and Thomas Heiser. Intrinsic diffusion coefficient of interstitial copper in silicon. *Physical review letters*, 81(6):1243, 1998.

[90] S. Iwanaga, E. S. Toberer, A. LaLonde, and G. J. Snyder. A high temperature apparatus for measurement of the seebeck coefficient. *Review of Scientific Instruments*, 82(6):063905, 2011.

[91] M. Jaime, M. B. Salamon, K. Pettit, M. Rubinstein, R. E. Treece, J. S. Horwitz, and D. B. Chrisey. Magnetothermopower in $La_{0.67}Ca_{0.33}MnO_3$ thin films. *Applied Physics Letters*, 68(11):1576–1578, 1996.

[92] C. M. Jaworski, M. D. Nielsen, H. Wang, S. N. Girard, W. Cai, W. D. Porter, M. G. Kanatzidis, and J. P. Heremans. Valence-band structure of highly efficient p-type thermoelectric pbte-pbs alloys. *Physical Review B*, 87(4):045203, 2013.

[93] H.; Lindberg G.W. Johnston, W. V.; Weidersihch. Heat capacity, transformations, and thermal disorder in the solid electrolyte rbag4i5. *The Journal of Chemical Physics*, 51(9):3739, 1969.

[94] Martin Joshua. Protocols for the high temperature measurement of the seebeck coefficient in thermoelectric materials. *Measurement Science and Technology*, 24(8):085601, 2013.

[95] Mehran Kardar. *Statistical physics of fields*. Cambridge University Press, 2007.

[96] S. Kashida and J. Akai. X-ray-diffraction and electron-microscopy studies of the room-temperature structure of Cu_2Se. *Journal of Physics C-Solid State Physics*, 21(31):5329–5336, 1988.

[97] D. A. Keen, S. Hull, A. C. Barnes, P. Berastegui, W. A. Crichton, P. A. Madden, M. G. Tucker, and M. Wilson. Nature of the superionic transition in Ag^+ and Cu^+ halides. *Physical Review B*, 68(1):014117, 2003.

[98] V Keppens, D Mandrus, BC Sales, BC Chakoumakos, P Dai, R Coldea, MB Maple, DA Gajewski, EJ Freeman, and S Bennington. Localized vibrational modes in metallic solids. *Nature*, 395(6705):876–878, 1998.

[99] H. S. Kim and H. I. Yoo. Compilation of all the isothermal mass/charge transport properties of the mixed conducting $La_2NiO_{4+\delta}$ at elevated temperatures. *Physical Chemistry Chemical Physics*, 13(10):4651–4658, 2011.

[100] Charles Kittel and Paul McEuen. *Introduction to solid state physics*, volume 8. Wiley New York, 1976.

[101] M. A. Korzhuev. The entropy of fusion and the growth-morphology of superionic $Cu_{2-X}Se$ crystals. *Physica Status Solidi a-Applied Research*, 127(1):K1–K3, 1991.

[102] M. A. Korzhuev. Dufour effect in superionic copper selenide. *Physics of the Solid State*, 40(2):217–219, 1998.

[103] M. A. Korzhuev. Entropy of crystallization of materials from a "molten" sublattice of superionic conductors. *Physics of the Solid State*, 40(2):204–205, 1998.

[104] M. A. Korzhuev. Conflict between internal combustion engine and thermoelectric generator during waste heat recovery in cars. *Technical Physics Letters*, 37(2):151–153, 2011.

[105] M. A. Korzhuev, N. K. Abrikosov, and I. V. Kuznetsova. Isolation of moving copper from the $Cu_{2-X}Se$ under the pressure effect. *Pisma V Zhurnal Tekhnicheskoi Fiziki*, 13(1):9–14, 1987.

[106] M. A. Korzhuev, V. F. Bankina, I. G. Korolkova, G. B. Sheina, and E. A. Obraztsova. Doping effects on mechanical-properties and microhardness of superionic copper selenide $Cu_{2-X}Se$. *Physica Status Solidi a-Applied Research*, 123(1):131–137, 1991.

[107] M. A. Korzhuev and A. V. Laptev. Thermodiffusion and piezodiffusion effects in superionic copper selenide. *Fizika Tverdogo Tela*, 29(9):2646–2650, 1987.

[108] M. A. Korzhuev, A. V. Laptev, and N. K. Abrikosov. Superfast homogenization and kirkendale effect in superionic copper selenide. *Fizika Tverdogo Tela*, 29(5):1543–1546, 1987.

[109] W. Koshibae and S. Maekawa. Effects of spin and orbital degeneracy on the thermopower of strongly correlated systems. *Physical Review Letters*, 87(23), 2001.

[110] W. Koshibae, K. Tsutsui, and S. Maekawa. Thermopower in cobalt oxides. *Physical Review B*, 62(11):6869–6872, 2000.

[111] Y. Kowada, Y. Yamada, M. Tatsumisago, T. Minami, and H. Adachi. Variation of electronic state of AgI-based superionic conductors with movement of Ag ions. *Solid State Ionics*, 136:393–397, 2000.

[112] R. Kubo. Statistical-mechanical theory of irreversible processes .1. General theory and simple applications to magnetic and conduction problems. *Journal of the Physical Society of Japan*, 12(6):570–586, 1957.

[113] R. Kubo, M. Yokota, and S. Nakajima. Statistical-mechanical theory of irreversible processes .2. response to thermal disturbance. *Journal of the Physical Society of Japan*, 12(11):1203–1211, 1957.

[114] M. Kusakabe, Y. Ito, and S. Tamaki. The specific heat of the solid electrolyte system cui-agi. *Journal of Physics-Condensed Matter*, 8(37):6851–6856, 1996.

[115] M. Laguesse, A. Rulmont, Ch Laurent, S. K. Patapis, H. W. Vanderschueren, P. Tarte, and M. Ausloos. Thermoelectric power and magneto seebeck-effect near the critical temperature of granular ceramic oxide superconductors y1ba2ca3o7y. *Solid state communications*, 66(4):445–450, 1988.

[116] A. D. LaLonde, T. Ikeda, and G. J. Snyder. Rapid consolidation of powdered materials by induction hot pressing. *Review of Scientific Instruments*, 82(2):025104, 2011.

[117] Saniya LeBlanc, Shannon K. Yee, Matthew L. Scullin, Chris Dames, and Kenneth E. Goodson. Material and manufacturing cost considerations for thermoelectrics. *Renewable and Sustainable Energy Reviews*, 32(0):313–327, 2014.

[118] F. L. Lederman, M. B. Salamon, and H. Peisl. Evidence for an order-disorder transformation in solid electrolyte rb ag-4i-5. *Solid State Communications*, 19(2):147–150, 1976.

[119] J. H. Lee and H. I. Yoo. Electrochemical study of the cross effect between ion and electron flows in semiconducting coo. *Journal of the Electrochemical Society*, 141(10):2789–2794, 1994.

[120] C. J. Liu, C. S. Sheu, T. W. Wu, L. C. Huang, F. H. Hsu, H. D. Yang, G. V. M. Williams, and C. J. C. Liu. Magnetothermopower and magnetoresistivity of $RuSr_2Gd_{1-x}La_xCu_2O_8$ (x=0,0.1). *Physical Review B*, 71(1), 2005.

[121] Huili Liu, Xun Shi, Melanie Kirkham, Hsin Wang, Qiang Li, Ctirad Uher, Wenqing Zhang, and Lidong Chen. Structure-transformation-induced abnormal

thermoelectric properties in semiconductor copper selenide. *Materials Letters*, 93:121–124, 2013.

[122] Huili Liu, Xun Shi, Fangfang Xu, Linlin Zhang, Wenqing Zhang, Lidong Chen, Qiang Li, Ctirad Uher, Tristan Day, and G. Jeffrey Snyder. Copper ion liquid-like thermoelectrics. *Nature Materials*, 11(5):422–425, 2012.

[123] Huili Liu, Xun Yuan, Ping Lu, Xun Shi, Fangfang Xu, Ying He, Yunshan Tang, Shengqiang Bai, Wenqing Zhang, Lidong Chen, Yue Lin, Lei Shi, He Lin, Xingyu Gao, Xingmin Zhang, Hang Chi, and Ctirad Uher. Ultrahigh thermoelectric performance by electron and phonon critical scattering in $Cu_2Se_{1-x}Ix$. *Advanced Materials*, 25(45):6607–6612, 2013.

[124] N. D. Lowhorn, W. Wong-Ng, W. Zhang, Z. Q. Lu, M. Otani, E. Thomas, M. Green, T. N. Tran, N. Dilley, S. Ghamaty, N. Elsner, T. Hogan, A. D. Downey, Q. Jie, Q. Li, H. Obara, J. Sharp, C. Caylor, R. Venkatasubramanian, R. Willigan, J. Yang, J. Martin, G. Nolas, B. Edwards, and T. Tritt. Round-robin measurements of two candidate materials for a Seebeck coefficient standard reference material (tm). *Applied Physics a-Materials Scienceand Processing*, 94(2):231–234, 2009.

[125] Nathan Lowhorn, Winnie Wong Ng, Zhan-Qian Lu, Joshua Martin, Martin Green, John Bonevich, Evan Thomas, Neil Dilley, and Jeff Sharp. Development of a seebeck coefficient standard reference material. *Journal of materials research*, 26(15):1983–1992, 2011.

[126] ZQ Lu, Nathan D Lowhorn, Winnie Wong-Ng, Weiping Zhang, Makoto Otani, Evan E Thomas, Martin L Green, and Thanh N Tran. Statistical analysis of a round-robin measurement survey of two candidate materials for a seebeck coefficient standard reference material. Report, DTIC Document, 2009.

[127] Georg KH Madsen and David J Singh. BoltzTraP. A code for calculating band-

structure dependent quantities. *Computer Physics Communications*, 175(1):67–71, 2006.

[128] G. D. Mahan and J. O. Sofo. The best thermoelectric. *Proceedings of the National Academy of Sciences of the United States of America*, 93(15):7436–7439, 1996.

[129] J Martin, T Tritt, and Ctirad Uher. High temperature seebeck coefficient metrology. *Journal of Applied Physics*, 108(12):121101, 2010.

[130] Joshua Martin. Apparatus for the high temperature measurement of the seebeck coefficient in thermoelectric materials. *Review of Scientific Instruments*, 83(6):065101, 2012.

[131] Joshua Martin, Winnie Wong-Ng, Thierry Caillat, I. Yonenaga, and Martin L. Green. Thermocyclic stability of candidate seebeck coefficient standard reference materials at high temperature. *Journal of Applied Physics*, 115(19):–, 2014.

[132] S.R. DeGroot Mazur and P. *Non-Equillibrium Thermodynamics*. Dover Publications, New York, 1962.

[133] Wenlong Mi, Pengfei Qiu, Tiansong Zhang, Yanhong Lv, Xun Shi, and Lidong Chen. Thermoelectric transport of Se-rich Ag_2Se in normal phases and phase transitions. *Applied Physics Letters*, 104(13):–, 2014.

[134] O. Milat, Z. Vucic, and B. Ruscic. Superstructural ordering in low-temperature phase of superionic Cu_2Se. *Solid State Ionics*, 23(1-2):37–47, 1987.

[135] RC Miller, RR Heikes, and RW Ure Jr. Thermoelectricity: Science and engineering. *Interscience, New York*, page 438, 1961.

[136] S. Miyatani. Ionic conduction in $\beta - ag_2te$ and $\beta - ag_2se$. *Journal of the Physical Society of Japan*, 14(8):996–1002, 1959.

[137] S. Miyatani. Experimental evidence for the Onsager reciprocal relation in mixed conduction. *Solid State Communications*, 38(4):257–259, 1981.

[138] S. Mukerjee. Thermopower of the hubbard model: Effects of multiple orbitals and magnetic fields in the atomic limit. *Physical Review B*, 72(19), 2005.

[139] S. Mukerjee and J. E. Moore. Doping dependence of thermopower and thermoelectricity in strongly correlated materials. *Applied Physics Letters*, 90(11), 2007.

[140] P Navard and JM Haudin. The height of DSC phase transition peaks. *Journal of Thermal Analysis and Calorimetry*, 29(3):405–414, 1984.

[141] H. Ogawa and M. Kobayashi. Cross conduction in superionic conductors. *Solid State Ionics*, 96(12):95–98, 1997.

[142] H. Ogawa and M. Kobayashi. Cross conductivity in silver chalcogenides. *Solid State Ionics*, 148(12):211–217, 2002.

[143] Ogorelec.Z and B. Celustka. Thermoelectric power and phase transitions of non-stoichiometric cuprous selenide. *Journal of Physics and Chemistry of Solids*, 27(3):615, 1966.

[144] K. Okamoto. Thermoelectric power and phase transition of Cu_2Se. *Japanese Journal of Applied Physics*, 10(4):508, 1971.

[145] M. Oliveria, R. K. McMullan, and B. J. Wuensch. Single crystal neutron diffraction analysis of the cation distribution in the high-temperature phases $Cu_{2-x}S$, $Cu_{2-x}Se$, and Ag_2Se. *Solid State Ionics*, 2830, Part 2(0):1332–1337, 1988.

[146] M. L. Olsen, E. L. Warren, P. A. Parilla, E. S. Toberer, C. E. Kennedy, G. J. Snyder, S. A. Firdosy, B. Nesmith, A. Zakutayev, A. Goodrich, C. S. Turchi, J. Netter, M. H. Gray, P. F. Ndione, R. Tirawat, L. L. Baranowski, A. Gray, and D. S. Ginley. A high-temperature, high-efficiency solar thermoelectric generator prototype. *Energy Procedia*, 49(0):1460–1469, 2014.

[147] Lars Onsager. Reciprocal relations in irreversible processes. I. *Physical Review*, 37(4):405–426, 1931.

[148] Jon L Opsal, Barry J Thaler, and Jack Bass. Electron-phonon mass enhancement in thermoelectricity. *Physical Review Letters*, 36(20):1211, 1976.

[149] W. E. Osmeyer. Selenide isotope generator for the galileo mission. program final report. Report TES-33009-46, 1979.

[150] J. F. Osterle. Unified treatment of thermodynamics of steady-state energy conversion. *Applied Scientific Research Section a-Mechanics Heat Chemical Engineering Mathematical Methods*, 12(6):425, 1964.

[151] W. J. Pardee and G. D. Mahan. Disorder and ionic polarons in solid electrolytes. *Journal of Solid State Chemistry*, 15(4):310–324, 1975.

[152] Camille Parmesan and Gary Yohe. A globally coherent fingerprint of climate change impacts across natural systems. *Nature*, 421(6918):37–42, 2003.

[153] Y. Z. Pei, X. Y. Shi, A. LaLonde, H. Wang, L. D. Chen, and G. J. Snyder. Convergence of electronic bands for high performance bulk thermoelectrics. *Nature*, 473(7345):66–69, 2011.

[154] Yanzhong Pei, Heng Wang, and G. J. Snyder. Band engineering of thermoelectric materials. *Advanced Materials*, 24(46):6125–6135, 2012.

[155] JCA Peltier. Nouvelles experiences sur la caloricite des courants electrique. *Annales de Chimie et de Physique*, 56:371–386, 1834.

[156] JC Phillips. Ionicity of the chemical bond in crystals. *Reviews of Modern Physics*, 42(3):317, 1970.

[157] AB Pippard. Xlviii. thermodynamic relations applicable near a lambda-transition. *Philosophical Magazine*, 1(5):473–476, 1956.

[158] Max Planck. Entropie und temperatur strahlender waerme. *Annalen der Physik*, 306(4):719–737, 1900.

[159] PJ Price. Cxxxv. Ambipolar thermodiffusion of electrons and holes in semiconductors. *Philosophical Magazine*, 46(382):1252–1260, 1955.

[160] E. H. Putley. The hall coefficient, electrical conductivity and magneto-resistance effect of lead sulphide, selenide and telluride. *Proceedings of the Physical Society of London Section B*, 68(1):22–34, 1955.

[161] P. Rahlfs. The cubic high temperature modificators of sulfides, selenides and tellurides of silver and of uni-valent copper. *Zeitschrift fr physikalische Chemie. Abteilung B, Chemie der Elementarprozesse, Aufbau der Materie*, 31(3):157–194, 1936.

[162] C. N. R. Rao and K. J. Rao. *Phase transitions in solids : an approach to the study of the chemistry and physics of solids*. McGraw-Hill, New York, 1978.

[163] M. J. Rice and W. L. Roth. Ionic transport in super ionic conductors - theoretical model. *Journal of Solid State Chemistry*, 4(2):294–, 1972.

[164] I. Riess. Measurements of electronic and ionic partial conductivities in mixed conductors, without the use of blocking electrodes. *Solid State Ionics*, 44(3-4):207–214, 1991.

[165] I. Riess. Review of the limitation of the Hebb-Wagner polarization method for measuring partial conductivities in mixed ionic electronic conductors. *Solid State Ionics*, 91(3-4):221–232, 1996.

[166] I. Riess. What does a voltmeter measure? *Solid State Ionics*, 95(3-4):327–328, 1997.

[167] I. Riess. Mixed ionic-electronic conductors - material properties and applications. *Solid State Ionics*, 157(1-4):1–17, 2003.

[168] Fred Ritz and Craig E Peterson. Multi-mission radioisotope thermoelectric generator (MMRTG) program overview. In *Aerospace Conference, 2004. Proceedings. 2004 IEEE*, volume 5. IEEE.

[169] A.L. Rockwood. Relationship of thermoelectricity to electronic entropy. *Physical Review A*, 30(5):2843–2844, 1984.

[170] D.M. Rowe. *Materials, Preparation, and Characterization in Thermoelectrics*. Taylorand Francis, 2012.

[171] K. D. Sandbakk, A. Bentien, and S. Kjelstrup. Thermoelectric effects in ion conducting membranes and perspectives for thermoelectric energy conversion. *Journal of Membrane Science*, 434(0):10–17, 2013.

[172] V. Sandomirsky, A. V. Butenko, R. Levin, and Y. Schlesinger. Electric-field-effect thermoelectrics. *Journal of Applied Physics*, 90(5):2370–2379, 2001.

[173] W Schweika, RP Hermann, M Prager, J Persson, and Veerle Keppens. Dumbbell rattling in thermoelectric zinc antimony. *Physical review letters*, 99(12):125501, 2007.

[174] T. J. Seebeck. Ueber die magnetische polarisation der metalle und erze durch temperaturdifferenz. *Annalen der Physik*, 82(3):253–286, 1826.

[175] Thomas Johann Seebeck. *Ueber den Magnetismus der galvanischen Kette*. Berlin, 1821.

[176] Thomas Johann Oettingen A. Seebeck. *Magnetische polarisation der metalle und erze durch temperatur-differenz*. W. Engelmann, Leipzig, 1823.

[177] N. N. Sirota, M. A. Korzhuev, M. A. Lobzov, N. K. Abrikosov, and V. F. Bankina. Superplasticity of beta-phase of copper selenide possessing the superionic conduction. *Doklady Akademii Nauk Sssr*, 281(1):75–77, 1985.

[178] W. Sitte. Electrochemical cell for composition dependent measurements of chemical diffusion coefficients and ionic conductivities on mixed conductors and application to silver telluride at 160c. *Solid State Ionics*, 59(12):117–124, 1993.

[179] G. J. Snyder, Mogens Christensen, Eiji Nishibori, Thierry Caillat, and Bo Iversen. Disordered zinc in Zn_4Sb_3 with phonon-glass and electron-crystal thermoelectric properties. *Nature Materials*, 3(7):458–63, 2004.

[180] G. J. Snyder and E. S. Toberer. Complex thermoelectric materials. *Nature Materials*, 7(2):105–114, 2008.

[181] G. Stapfer. Copper-selenide system, p-type tpm-217. Report DOE/ET/33003-T5, 1977.

[182] G. Stapfer. Development of the data base of a degradation model of a selenide RTG. *Proceedings of the the 12th IECEC*, 1977.

[183] G. Stapfer and L. Garvey. Progress report no. 29 for a program of thermoelectric generator testing and rtg degradation mechanisms evaluation. Report DOE/ET/33003-T2, 1979.

[184] AB Thompson and EH Perkins. *Lambda transitions in minerals*, pages 35–62. Springer, 1981.

[185] E. S. Toberer, P. Rauwel, S. Gariel, J. Tafto, and G. J. Snyder. Composition and the thermoelectric performance of $beta - Zn_4Sb_3$. *Journal of Materials Chemistry*, 20(44):9877–9885, 2010.

[186] E. S. Toberer, K. A. Sasaki, C. R. I. Chisholm, S. M. Haile, W. A. Goddard, and G. J. Snyder. Local structure of interstitial zn in $\beta - zn_4sb_3$. *Physica Status Solidi-Rapid Research Letters*, 1(6):253–255, 2007.

[187] Richard C. Tolman and Paul C. Fine. On the irreversible production of entropy. *Reviews of Modern Physics*, 20(1):51–77, 1948.

[188] A. Tonejc and A. M. Tonejc. X-ray-diffraction study on alpha-reversible-beta-phase transition of Cu_2Se. *Journal of Solid State Chemistry*, 39(2):259–261, 1981.

[189] K. Trachenko. Heat capacity of liquids: An approach from the solid phase. *Physical Review B*, 78(10), 2008.

[190] B. Vengalis, K. Valacka, N. Shiktorov, and V. Yasutis. The state of $Cu_{2-\delta}Se$ below the superionic phase-transition temperature. *Fizika Tverdogo Tela*, 28(9):2675–2679, 1986.

[191] Z. Vucic, V. Horvatic, and O. Milat. Dilatometric study of nonstoichiometric copper selenide $Cu_{2-x}Se$. *Solid State Ionics*, 13(2):127–133, 1984.

[192] Z. Vucic, V. Horvatic, and Z. Ogorelec. Influence of the cation disordering on the electronic conductivity of superionic copper selenide. *Journal of Physics C-Solid State Physics*, 15(16):3539–3546, 1982.

[193] Z. Vucic and Z. Ogorelec. Unusual behavior of nonstoichiometric cuprous selenide at the transition to the superionic phase. *Philosophical Magazine B-Physics of Condensed Matter Statistical Mechanics Electronic Optical and Magnetic Properties*, 42(2):287–296, 1980.

[194] Z. Vui, O. Milat, V. Horvati, and Z. Ogorelec. Composition-induced phase-transition splitting in cuprous selenide. *Physical Review B*, 24(9):5398–5401, 1981.

[195] Hsin Wang, Wallace D Porter, Harald Bttner, Jan Knig, Lidong Chen, Shengqiang Bai, Terry M Tritt, Alex Mayolet, Jayantha Senawiratne, and Charlene Smith. Transport properties of bulk thermoelectrics: An international round-robin study, part i: Seebeck coefficient and electrical resistivity. *Journal of electronic materials*, 42(4):654–664, 2013.

[196] Y. Y. Wang, N. S. Rogado, R. J. Cava, and N. P. Ong. Spin entropy as the likely source of enhanced thermopower in $Na_xCo_2O_4$. *Nature*, 423(6938):425–428, 2003.

[197] W. Weppner, C. Lichuan, and W. Piekarczyk. Electrochemical determination of phase-diagrams and thermodynamic data of multicomponent systems. *Zeitschrift Fur Naturforschung Section a-a Journal of Physical Sciences*, 35(4):381–388, 1980.

[198] G. A. Wiegers. Crystal-structure of low-temperature form of silver selenide. *American Mineralogist*, 56(11-1):1882, 1971.

[199] Chong Xiao, Jie Xu, Kun Li, Jun Feng, Jinlong Yang, and Yi Xie. Superionic phase transition in silver chalcogenide nanocrystals realizing optimized thermoelectric performance. *Journal of the American Chemical Society*, 134(9):4287–4293, 2012.

[200] Xing-Xing Xiao, Wen-Jie Xie, Xin-Feng Tang, and Qing-Jie Zhang. Phase transition and high temperature thermoelectric properties of copper selenide $Cu_{2-x}Se$ ($0 < x < 0.25$). *Chinese Physics B*, 20(8):087201, 2011.

[201] K. Yamamoto and S. Kashida. X-ray study of the cation distribution in Cu_2Se, $Cu_{1.8}Se$ and $Cu_{1.8}S$ - analysis by the maximum-entropy method. *Solid State Ionics*, 48(3-4):241–248, 1991.

[202] Jihui Yang and Thierry Caillat. Thermoelectric materials for space and automotive power generation. *MRS bulletin*, 31(03):224–229, 2006.

[203] Shannon K. Yee, Saniya LeBlanc, Kenneth E. Goodson, and Chris Dames. Dollar per w metrics for thermoelectric power generation: beyond zt. *Energy and Environmental Science*, 6(9):2561–2571, 2013.

[204] H. Yin, M. Christensen, N. Lock, and B. B. Iversen. Zn migration during spark plasma sintering of thermoelectric Zn_4Sb_3. *Applied Physics Letters*, 101(4), 2012.

[205] Han-Ill Yoo, Jong-Ho Lee, M. Martin, J. Janek, and H. Schmalzried. Experimental evidence of the interference between ionic and electronic flows in an oxide with prevailing electronic conduction. *Solid State Ionics*, 67(34):317–322, 1994.

[206] B. Yu. Thermoelectric properties of copper selenide with ordered selenium layer and disordered copper layer. *Nano Energy*, 1(3):472–478, 2012.

[207] Jaemin Yu and Hoseop Yun. Reinvestigation of the low-temperature form of Ag_2Se (naumannite) based on single-crystal data. *Acta crystallographica. Section E*, 67(Pt 9):i45–U123, 2011.